DEVELOPMENT AND CHARACTERIZATION OF BIO-BASED BASALT FIBER REINFORCED POLYMER COMPOSITES FOR AUTOMOTIVE STRUCTURAL APPLICATIONS

A Ph.D. DISSERTATION PRESENTED TO THE DEPARTMENT OF MATERIALS SCIENCE AND ENGINEERING

AFRICAN UNIVERSITY OF SCIENCE AND TECHNOLOGY

By

MUSA ABDULRAHMAN ADEIZA

(70219)

April, 2026

DEVELOPMENT AND CHARACTERIZATION OF BIO-BASED BASALT FIBER REINFORCED POLYMER COMPOSITES FOR AUTOMOTIVE STRUCTURAL APPLICATIONS

A Dissertation submitted to the Department of Materials Science and Engineering
African University of Science and Technology, Abuja, Nigeria
In partial fulfilment of the requirements for the degree of Doctor of Philosophy in Materials Science and Engineering

By

MUSA ABDULRAHMAN ADEIZA
(70219)

PhD Supervisors:

Prof. Azikiwe Peter Onwualu (African University of Science and Technology, AUST, Nigeria)

Dr. Minkook Kim (Korea Institute of Science and Technology, KIST, Republic of Korea)

Ph.D. Committee Members:

Dr. Vitalis C. Anye (African University of Science and Technology, AUST, Nigeria)

Dr. Abdulhakeem Bello (African University of Science and Technology, AUST, Nigeria)

Prof. Kamilu Adeyemi Bello (Ahmadu Bello University, ABU, Zaria, Nigeria)

Dr. Ifeyinwa Ijeoma Obianyo (Nile University, Abuja, Nigeria)

CERTIFICATION

This is to certify that the thesis titled "**DEVELOPMENT AND CHARACTERIZATION OF BIO-BASED BASALT FIBER REINFORCED POLYMER COMPOSITES FOR AUTOMOTIVE STRUCTURAL APPLICATIONS**" submitted to the School of Postgraduate Studies, African University of Science and Technology (AUST), Abuja, Nigeria, for the award of the Doctor of Philosophy (Ph.D.) degree, is a record of original research carried out by Musa, Abdulrahman Adeiza in the Department of Materials Science and Engineering.

DEVELOPMENT AND CHARACTERIZATION OF BIO-BASED BASALT FIBER REINFORCED POLYMER COMPOSITES FOR AUTOMOTIVE STRUCTURAL APPLICATIONS

By

MUSA ABDULRAHMAN ADEIZA

A DISSERTATION APPROVED BY THE MATERIALS SCIENCE AND ENGINEERING DEPARTMENT

10/04/2026

RECOMMENDED: …….
Supervisor: Professor Azikiwe Peter Onwualu

11/04/2026

…….
Co-supervisor: Dr. Minkook Kim

APPROVED: …….
Head of Department: Dr. Vitalis C. Anye

…….
Chief Academic Officer

Date: …….

ABSTRACT

The growing demand for sustainable lightweight materials in the automotive industry has increased interest in basalt fiber-reinforced polymer (BFRP) composites as eco-friendly alternatives to conventional composites. Basalt fibers (BFs) offer excellent mechanical properties, thermal stability, and environmental benefits. However, their application is often limited by weak interfacial bonding with polymer matrices due to their smooth and chemically inert surfaces. This study presents a novel nanocellulose (NC) grafting approach as the primary contribution, where cellulose nanofiber (CNF) and cellulose nanocrystal (CNC) were directly anchored onto silane-functionalized BFs before composite fabrication. Unlike conventional direct NC dispersion in epoxy, which often suffers from agglomeration and poor dispersion, the proposed grafting strategy localizes NC at the fiber–matrix interface, significantly improving load transfer and interfacial adhesion. The NC-grafted BFRP composites exhibited significant improvements in interfacial bonding, resulting in enhanced impact resistance, interlaminar shear strength, and overall mechanical performance compared with composites produced through direct NC–epoxy mixing. In addition, the grafted composites demonstrated improved resistance to moisture absorption, despite the naturally hydrophilic nature of NCs, indicating that surface immobilization of NC effectively mitigates water uptake at the interface. Surface analyses using X-ray Photoelectron Spectroscopy (XPS) and Field Emission Scanning Electron Microscopy (FE-SEM) confirmed successful grafting and improved interfacial morphology. To assess structural applicability, composite components were further evaluated through impact crushing experiments and finite element simulations using Abaqus CAE. The strong agreement between experimental and simulation results confirmed the reliability, energy absorption capability, and crashworthiness of the developed composites for lightweight automotive structures. Overall, this work demonstrates that NC grafting onto BFs is a highly effective strategy for overcoming interfacial bonding and dispersion challenges, offering a promising route toward durable and sustainable automotive composite materials.

KEYWORD

BFRP, Nanocellulose, Interfacial bonding, Crashworthiness, Mechanical properties, Finite element modelling

ACKNOWLEDGEMENT

First and foremost, I express my deepest gratitude to Almighty Allah for His guidance, strength, and blessings throughout this PhD journey. My sincere appreciation goes to the PASET-RSIF for their scholarship and financial support, which made this research possible. Their dedication to advancing scientific research has been instrumental in my academic growth. I am profoundly grateful to my exceptional supervisors, Prof. Azikiwe Peter Onwualu (President, African University of Science and Technology, Abuja, Nigeria) and Dr. Minkook Kim (Senior Researcher, Korea Institute of Science and Technology, KIST, Republic of Korea), for their invaluable guidance, encouragement, and support. Their expertise, mentorship, and insightful advice have played a crucial role in shaping my research. I also appreciate my PhD committee members for their constructive feedback, which has enriched this study. Special thanks to Dr. Soon Ho Yoon (Senior Researcher, KIST) for his invaluable guidance and advice. Additionally, I extend my sincere gratitude to my lab members, especially Dr. Thuan, Dr. Jeon, Dr. Anand, and Mr. Junha Park, for their wonderful support throughout this journey. To my beloved wife, Hajiya Lauratu Hassan, and my wonderful daughters, Ruwaidah and Rufaidah Abdulrahman, your love, patience, and unwavering support have been my greatest source of strength. Your sacrifices, understanding, and constant prayers have made this journey possible, and I am forever grateful for your presence in my life. I extend my heartfelt gratitude to my family, particularly my dearest mother, Hajiya Habibat Mayaki, my siblings, and all my friends, whose constant encouragement has motivated me to succeed in this journey. Your countless support and prayers have been the determining factors in achieving this milestone. Finally, I thank all those who contributed directly or indirectly to this research. Your kindness and assistance were deeply appreciated.

PREFACE

This dissertation is the original work of Musa Abdulrahman Adeiza and was conducted at the African University of Science and Technology (AUST), Abuja, Nigeria, and Korea Institute of Science and Technology (KIST), Republic of Korea, in fulfillment of the requirements for the award of the Doctor of Philosophy degree in Materials Science and Engineering. The research was carried out within the framework of advanced composite materials development, with a focus on environmentally sustainable solutions for automotive applications. I served as the principal investigator for this research and was responsible for all major aspects of the work, including conceptualization, experimental design, materials fabrication, mechanical and surface characterization, data analysis, numerical simulation, and the preparation of the thesis manuscript, under the supervision and support of Prof. A. P. Onwualu (AUST, Abuja) and Dr. Kim Minkook (KIST, Republic of Korea), as well as the guidance of other committee members.

This study investigates the development of basalt fiber–reinforced polymer (BFRP) composites enhanced through nanocellulose (NC) grafting to improve fiber–matrix interfacial bonding and overall mechanical performance. The work involved the surface functionalization of basalt fibers using both cellulose nanofiber and cellulose nanocrystal additives. Experimental and numerical results were critically analyzed to validate the applicability of the developed composites for lightweight automotive structures.

At the time of submission of this thesis, Chapters 4 and 5 have been published in Composites Part A: Applied Science and Manufacturing, and Chapter 6 has been published in Polymer Composites (Wiley Online Library).

TABLE OF CONTENTS

COVER PAGE ..... **i**
TITLE PAGE ..... **ii**
CERTIFICATION ..... **iii**
SIGNATURE PAGE ..... **iv**
COPYRIGHT PAGE ..... **v**
ABSTRACT ..... **vi**
KEYWORD ..... **vi**
ACKNOWLEDGEMENT ..... **vii**
PREFACE ..... **viii**
TABLE OF CONTENTS ..... **ix**
LIST OF ABBREVIATIONS ..... **xiv**
LIST OF SYMBOLS ..... **xvi**
DEFINITIONS OF IMPORTANT TERMS ..... **xviii**
LIST OF FIGURES ..... **xx**
LIST OF TABLES ..... **xxiii**
LIST OF PUBLICATIONS ..... **xxiv**
CHAPTER ONE **1**
1. INTRODUCTION **1**
1.1. Background 1
1.2. Problem Statement 5
1.3. Research Questions 6
1.4. Research Aim and Objectives 7
1.5. Scope of the Study 7
1.6. Significance/Justification of the Study 8
1.7. Dissertation Layout 9
CHAPTER TWO **11**
2. LITERATURE REVIEW **11**
2.1. Overview of Literature Review 11
2.2. Composite Materials 13
2.3. Brief History of Basalt 16
2.4. Basalt Fiber Production and Chemical Characteristics 18

2.5. Application of Basalt Fiber 21
2.6. Basalt Fiber Reinforced Polymer (BFRP) 23
2.6.1. Biodegradable Polymer 24
2.6.2. Synthetic-Based Polymer 25
2.6.3. Epoxy Resin 25
2.7. Potential of BFRPs in Automotive Structures 26
2.7.1. Lightweight and Sustainability Trends in Automotive 27
2.7.2. Use of BFRP in Load-Bearing Components 27
2.8. Enhancement of Basalt Fiber Reinforced Polymer Composite 28
2.8.1. Chemical Treatment 30
2.8.2. Hybridization with Other Fibers 30
2.8.3. Modification with Nanoparticle 33
2.8.3.1. Direct Dispersion in Matrix Resin 33
2.8.3.2. Attaching the Nanoparticle to the BF Surface 34
2.9. Nanocellulose 35
2.9.1. Types of Nanocellulose 35
2.9.1.1. Cellulose Nanofiber (CNF) 36
2.9.1.2. Cellulose Nanocrystals (CNC) 37
2.9.2. Advantages of Nanocellulose 38
2.9.3. NC-modified FRP and its Challenges 39
2.10. Development of Hat-Shaped BFRP Composite 40
2.10.1. Fabrication and Experimental Procedure 40
2.10.2. Modeling and Simulation 41
2.10.3. Damage Criteria 44
2.10.3.1. Maximum Stress/Strain Criterion 45
2.10.3.2. Tsai–Hill Criterion 45
2.10.3.3. Tsai–Wu Criterion 45
2.10.3.4. Hashin's Criterion 46
2.11. Delamination Behavior With CZM 47
2.12. Critical Research Gaps and Scientific Positioning of the Developed BFRP 51
CHAPTER THREE 56
3. RESEARCH METHODOLOGY 56
3.1. Introduction 56

3.2. Materials Used 56
3.2.1. Reinforcement material 56
3.2.2. Matrix material 57
3.2.3. Auxiliary materials 57
3.3. Equipment and Methods Used 58
3.3.1. Mixing and homogenization 58
3.3.2. Curing equipment 58
3.3.3. Material characterization 59
3.4. Numerical Simulation Approach 59
3.5. Overview of the Research Organization 60
CHAPTER FOUR 61
4. EFFECT OF NC DISPERSION ON BF/EPOXY COMPOSITES 61
4.1. Introduction 61
4.2. Materials and Methods 64
4.2.1. Materials 64
4.2.2. Preparation and Mixing of NCs into Epoxy Resin 65
4.2.3. NC-Dispersed BFRP Fabrication 66
4.2.4. Mechanical Property 67
4.2.5. Scanning Electron Microscopy 68
4.3. Results and Discussion 68
4.3.1. Tensile Property 68
4.3.2. Interlaminar Shear Strength 71
4.3.3. Izod Impact Strength 74
4.4. Concluding Remark 75
CHAPTER FIVE 77
5. IMPROVING BF/EPOXY BONDING USING NC GRAFTING APPROACH 77
5.1. Introduction 77
5.2. Materials and Methods 78
5.2.1. Materials 78
5.2.2. Grafting Techniques and Reaction Mechanisms of NC on the BF Surface 78
5.2.3. NC-Grafted BFRP Fabrication 81
5.2.4. Mechanical Property 82
5.2.5. X-ray Photoelectron Spectroscopy (XPS) 82

5.2.6. Moisture Absorption Test 82
5.2.7. Fracture Toughness Test 83
5.3. Results and Discussion 86
5.3.1. Surface Functional Groups of BF, NCs, and NC-Grafted BFs 86
5.3.2. Tensile Strength and Stiffness 92
5.3.3. Interlaminar Shear Strength 94
5.3.4. Izod Impact Strength 99
5.3.5. Moisture Absorption of NC-grafted BFRP 102
5.3.6. Fracture Toughness of Optimized NC-Grafted BFRP Composite 105
5.4. Concluding Remark 109
CHAPTER SIX 110
6. FINITE ELEMENT MODELING AND EXPERIMENTAL INVESTIGATION OF THE IMPACT BEHAVIOR OF HAT-SHAPED BFRP COMPOSITES 110
6.1. Introduction 110
6.2. Materials and Methods 113
6.2.1. Materials 113
6.3. Finite Element Modeling 114
6.3.1. Geometry Definition 115
6.3.2. Material Property Assignment 115
6.3.3. Meshing 118
6.3.4. Contact Interaction 120
6.3.5. Boundary Conditions 120
6.4. Experimental Investigation 121
6.4.1. Fabrication of Hat-Shaped BFRP 121
6.4.2. Dynamic Impact Test 123
6.5. Results and Discussion 125
6.5.1. Surface Morphology 125
6.5.2. Influence of Surface Treatment on Impact Performance 127
6.5.3. Post-Impact Failure Mode Analysis 132
6.5.4. Experimental vs numerical analysis 135
6.5.5. Failure modes analysis 138
6.6. Concluding Remark 142
CHAPTER SEVEN 144

7. CONCLUSION, CONTRIBUTIONS, AND RECOMMENDATIONS 144
7.1. Conclusions 144
7.2. Contributions of the study 145
7.3. Limitations and Challenges 146
7.4. Recommendations for Future Work 146
APPENDICES (Supplementary data) 148
REFERENCES 152

LIST OF ABBREVIATIONS

AF	**A**ramid **F**iber
AFM	**A**tomic **F**orce **M**icroscopy
ASTM	**A**merican **S**ociety for **T**esting and **M**aterials
B-K	**B**enzeggagh–**K**enane
BF	**B**asalt **F**iber
C	**C**ompliance
CAE	**C**omputer-**A**ided **E**ngineering
CC	**C**ompliance **C**oefficient
CF	**C**arbon **F**iber
CFRP	**C**arbon **F**iber **R**einforced **P**olymer
CMCs	**C**eramic **M**etal **C**omposites
CNC	**C**ellulose **N**anocrystal
CNF	**C**ellulose **N**anofiber
CNT	**C**arbon **N**anotube
CZM	**C**ohesive **Z**one **M**odeling
DCB	**D**ouble **C**antilever **B**eam
DIC	**D**igital **I**mage **C**orrelation
EA	**E**nergy **A**bsorption
ENF	**E**nd-**N**otched **F**lexure
EP	**E**poxy
FE	**F**inite **E**lement
FEA	**F**inite **E**lement **A**nalysis
FESEM	**F**ield **E**mission **S**canning **E**lectron **M**icroscope
FRP	**F**iber **R**einforced **P**olymer
GF	**G**lass **F**iber
GFRP	**G**lass **F**iber **R**einforced **P**olymer
GO	**G**raphene **O**xide
ILSS	**I**nterlaminar **S**hear **S**trength.
LCA	**L**ife **C**ycle **A**ssessment.

MDA	**M**ethylenedianiline
MMCs	**M**etal **M**atrix **C**omposites
MWCNT	**M**ulti-**W**alled **C**arbon **N**anotube
NCs	**N**anocelluloses
NFRPC	**N**atural **F**iber **R**einforced **P**olymer **C**omposite
PHA	**P**olyhydroxyalkanoates
PLA	**P**olylactic **A**cid
PMCs	**P**olymer **M**atrix **C**omposites
SDG	**S**ustainable **D**evelopment **G**oals
SDEG	**S**calar **D**egradation
SEA	**S**pecific **E**nergy **A**bsorption
SEM	**S**canning **E**lectron **M**icroscopy
TEMPO	**T**etramethylpiperidine-1-oxyl
UD	**U**nidirectional
UTM	**U**niversal **T**esting **M**achine
XPS	**X**-ray **P**hotoelectron **S**pectroscopy

LIST OF SYMBOLS

E	Young's modulus
G	Shear modulus
ν	Poisson's ratio
ρ	Density
t	Thickness of sub-laminate
σ	Stress
δ	Displacement
P_{max}	Maximum load
G_I	Mode I fracture toughness
G_{II}	Mode II fracture toughness
a_0	Crack length
Δa	Crack extension
R	Crack resistance
EA	Energy Absorption
m	Mass of the specimen
δ_f	Separation at complete failure
δ_0	Displacement at damage initiation
δ_c	Critical separation
K	Interface stiffness
D	Damage variable
t_{nn}	Nominal normal traction
t_{ss}	Nominal shear traction in the first shear direction
t_{tt}	Nominal shear traction in the second shear direction
G_{IC}	Critical Mode I energy release rate
G_{IIC}	Critical Mode II energy release rate
τ	Shear stress
G_C	Compressive fracture energy

G_T	Tensile fracture energy
PF	Peak force
L	Specimen length
M_t	Moisture uptake at time t
W_t	Weight of the composite after time *t*
W_0	Initial dry weight of the composite

DEFINITIONS OF IMPORTANT TERMS

Abaqus: A commercial finite element analysis software package used in this study to model, simulate, and analyze the mechanical and dynamic behavior of BFRP composite structures.

Aspect Ratio: The ratio of length to diameter of a fiber or nanomaterial.

Basalt Fiber–Reinforced Polymer: A composite material consisting of basalt fibers embedded in an epoxy matrix.

Boundary Conditions: Constraints and loading conditions applied to a numerical model to represent real-world physical behavior.

Cellulose Nanocrystals: Rod-like nanostructures extracted from cellulose, characterized by high crystallinity and stiffness.

Cellulose Nanofibrils: Flexible, high-aspect-ratio cellulose nanomaterials composed of entangled fibrils with both crystalline and amorphous regions.

Cohesive Zone Modeling: A numerical approach used to simulate interfacial damage and delamination by defining traction–separation laws.

Damage Tolerance: The ability of a composite material to sustain damage without catastrophic failure while maintaining structural integrity.

Delamination: The separation of layers within a laminated composite under mechanical or environmental loading.

Dynamic Loading: Time-dependent loading conditions applied to a structure, such as impact or vibration.

Element Type: The specific finite element formulation used in a numerical model, such as shell, solid, or cohesive elements.

Energy Absorption: The capacity of a material or structure to absorb mechanical energy during impact or dynamic loading.

Fiber–Matrix Interface: The region of interaction between reinforcing fibers and the surrounding polymer matrix that controls load transfer and damage initiation.

Finite Element Analysis: A numerical method that discretizes a structure into finite elements to predict mechanical and dynamic responses under defined loading and boundary conditions.

Grafting: A surface modification technique in which nanomaterials are chemically bonded to fiber surfaces to enhance interfacial adhesion.

Hat-Shaped Structure: A formed composite structural component used in this study to evaluate the dynamic impact performance at the structural level.

Interfacial Bonding: The adhesion or interaction between reinforcement and the polymer matrix that governs load transfer in composites.

Interlaminar Shear Strength: A measure of a composite's resistance to shear failure between laminate layers.

Load Transfer Mechanism: The process by which applied stresses are transferred from the polymer matrix to the reinforcing fibers through the interface.

Nanocellulose: Cellulose-derived nanomaterials used as interfacial modifiers in the composite systems.

Numerical Modeling: The use of computational techniques, including finite element methods, to simulate material and structural performance.

Mesh: The discretized representation of a structure into finite elements used in numerical simulations.

Model Validation: The process of assessing numerical model accuracy by comparing simulation results with experimental data.

Silane Coupling Agent: A chemical compound used to improve bonding between inorganic fibers and organic polymer matrices.

LIST OF FIGURES

Fig. 2.1. Conceptual framework of the literature review and research focus 12

Fig. 2.2. Development of composite materials 14

Fig. 2.3. Basalt rock formation 17

Fig. 2.4. Schematic illustration showing the manufacturing process of BF 18

Fig. 2.5. Various forms of BF finished products: (a) Chopped BF, (b) Continuous BF, and (c) Woven mat BF 19

Fig. 2.6. Chemical composition of BF 21

Fig. 2.7. Key areas of BF application: (a) Building and construction, (b) Fire-resistant doors, (c) Wind turbine blades, and (b) Radioactive storage container 22

Fig. 2.8. Key energy absorbing components in automotive structural design 28

Fig. 2.9. Different methods of improving the interfacial bonding strength of BF 29

Fig. 2.10. Mechanical performances of carbon/basalt fiber hybrid composite: (a) Tensile strength, (b) Impact energy, (c) Flexural strength, (d) Hardness number 32

Fig. 2.11. Structure of cellulose 36

Fig. 2.12. Morphology of Nanocelluloses: (a) CNC and (b) CNF 37

Fig. 2.13. Bilinear traction-separation law for cohesive modeling: (a) Opening mode and (b) Sharing mode 49

Fig. 3.1. Research methodology framework for the development of NC-modified BFRP composites for automobile applications 60

Fig. 4.1. Common damage mechanisms in BFRP composite: (a) fiber debonding and (b) interfacial delamination 62

Fig. 4.2. Mechanical stirring setup for dispersion of NCs into epoxy resin 66

Fig. 4.3. Tensile strength and stiffness of BFRPs at different concentrations of NCs in epoxy matrix: (a & b) CNC and (c & d) CNF 70

Fig. 4.4. ILSS and Shear stress-displacement curve at different concentrations of NCs in epoxy matrix: (a & b) CNC and (c & d) CNF 73

Fig. 4.5. Microstructural fractured surfaces of BFRPs after the ILSS test at different concentrations of NCs in epoxy resin: (a) Reference, (b) CNC, and (c) CNF 74

Fig. 4.6. Izod impact strength of BFRPs at different concentrations of NCs in epoxy resin: (a) CNC and (a) CNF 75

Fig. 5.1. Homogeneous dispersion of NCs in aqueous solution 78

Fig. 5.2. Schematic representation of the NCs-grafted BFRP process 80

Fig. 5.3. Schematic diagram for the silane functionalization process and the bonding mechanism of nanocellulose on BF surfaces 80

Fig. 5.4. Specimen testing configuration (a) DCB and (b) ENF 85

Fig. 5.5. DCB experimental setup 85

Fig. 5.6. Compliance coefficient determination 86

Fig. 5.7. XPS spectra results: (a) Survey spectrum, (b) Pristine BF, (c) Flame treated BF, (d) Silane treated BF, (e) CNC powder, (f) CNC-grafted BF, (g) CNF powder, and (h) CNF-grafted BF 91

Fig. 5.8. Stress-strain curve of BFRPs at different concentrations of NCs in the grafting solution: (a) CNC and (b) CNF 93

Fig. 5.9. Tensile strength and stiffness of BFRPs at different concentrations of NCs in the grafting solution: (a & b) CNC and (c & d) CNF 94

Fig. 5.10. ILSS and Shear stress-displacement curve at different concentrations of NCs in the grafting solution: (a & b) CNC and (c & d) CNF 96

Fig. 5.11. Microstructural fractured surfaces of BFRP after the ILSS test at different concentrations of NCs in the grafting solution: (a) 0.5 wt.%, (b) 1 wt.%, (c) 1.5 wt.%, and (d) 2 wt.% 99

Fig. 5.12. Impact fractured surfaces of the NC-grafted BFRP at different concentrations: (a) Reference, (b) CNC, and (c) CNF 102

Fig. 5.13. Moisture absorption curves for the optimum NCs-grafted and reference BFRP 103

Fig. 5.14. Moisture absorption effects on mechanical properties of NCs-modified BFRP after 168 h at 50 °C: (a) Tensile strength, (b) Stiffness, (c) ILSS, and (d) Izod impact strength 105

Fig. 5.15. Fracture toughness of BFRP: (a) Mode I and Mode II, (b) Force-displacement curve for Mode I testing, (c) Fiber bridging mechanism in NC-grafted BFRP 108

Fig. 5.16. (a) Mode I resistance curve, (b) Mode II force-displacement curves (NPC), and (c) Mode II force-displacement curves (PC) 108

Fig. 6.1. Specimen geometry for the hat-shaped profile 115

Fig. 6.2. Composite layup definition and fiber orientation for twill-woven BFRP hat-shaped component 118

Fig. 6.3. Meshing style between the composite and cohesive element 119

Fig. 6.4. Mesh refinement at the curvature 120

Fig. 6.5. FEA Model: (a) Loading condition, (b) Specimen geometry 121

Fig. 6.6. Fabrication process of hat-shaped BFRP composite 123

Fig. 6.7. Schematic arrangement of the experimental setup for dynamic impact testing of hat-shaped BFRP composite 124

Fig. 6.8. SEM images of CNC grafting process: (a) Pristine BF, (b) Flame-treated BF, (c) Silane-coated BF, (d) CNC-coated BF 126

Fig. 6.9. Energy-displacement curves for both CNC-modified and unmodified BFRP at varying span lengths: (a) 80 mm, (b) 140 mm, (c) 200 mm 130

Fig. 6.10. Experimental failure patterns in both CNC-modified and unmodified BFRP at different span lengths: (a) 200 mm, (b) 140 mm, (c) 80 mm 134

Fig. 6.11. Comparison of experimental and simulated force–displacement responses for the six test cases..... 136

Fig. 6.12. Experimental and numerical results for CNC-modified and unmodified BFRP composites: (a) Peak force, (b) Energy absorption 138

Fig. 6.13. Correlation of experimental and numerical failure patterns in BFRP Structures at different span lengths: (a) 200 mm, (b) 140 mm, (c) 80 mm..... 140

Fig. 6.14. Deformation pattern of BFRP under dynamic impact: (a) Experimental, (b) Simulation 140

Fig. 6.15. Comparative post-impact deformation patterns of hat-shaped BFRP composites (80 mm span) from experiment and simulation: (a) Unmodified specimen, (b) CNC-modified specimen 142

Fig. A1. Compressive test result of the optimized CNC-modified and unmodified BFRP: (a) Compressive strength, (b) Compressive stiffness, (c) Stress-strain curves (modified BFRP), and (d) Stress-strain curves (unmodified BFRP)..... 149

Fig. A2. Mold design for the fabrication of the hat-shaped BFRP composite 150

Fig. A3. Schematic side view of the dynamic impact testing configuration and specimen dimension. 151

Fig. A4. Crushing efficiency comparison between CNC-modified and unmodified BFRP at varying span lengths 151

LIST OF TABLES

Table 1.1. Comparative sustainability and economic assessment of common reinforcing fibers.3

Table 1.2. Comparison of the mechanical properties of BF with conventional fibers..... 4

Table 2.1. Physical and mechanical properties of selected thermosetting resins..... 26

Table 2.2. The weight ratio of the BF/CF hybrid composite 31

Table 2.3. Physicochemical properties of nanocellulose 37

Table 2.4. Mapping of identified research gaps to the present study..... 52

Table 2.5. Quantitative comparison of interfacial modification strategies on the performance of BF-based composites 55

Table 4.1. Fiber volume fraction and void content in NC-mixed BFRP composites..... 71

Table 5.1. Atomic composition of NC powders and BF after grafting processes..... 92

Table 6.1. Test cases for both CNC-modified and unmodified BFRP at various span lengths....113

Table 6.2. Input material properties for the FE model 117

Table 6.3. Statistical significance results from two-sample t-tests (assuming unequal variances) for three span lengths 131

Table 6.4. Experimental and numerical results of the dynamic impact analysis 132

Table 6.5. Experimental validation of numerical EA prediction in modified and unmodified BFRP Composites at varying span lengths 138

Table A 1. Calculated compliance and compliance coefficient values for the tested NC-modified and unmodified BFRP specimens……148

Table A 2. Mesh convergence analysis of the FEA model for the representative case (80 mm span length)……..150

LIST OF PUBLICATIONS

Peer-reviewed journal publications:

Musa AA, Kim MG, Jaiswal AP, Ho-Nguyen-Tan T, Yu J, Yoon SH, Onwualu AP, Kim M. (2026) Experimental and numerical investigation on the dynamic impact response of hat-shaped basalt fiber-reinforced polymer composite structures with improved interfacial properties. *Polymer Composites* 1–17. https://doi.org/10.1002/pc.70964.

Musa AA, Park J, Hong G, Yoon SH, Onwualu AP, Kim M. (2025). Development of high-performance basalt fiber-reinforced polymer composite using a nanocellulose-based surface modification strategy. *Composites Part A: Applied Science and Manufacturing*. 23:109191. https://doi.org/10.1016/j.compositesa.2025.109191.

Musa AA, Bello A, Adams SM, Onwualu AP, Anye VC, Bello KA, Obianyo II. (2025). Nano-enhanced polymer composite materials: a review of current advancements and challenges. *Polymers*. 26;17(7):893. https://doi.org/10.3390/polym17070893.

Musa AA, Onwualu AP. (2025). Potential of lignocellulosic fiber reinforced polymer composites for automobile parts production: Current knowledge, research needs, and future direction. *Heliyon*. 15;10(3). https://doi.org/10.1016/j.heliyon.2024.e24683.

Conference presentations:

Musa AA, Yoon SH, Onwualu AP, Kim M. Energy Absorption Behavior of Hat-Shaped Basalt Fiber-Reinforced Composites: Numerical and Experimental Analysis. Spring conference, Korean Society for Composite Materials (KSCM), Republic of Korea. 30th April – 2nd May, 2025.

Musa AA, Holzschuher M, Yoon SH, Onwualu AP, Kim M. Nano-enhanced basalt fiber-reinforced polymer composite: A sustainable solution for lightweight structural applications. Fall conference, KSCM, Republic of Korea. 13th – 15th November, 2024.

Musa AA, Park J, Yoon SH, Onwualu AP, Kim M. Enhancing the impact strength of basalt fiber-reinforced polymer composite for structural applications. Spring conference, KSCM, Republic of Korea. 26th – 30th April, 2024.

CHAPTER ONE

1. INTRODUCTION

1.1. Background

The increasing demand for lightweight, high-performance, and sustainable materials in many critical industries has driven the development of eco-friendly composite materials. BFs, derived from natural volcanic rock, offer advantages such as high strength, corrosion resistance, and recyclability, making them a suitable alternative reinforcement material for polymer composites [1–3]. However, improving the interfacial bonding between BF and polymer matrices remains a serious challenge. Nanocellulose, known for its high surface area, high density of hydroxyl groups (OH), and reinforcing capabilities, presents an opportunity to enhance the mechanical and interfacial properties of BFRP composites while maintaining processability and eco-friendliness [4,5]. This research aims to develop and optimize the performance of BFRP composites tailored for automotive structural applications, ensuring a balance between cost-effectiveness and environmental advantages.

Over the past few decades, the automotive industry has relied heavily on materials such as steel, aluminum, and other lightweight metals to achieve optimal performance, safety, and cost efficiency. In addition to these traditional materials, synthetic fiber-reinforced composites, particularly those incorporating carbon and glass fibers, have been extensively used in vehicle manufacturing [6,7]. Carbon fiber-reinforced polymer (CFRP) has gained significant attention due to its exceptional strength-to-weight ratio, high stiffness, superior damping properties, and design versatility compared to traditional metals [8,9]. However, with increasing emphasis on resource conservation, carbon footprint reduction, and green innovation, the industry is now shifting towards the development of environmentally friendly composite materials [10,11].

The focus is on creating high-performance alternative materials that not only enhance vehicle efficiency but also reduce environmental impact throughout their lifecycle.

Furthermore, the materials used must be lightweight and renewable to support the global transition toward a circular economy and enhanced fuel efficiency in the production of automobile components [12]. This shift is not driven solely by ethical or regulatory obligations, but also reflects a strategic response to an evolving market in which consumers and industry stakeholders increasingly demand cleaner and greener alternatives to conventional composite materials. As manufacturers and key players in the transportation sector strive to balance these technological advancements, regulatory requirements, and cost-effectiveness, the adoption of eco-friendly fiber materials offers a viable pathway to addressing the challenges of modern transportation while promoting long-term industry resilience [13].

Fiber-reinforced polymer (FRP) composites have gained significant attention across various industries, particularly in the transportation sector [14]. Their lightweight nature offers a crucial advantage by improving fuel efficiency and reducing carbon emissions, thereby contributing to the fight against global climate change [15–17]. Among FRP composites, CFRP and GFRP are the most widely used. However, GFRP suffers from relatively lower mechanical performance, while CFRP, despite its excellent strength and stiffness, is hindered by high production costs, recycling challenges, and environmental concerns, limiting its large-scale adoption [18–20]. The growing emphasis on environmental regulations has driven many industries and researchers to explore and develop more eco-friendly alternative composite materials. These efforts focus on utilizing natural-based reinforcement materials to overcome the limitations of conventional composites while maintaining high-performance standards. A comparative assessment of key sustainability indicators, including cost per kilogram, embodied

energy, recyclability, and CO_2 footprint, is presented in Table 1.1, sourced from [21] and [22], highlighting the limitations of conventional fibers and the advantages of emerging alternatives. Basalt fiber is a naturally occurring mineral fiber derived from basalt rock, recognized for its potential in advanced composite applications, particularly in the automotive and aerospace industries. Its appeal lies in a unique combination of high mechanical strength, thermal stability, chemical resistance, flame retardancy, eco-friendliness, cost-effectiveness, and ease of processing [20,23]. As shown in Table 1.1, BF offers a favorable balance between cost, environmental impact, and recyclability when compared with conventional carbon and glass fibers.

Table 1.1. Comparative sustainability and economic assessment of common reinforcing fibers [21,22]

Fiber type	**Approximate cost (USD/kg)**	**CO_2 footprint (kg CO_2-eq/kg)**	**Embodied Energy (MJ/kg)**	**Recyclability**
Carbon	20–40	22–30	180-250	Difficult
E-glass	2–5	4–8	25-30	Moderate
Basalt	3–6	0.98–3.87	15-18	Good
Natural	0.5–3	0.5–2	–	Very good

In addition, studies have shown that BF outperform E-glass fibers in mechanical properties while offering a higher failure strain compared to CF, as reported by Jagadeesh et al. [23] and Bhat et al. [24] and presented in Table 1.2, making them a promising alternative. This balance between performance and affordability has positioned BF as an intermediate option between GF and CF, with added environmental benefits [25]. Despite its numerous advantages, the poor compatibility of BFs with polymer resins remains a significant challenge, limiting their effectiveness in composite production. This weak interfacial adhesion often leads to inadequate load transfer between the fiber and the matrix. To overcome this limitation, various surface

modifications have been explored to enhance fiber-matrix bonding and improve overall composite properties. Developing effective strategies to address this issue is crucial for expanding the application of BFRP composites in high-performance industries such as automotive and aerospace. Notably, Balaji et al. [20] reviewed various surface treatments aimed at improving BF–matrix interfacial bonding for automotive applications, highlighting that techniques such as silane treatment, plasma treatment, and nanoparticle coating significantly enhance the BF–matrix interphase. Similarly, Balaji et al. [26] explored the use of carbon nanotubes (CNTs) and graphene (G) as effective reinforcements to enhance the interfacial bonding between BF and polymer matrices, leading to significant improvements in composite performance. Dhand et al. [1] conducted an in-depth analysis of BF as a viable alternative reinforcement material, discussing its fundamental chemical composition, characterization techniques, and the growing research interest in BF-reinforced polymer composites.

Table 1.2. Comparison of the mechanical properties of BF with conventional fibers [23,24]

Fiber	**Density (g/cm^3)**	**Tensile strength (GPa)**	**Young's Modulus (GPa)**	**Elongation at break (%)**
E-glass	2.56	1.4-2.5	76	1.8-3.2
Carbon	1.4	4	230-240	1.4-1.8
Basalt	2.5-2.8	2.8	89	3.15

The poor interfacial bonding of BFRP composites has been widely recognized as a major obstacle limiting their widespread adoption in composite fabrication, especially when compared to conventional fibers. Weak fiber-matrix adhesion reduces the efficiency of load transfer, leading to compromised mechanical properties and limiting their use in high-performance applications. Despite significant research efforts to improve interfacial bonding through various surface treatments and matrix modifications, most studies have primarily focused on enhancing

mechanical performance without fully considering the environmental implications of the resulting composites. Achieving this balance is crucial for advancing BFRPs as a truly environmentally sustainable alternative to conventional FRP composites. The current research explores an innovative surface treatment technique using bio-based surface treatment strategies that enhance composite performance without compromising its eco-friendliness.

1.2. Problem Statement

Basalt fibers offer several advantages for many applications, but their poor interfacial bonding with polymer matrices limits the mechanical performance of BFRP composites. Fiber–matrix interface plays a critical role in determining composite performance, yet conventional fiber treatments and reinforcement methods often fail to achieve an optimal balance between mechanical performance, cost-effectiveness, and environmental impact. Nanocellulose is a renewable, biodegradable, and relatively low-cost nanomaterial with excellent mechanical properties and a high density of hydroxyl groups [27], making it a promising candidate for enhancing interfacial adhesion between BF and epoxy resin. However, when NC is mixed directly into polymer resins, it tends to form gel-like suspensions, leading to poor dispersion and agglomeration, even at low concentrations. This also increases resin viscosity, making fiber impregnation difficult and limiting NC content to 0.01–1 wt.%, which results in only modest performance improvements, as reported by previous researchers [4,28–30].

Additionally, prior studies have largely focused on matrix-based NC incorporation [31,32], with limited attention given to direct fiber surface functionalization as a means of controlling NC placement at the critical load-transfer interface. This represents an important research gap. To address this limitation, the present study proposes an innovative surface modification approach in which NC is grafted directly onto the BF surface before composite fabrication. Unlike

conventional mixing methods, this approach is intended to improve NC distribution at the fiber–matrix interface, enhance interfacial bonding efficiency, and maximize the mechanical performance of BFRP composites. The effectiveness of this method is evaluated against both the conventional NC mixing approach and unmodified BFRP composites.

1.3. Research Questions

In order to study the interfacial behavior, mechanical performance, and structural suitability of NC-modified BFRP composites for automotive structural applications, the following research questions are addressed.

i. How can NC be effectively incorporated as an interfacial modification agent in BFRP composites?
ii. How do variations in NC morphology influence the fiber–matrix interfacial bonding in BFRP composites?
iii. What mechanisms govern the resulting improvements in the mechanical performance and durability of NC-modified BFRP composites?
iv. How does NC-enabled interface engineering affect the mechanical properties of the developed BFRP composites, and which properties show the greatest sensitivity to enhanced interfacial bonding?
v. What insights do surface characterization techniques, such as SEM and XPS, provide about the interfacial bonding and strengthening mechanisms in the modified BFRP composites?
vi. How suitable is the optimized NC-modified BFRP composite for automotive structural applications, and how well do numerical simulations predict its dynamic behavior?

1.4. Research Aim and Objectives

The main objective of this study is to develop and evaluate BFRP composites modified with NCs for enhanced interfacial performance and mechanical properties, and to evaluate their structural suitability for automotive applications.

To achieve this aim, the specific objectives are to:

i. Develop a grafting strategy for anchoring nanocellulose onto silane-functionalized basalt fiber surfaces to improve interfacial compatibility.
ii. Investigate the effect of nanocellulose type (CNC and CNF) on the interfacial bonding behavior of BFRP composites.
iii. Characterize the mechanical properties of the developed composites, including tensile strength, flexural strength, and interlaminar shear strength.
iv. Analyze the microstructural features of the modified fiber-matrix interface using appropriate characterization techniques.
v. Evaluate the durability performance of the composites, particularly the moisture absorption behavior and its effect on mechanical properties.
vi. Assess the suitability of the developed composites for structural and automotive applications through experimental and numerical analysis.
vii. Simulate the mechanical response and interfacial damage behavior of the composites using FE modeling.

1.5. Scope of the Study

This study focuses on improving the interfacial properties and overall mechanical performance of BFRP composites through the use of NC as a surface modification agent. The scope encompasses the development and evaluation of an innovative NC grafting approach for

basalt fiber surfaces to overcome dispersion limitations associated with conventional direct-mixing methods. Comprehensive chemical, surface, and mechanical characterizations are carried out to assess the effectiveness of the modification and its influence on fiber–matrix interactions, composite performance, and failure behavior. In addition, the applicability of the modified BFRP composites for automotive applications, particularly in terms of crashworthiness, is evaluated. Accordingly, the scope of the study is structured as follows:

i. Enhance the interfacial bonding and mechanical performance of the BF/epoxy composite, using NC as a surface modification agent.
ii. Development of an innovative NC grafting technique onto the BF surface to address the dispersion challenges often encountered with the direct-mixing method.
iii. Examines the chemical bonding and surface composition of NC and NC-grafted BF using XPS analysis, offering insights into the success and effectiveness of the grafting process.
iv. Conduct mechanical characterization, including tensile strength, impact resistance, interlaminar shear strength (ILSS), and fracture toughness, to quantify the impact of NC modification on BFRP composites.
v. Conduct surface characterization using SEM analysis to examine fiber-matrix interactions, NC dispersion, and failure mechanisms in the composites.
vi. Assess the potential of BFRP composites for automotive applications, focusing on crashworthiness.

1.6. Significance/Justification of the Study

The increasing demand for lightweight, high-performance, and sustainable materials has driven interest in basalt fiber–reinforced polymer (BFRP) composites for structural and automotive applications. Despite their advantages, the broader application of BFRP composites

is constrained by weak fiber–matrix interfacial bonding and limited energy-absorption capability. This study addresses these limitations by employing nanocellulose (NC), a renewable and environmentally friendly nanomaterial, as a surface modification agent to enhance interfacial interactions and mechanical performance. The significance of this research lies in the development of an innovative NC grafting technique for basalt fiber surfaces, which overcomes dispersion challenges associated with conventional direct-mixing methods and leads to improved mechanical properties and crashworthiness. The findings provide valuable insights into fiber–matrix interactions and failure mechanisms, supporting the design of advanced composite materials for automotive structural applications. This research aligns with several United Nations Sustainable Development Goals (SDGs). It contributes to SDG 9 by promoting innovation in material design for industrial infrastructure. It supports SDG 12 through the use of renewable materials (i.e., basalt fibers and nanocelluloses), encouraging responsible and environmentally sustainable materials production. Finally, it addresses SDG 13 by enabling lightweight composite materials that can help reduce vehicle fuel consumption and associated carbon emissions.

1.7. Dissertation Layout

This dissertation is organized into seven chapters, each addressing a specific aspect of the research:

Chapter one provides background information on the study, clearly defines the research problem, and outlines the study's objectives. It also establishes the scope of the study, highlighting its limitations and boundaries, and provides an overview of the entire dissertation structure to guide the reader through the research process.

Chapter two reviews relevant literature on FRP composites, with a focus on BF and recent advancements in BFRP composites. It critically examines previous studies, theories, and key findings in the field, highlighting significant contributions and areas of consensus.

Chapter Three provides an overview of the research's methodological framework. It highlights the materials and equipment used and explains the characterization procedures employed to analyze the results.

Chapter four explores the effect of direct mixing of NCs (CNC and CNF) and epoxy resin on the performance of BFRP composites. It details the preparation process, including dispersion techniques, mixing parameters, and associated challenges. The influence of NC dispersion on the mechanical and morphological properties of the composite was evaluated through various experimental tests, including tensile, impact, and short beam shear tests.

Chapter five focuses on the NC grafting technique used to enhance the interfacial bonding strength between BF and epoxy resin. It provides an in-depth explanation of the surface modification approach, including chemical treatment, silane functionalization, and surface characterization of the treated fibers. The chapter also examines the effects of this modification on fiber–matrix adhesion by analyzing improvements in mechanical performance.

Chapter six covers the FE modeling and experimental validation of BFRP hat-shaped components. It outlines the Abaqus modeling procedures and then describes the manufacturing and impact testing of both NC-modified and unmodified composites. The chapter concludes with a comparison of the simulation and experimental results to validate the FE model.

Chapter seven summarizes the key findings/contributions of the study, discusses its limitations, and outlines recommendations for future research based on the outcomes of the current work.

CHAPTER TWO

2. LITERATURE REVIEW

2.1. Overview of Literature Review

This chapter presents a comprehensive review of the literature related to the development and application of BFRP composites, with a particular focus on their role in automotive structural design. The automotive industry faces strict regulations regarding fuel efficiency and emissions, driving the need for lightweight yet crashworthy materials, as well as environmentally friendly [6,33]. BFRPs offer a potential solution, but their use in complex structural components, such as hat-shaped crash elements, remains relatively underexplored, as compared to other conventional FRPs. This review covers two key aspects aligned with the aim of the study: (1) the development and characterization of BFRP materials, and (2) the simulation and modeling approaches used to predict their structural behavior, particularly under crash or impact conditions. Emphasis is placed on hat-shaped structures due to their significance in energy absorption and structural reinforcement in automotive applications. Fig. 2.1 presents the conceptual framework guiding the literature review, illustrating the relationship between sustainable material development, interfacial enhancement strategies, and structural crashworthiness evaluation for automotive applications.

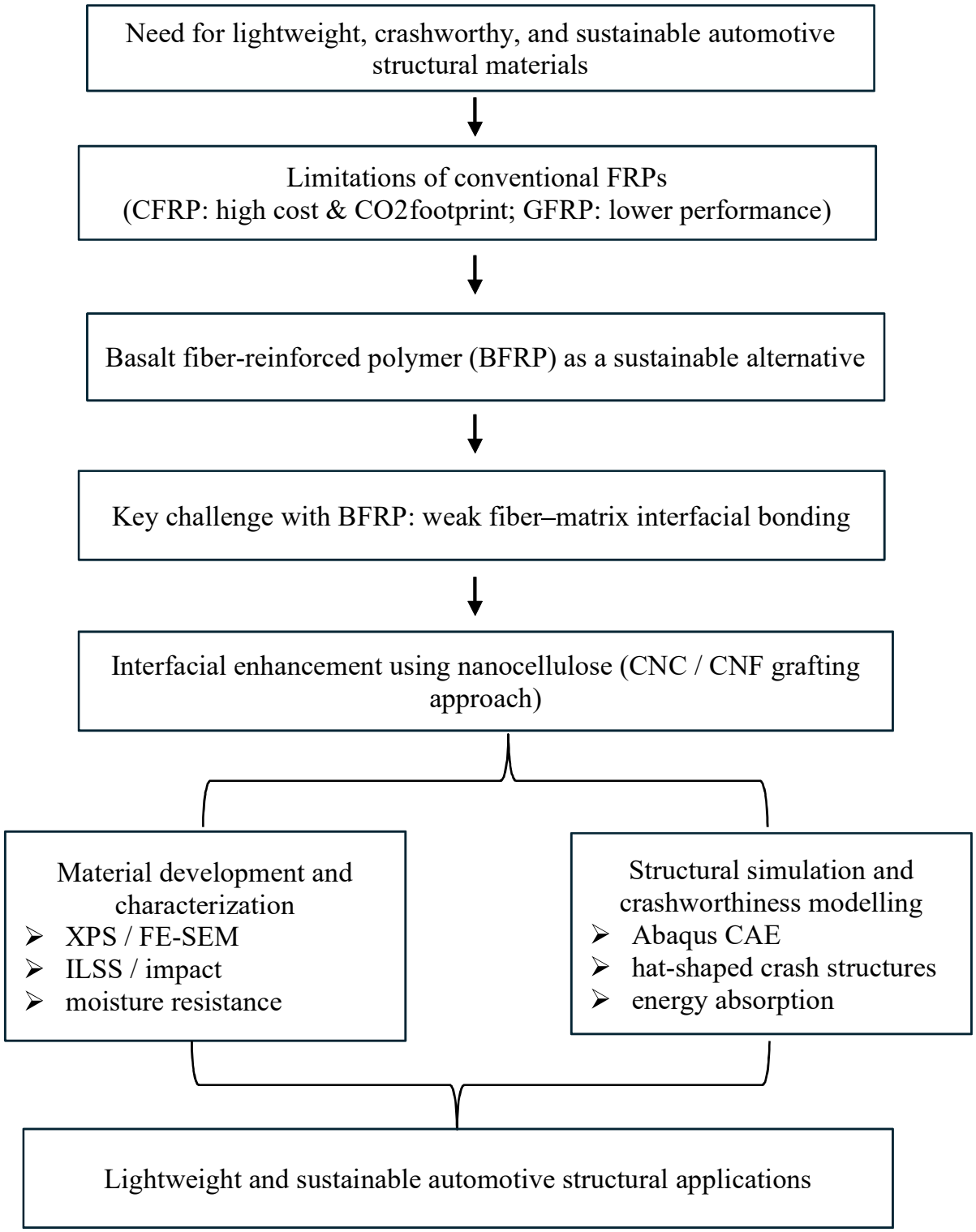

Fig. 2.1. Conceptual framework of the literature review and research focus

2.2. Composite Materials

The development of composite materials gained significant recognition in the mid-20th century, marking a shift toward the intentional design and engineering of heterogeneous materials to achieve an optimal combination of mechanical, thermal, chemical, and lightweight properties. One of the earliest and most widely adopted innovations in the field of fiber-reinforced polymer (FRP) composites is fiberglass-reinforced polymers (GFRPs). This material has revolutionized industries such as aerospace, automotive, and construction by providing a high-performance alternative to traditional materials such as metals and ceramics, owing to its high strength-to-weight ratio, corrosion resistance, and design flexibility [34]. Although some naturally occurring multiphase materials, such as wood, bone, seashells, and man-made materials like bricks made from straw-reinforced clay, have long existed [35], the deliberate combination of dissimilar materials with significantly different physical or chemical properties gave rise to the concept of composite materials. This approach has created a new class of materials with properties distinct from those of conventional monolithic materials such as metals, ceramics, and polymers. The concept of multiphase materials provides an exciting opportunity for the design and manufacture of a wide variety of materials with property combinations that cannot be achieved by conventional monolithic metal alloys, ceramics, or polymeric materials. Therefore, composites are materials composed of two or more physically distinct phases, combined to create a new material with enhanced properties surpassing those of the individual constituents [36,37]. These phases are typically classified as the matrix (which can be metal, ceramic, or polymer) and the reinforcement (such as fibers or particulates), as illustrated in Fig. 2.2. These two phases are typically referred to as matrix (metal, ceramic, or polymer) and reinforcement (fiber, particulate, etc.).

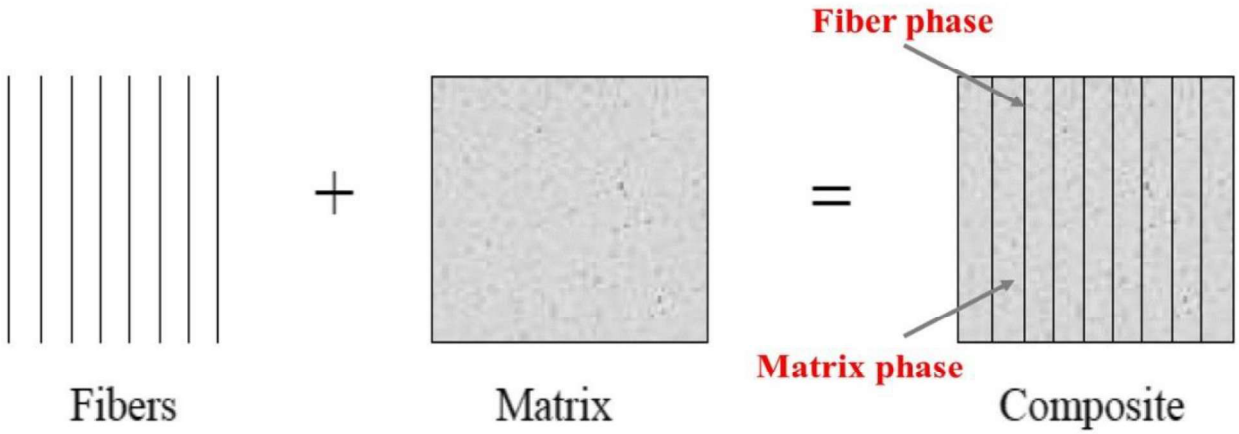

Fig. 2.2. Development of composite materials

Composites can be categorized based on the type of matrix material used, which plays a crucial role in determining their properties and applications. The three main classifications are metal matrix composites (MMCs), ceramic matrix composites (CMCs), and polymer matrix composites (PMCs). PMCs, which are composed of a polymer matrix such as epoxy, polyester, or thermoplastic resins, reinforced with fibers like glass fiber (GF), carbon fiber (CF), or aramid fiber (AF), have become highly popular among other composite types due to their exceptional properties [38]. These composites offer a high strength-to-weight ratio, corrosion resistance, durability, and ease of manufacturing, making them widely used in the aerospace, automotive, marine, and sporting goods industries. Their versatility and cost-effectiveness have established them as one of the most commonly used composite materials today.

Fiber-reinforced polymer (FRP) composites possess a unique combination of properties that govern their suitability for a wide range of applications. The overall performance of FRP composites is influenced by both the properties of these constituents and the strength of the bond between the fiber and matrix. Due to their exceptional mechanical properties and lightweight nature, FRP composites are widely utilized in engineering fields such as automotive and aerospace applications [39]. However, achieving high performance in FRP depends on effective

load transfer from the matrix to the fibers. Most of these fibers in their unmodified state displayed relatively weak fiber-matrix interface strength, which can limit the composite's overall strength and performance [4]. Modifications to the composite structure have been widely reported as a way of enhancing the interfacial bonding, leading to improved mechanical performance and broader application potential.

The growing demand for environmental sustainability in industries like automotive, aerospace, construction, and packaging has driven research into developing greener composites with improved recyclability and reduced energy consumption during and after production [40,41]. Sustainable composite materials are an emerging class of materials designed to reduce environmental impact while maintaining high performance [42,43]. These composites are made from renewable, biodegradable, or recycled materials, offering an eco-friendly alternative to traditional synthetic-based composites. They often incorporate natural fibers (such as flax, hemp, or jute) in polymer-based resins to minimize reliance on synthetic fiber materials [24]. However, natural fibers often fail to meet the stringent performance requirements necessary for critical applications, such as those in the automotive and construction industries. This limitation is primarily due to their lower mechanical strength, reduced thermal stability, and poor fire resistance compared to synthetic fibers [44]. Additionally, natural fibers tend to absorb moisture, which can lead to swelling, dimensional instability, and long-term material degradation. These challenges significantly hinder their use in high-performance applications, despite ongoing efforts to enhance their properties through various surface treatments and modifications. As a result, researchers continue to explore alternative fiber materials that are not only environmentally friendly but also offer enhanced mechanical strength, thermal stability, and fire resistance. The focus has increasingly shifted toward advanced natural-based fibers, such as

basalt fiber (BF), as viable substitutes for conventional synthetic fibers [20,26]. BF has gained significant research interest due to its eco-friendly advantage over traditional fibers like CF and GF. It exhibits excellent mechanical properties, high resistance to heat and chemicals, and improved durability, making it a promising reinforcement material for composite applications. Additionally, they produce fewer emissions during manufacturing, are non-toxic, and have better recyclability.

2.3. Brief History of Basalt

Basalt rock originates from volcanic magma associated with flood basalt eruptions. This magma is a very hot fluid or semi-fluid material found beneath the Earth's crust, which solidifies upon exposure to the open air. The resulting basalt rock typically appears black in color and features a fine-grained texture due to the rapid cooling of lava at the Earth's surface. An example of this typical appearance is illustrated in Fig. 2.3. The development of BF from basalt rock started as far back as the late 20th century, originating from research conducted at the Moscow Research Institute of Glass and Plastic in the former Soviet Union. Scientists sought to create a sustainable, high-performance material that could serve as an environmentally friendly alternative for various industrial applications [45,46]. During the 1970s and 1980s, BF production remained in the experimental phase, with early research focused on refining the extraction and manufacturing processes. By the 1990s, commercialization began as Russian and Ukrainian companies started producing and distributing BF on a larger scale. Its unique composition and eco-friendly nature have made it an attractive alternative to conventional fibers, offering a balance of high mechanical performance, thermal stability, and environmental benefits.

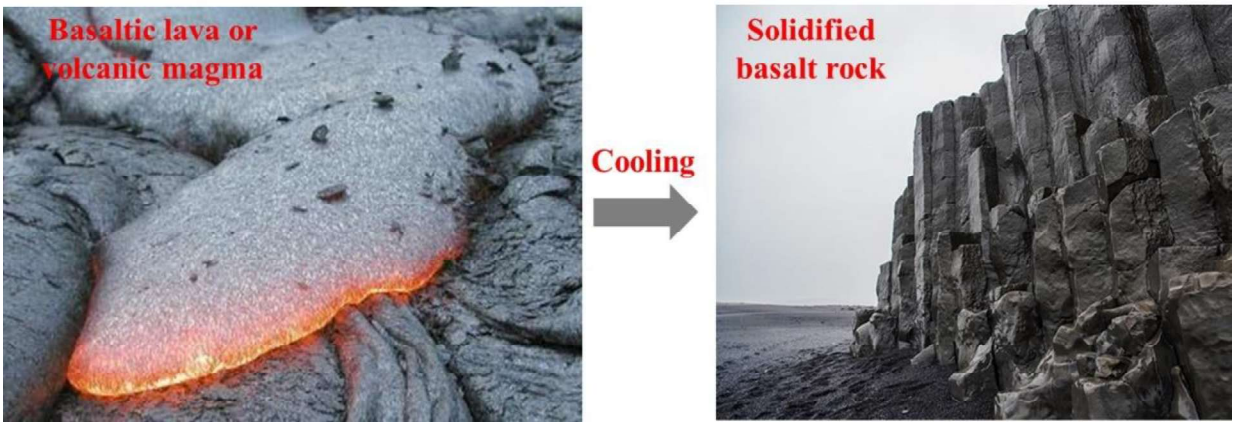

Fig. 2.3. Basalt rock formation [41]

The eco-friendliness and biocompatibility of BFs have been supported by several studies. Kogan et al. [49] conducted an inhalation study in which rats were exposed to air containing asbestos and basalt fibers for a duration of six months. For asbestos fibers, a dose of 1.7 g/kg (relative to the rats' body weight) resulted in the death of one-third of the test animals, while a dose of 2.7 g/kg proved fatal to all. In contrast, all rats exposed to basalt fibers survived, even at a much higher concentration of 10 g/kg. Similar findings were reported by McConnell et al. [50], who also concluded that basalt fibers pose no significant health risk to humans.

Despite these well-established advantages and the increasing adoption of BFs as an alternative to conventional synthetic fibers in structural applications, significant challenges remain with respect to their interfacial performance with polymer resins and long-term durability. In particular, inadequate interfacial adhesion between the BF reinforcement and the polymer matrix limits efficient stress transfer and adversely affects the mechanical properties of the composites. In addition, poor interfacial compatibility can accelerate moisture ingress and interfacial degradation, thereby compromising the durability and service life of the composite under operational conditions. Therefore, the motivation for the present study lies in addressing

the persistent interfacial limitations of BFRP composites through the development of a multifunctional interfacial modification approach capable of simultaneously enhancing adhesion, mechanical integrity, and environmental durability for demanding automotive applications.

2.4. Basalt Fiber Production and Chemical Characteristics

Basalt fiber is derived from naturally occurring volcanic rock formed from solidified lava and is produced through a series of processes, including mining, crushing, melting, fiber drawing, and subsequent finishing steps, as illustrated in Fig. 2.4. The process begins with the extraction of basalt rock from natural deposits, followed by crushing and thorough cleaning to remove impurities. The cleaned basalt rock is then transferred from the storage facility to a furnace, where it passes through multiple heating zones and is gradually heated until it reaches a fully molten state at temperatures typically ranging between 1400 °C and 1700 °C, depending on its composition and geographical origin [51].

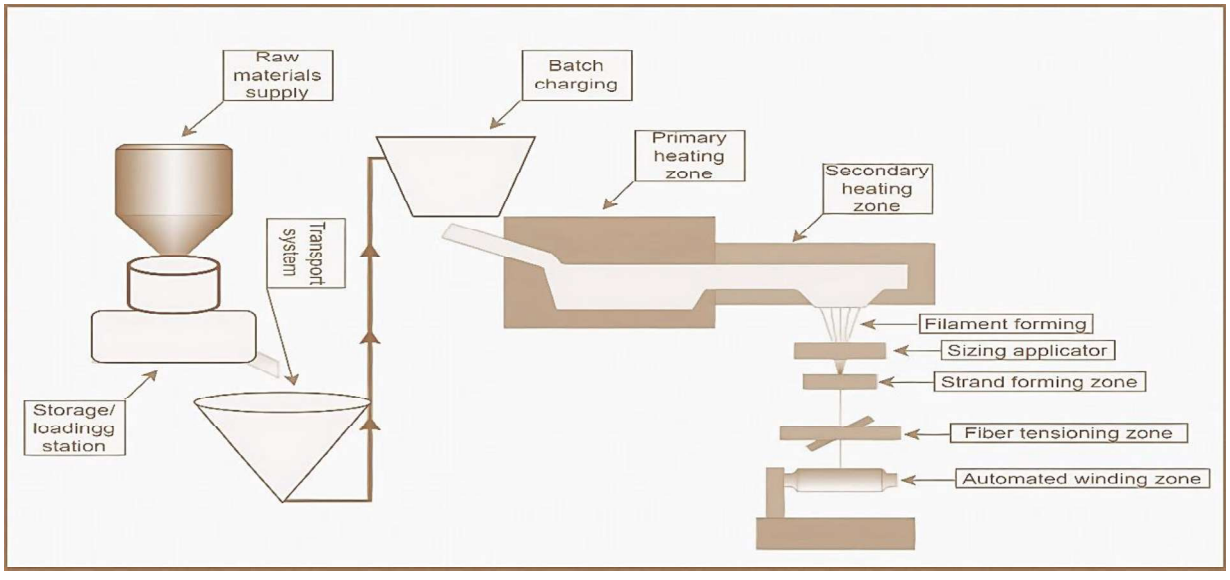

Fig. 2.4. Schematic illustration showing the manufacturing process of BF [45]

The molten basalt is subsequently extruded through fine platinum–rhodium nozzles to produce thin, continuous filaments. The resulting fibers are rapidly cooled and mechanically drawn to achieve the required filament diameter, which typically ranges from 9 to 24 μm, depending on the nozzle diameter and drawing speed. The final fiber diameter is primarily governed by the nozzle orifice size, melt viscosity, and take-up speed during the drawing process. To enhance surface characteristics and improve interfacial, mechanical, and thermal performance, the fibers may undergo additional treatments, such as the application of a sizing agent and/or controlled heat treatment. Depending on the intended application, the fibers can be further processed into different forms, including chopped fibers, continuous, and woven fabric mats, as shown in Fig. 2.5. Owing to its favorable mechanical properties, thermal stability, and environmental sustainability, BF is gaining increasing attention among researchers and manufacturers as a promising reinforcement material for composite production.

Fig. 2.5. Various forms of BF finished products: (a) Chopped BF, (b) Continuous BF, and (c) Woven mat BF [48]

Basalt rock is primarily composed of minerals such as plagioclase, pyroxene, and olivine, which contribute to its unique physical and chemical properties [52,53]. The chemical analysis of basalt rock shares several compositional similarities with E-glass fibers, with silica (SiO_2) being the dominant constituent, making up nearly half of the rock's total mass. Alumina (Al_2O_3) is the second most abundant component, along with other trace elements that influence the material's properties, as shown in Fig. 2.6. Basalt can also be classified based on its silica content, which aids in understanding its chemical composition and suitability for various industrial applications [54]. The classifications include:

a. Alkaline basalts: These contain a lower silica content, approximately 42%, and are typically rich in alkali oxides such as sodium (Na_2O) and potassium (K_2O). Alkaline basalts are commonly associated with volcanic activity in rift zones and oceanic islands.

b. Mildly acidic basalts: These have a silica content ranging between 43% and 46%. They exhibit a balanced composition, making them suitable for producing basalt fibers due to their optimal melting and processing properties

c. Acidic basalts: These often contain silica above 46%, placing them closer to the composition of andesitic rocks. Acidic basalts are often found in continental volcanic regions and have distinct physical and chemical properties that influence their industrial usability.

The main physical and mechanical properties of BF lie between those of CF and GF as presented in Table 1.1, making them very attractive, competitive, and alternative materials.

The mechanical strength, thermal resistance, and chemical stability of basalt fiber are largely dependent on variations in the chemical and elemental concentrations of the raw material. These factors play a crucial role in determining its suitability for different applications, including high-performance composite materials used in aerospace, automotive, and construction industries.

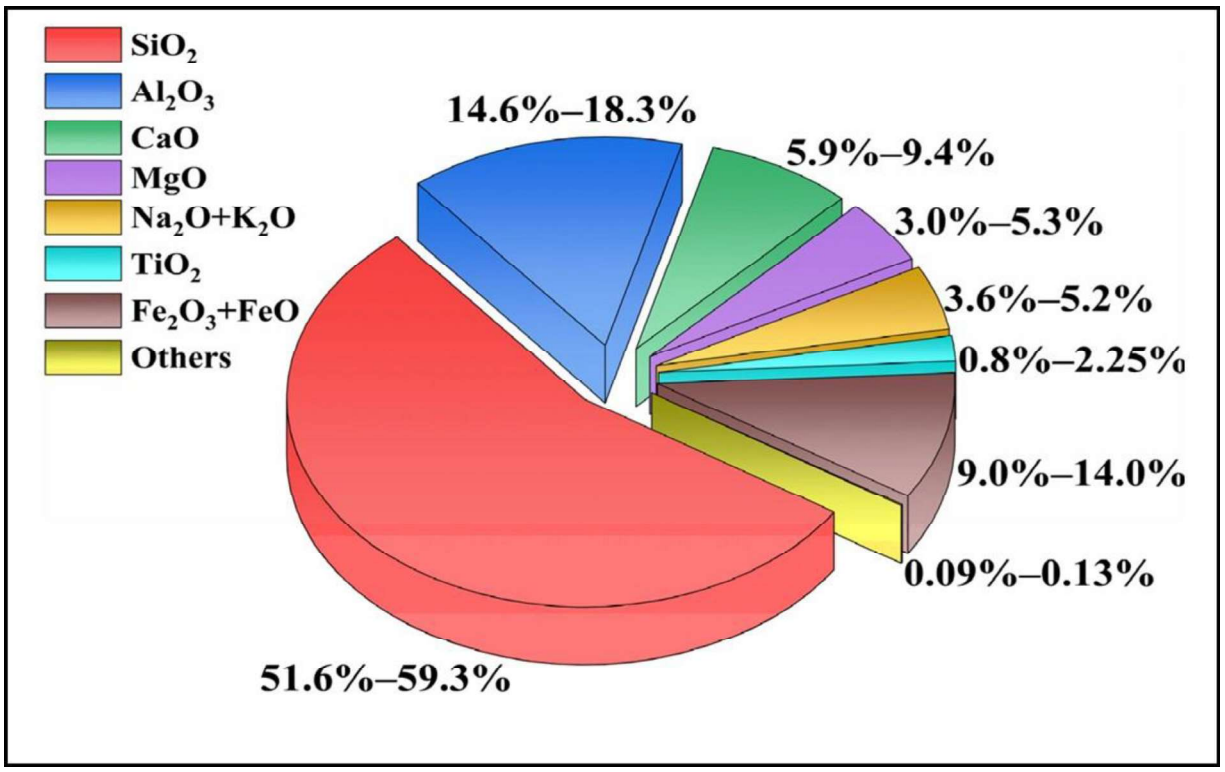

Fig. 2.6. Chemical composition of BF [55]

2.5. Application of Basalt Fiber

Basalt fibers are widely used across various industries due to their excellent mechanical properties, high thermal stability, and environmental sustainability. Their superior strength, corrosion resistance, and lightweight nature make them a suitable material for a broad range of applications. In the construction and building industry, BFs are utilized in reinforcing concrete structures, bridges, and road pavements, offering enhanced durability and crack resistance. Additionally, they are used in the production of flame-resistant and thermal insulation materials, including fireproof panels, protective coatings, and fire prevention doors, as shown in Fig. 2.7. These properties make BF an ideal choice for improving building safety and energy efficiency. BF has also been increasingly used in the manufacturing of wind turbine blades and propellers due to its higher fatigue resistance and better environmental durability than GF, while offering a

more cost-effective alternative to CF. The ability of BF to withstand mechanical stress and harsh weathering conditions makes it an exceptionally durable alternative to traditional materials such as CF and GF. This resilience is especially valuable in industries that require materials to endure extreme environmental factors and mechanical loads over long periods of time. Moreover, BF has also found critical applications in the nuclear industry, particularly for the fabrication of containers used to store radioactive wastes. BF exhibits excellent radiation resistance, allowing it to preserve its structural integrity and mechanical properties under prolonged radiation exposure [56]. This ability to resist degradation from radiation is crucial for the safe storage and transportation of hazardous substances. Furthermore, the long-term stability and non-toxic nature of BF enhance its appeal in industries requiring durable and environmentally friendly materials.

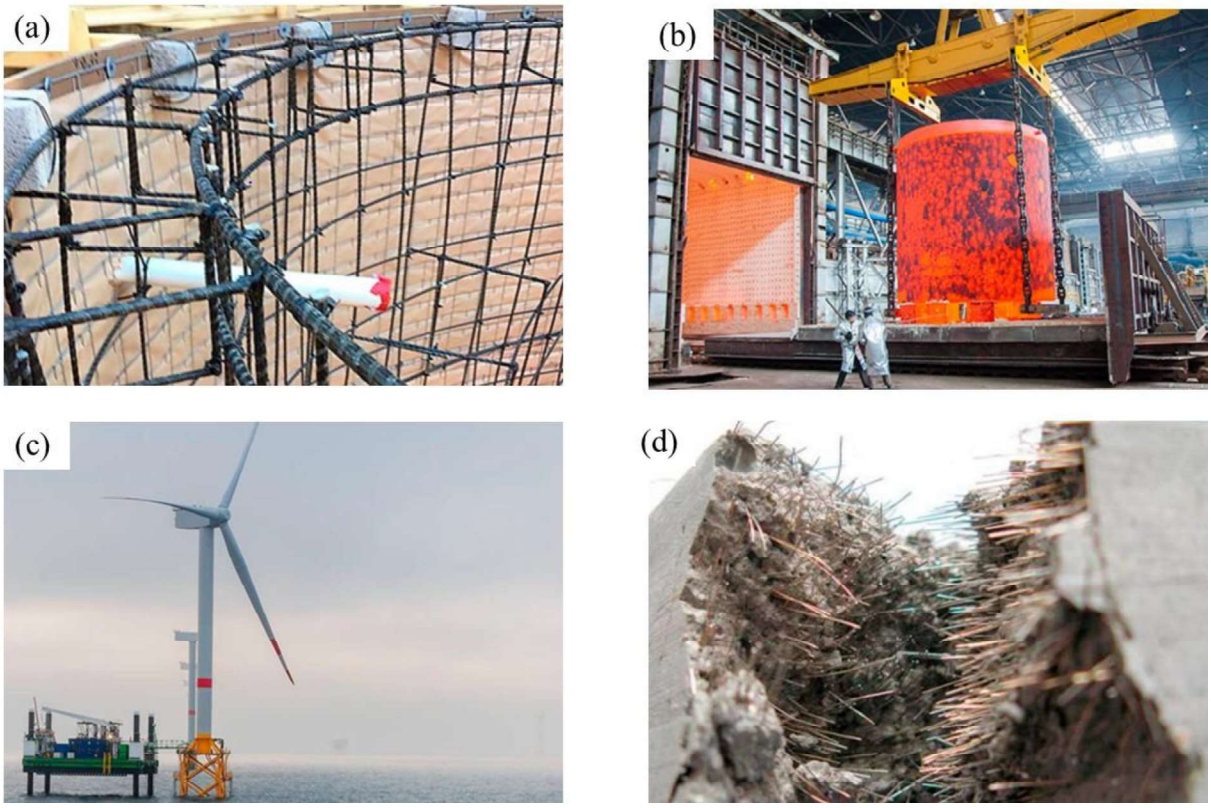

Fig. 2.7. Key areas of BF application: (a) Building and construction, (b) Fire-resistant doors, (c) Wind turbine blades, and (b) Radioactive storage container [57,58]

2.6. Basalt Fiber Reinforced Polymer (BFRP)

Basalt fiber reinforced polymer composite is a high-performance and emerging composite material that is created by embedding BFs within a polymer matrix, such as epoxy, polyester, vinyl ester resins, or biodegradable resins [23,43]. This innovative composite offers a compelling alternative to conventional GFRP and CFRP due to its superior balance of strength, durability, and environmental sustainability. The integration of BFs into a polymer matrix results in a lightweight yet exceptionally strong material with outstanding mechanical, thermal, and chemical resistance properties. Unlike traditional reinforcement materials, BF has the potential to strike a balance between high performance, lightweight properties, and environmental sustainability [59]. However, to fully harness its benefits, significant attention must be given to improving its compatibility with various polymer resins. The effectiveness of BFRP as a structural material largely depends on the interfacial bonding between the fiber and the polymer matrix [60,61]. A strong fiber-matrix adhesion translates to effective load transfer, resulting in enhanced mechanical performance and long-term durability. The limitation of BFRP in industrial applications has been attributed to the poor wettability, surface energy differences, and chemical incompatibility between BF and polymer resins [1]. To address these issues, researchers are actively exploring different surface modification techniques and matrix optimization strategies, such as chemical treatment [62], plasma and thermal treatments [63], nanoparticle coatings [64], as well as matrix selection. These methods modify the fiber surface morphology, increasing surface roughness and wettability, which enhances the interfacial bonding with polymer resins. The incorporation of CNTs, G, or silica nanoparticles in improving interfacial adhesion, mechanical properties, and durability has been widely reported in the literature [65,66].

However, in addition to their high cost, synthetic nanoparticles are often associated with health and environmental concerns, further complicating their widespread adoption in applications that prioritize sustainability. This challenge presents yet another bottleneck to their successful utilization. With ongoing advancements in manufacturing techniques and surface modification methods, BFRP has the potential to become a cost-effective and eco-friendly alternative to conventional fiber-reinforced polymers (FRPs). By enhancing fiber-matrix compatibility, optimizing production processes, and developing sustainable reinforcement strategies, BFRP could contribute significantly to the creation of high-performance, durable, and environmentally responsible composite materials across various industries.

2.6.1. Biodegradable Polymer

Biodegradable polymers are a class of materials designed to break down naturally over time through microbial activity, enzymatic reactions, or environmental exposure. These polymers decompose into non-toxic byproducts such as water, carbon dioxide, and biomass, making them an eco-friendly alternative to conventional plastics. Biodegradable polymers are commonly derived from natural sources, such as starch, cellulose, polylactic acid (PLA), and polyhydroxyalkanoates (PHA), or through synthetic routes designed to enhance degradation properties. Their use is gaining more popularity in packaging, biomedical applications, agriculture, and sustainable composite materials. When combined with natural fibers like BF, biodegradable fiber-reinforced composites can be produced, offering high-performance characteristics while ensuring environmental sustainability at the end of their lifecycle. However, challenges such as moisture sensitivity, limited mechanical performance, processing difficulty, and compatibility must be addressed to expand their industrial applications.

2.6.2. Synthetic-Based Polymer

Synthetic-based polymers are man-made materials produced from petroleum-based resources through polymerization processes. These polymers exhibit high durability, excellent mechanical strength, and superior thermal and chemical resistance, making them widely used in developing structural composites for construction purposes. Synthetic-based polymers commonly used in (FRP) composites include epoxy resins, polyester resins, vinyl ester resins, as well as thermoplastics such as polypropylene, polycarbonate, etc. The enhanced mechanical strength and thermal stability make them popular in composite production despite their environmental concerns and non-biodegradable nature.

2.6.3. Epoxy Resin

When making composite products, it is important to carefully choose the reinforcement materials, matrix components, and manufacturing methods to ensure the final product is strong, durable, and sustainable. The right combination of these elements helps improve mechanical performance, resistance to damage, and overall durability of the composite. The choice of reinforcement (such as BF, GF, or CF) and matrix material (such as epoxy, polyester, or thermoplastic resins) significantly influences the properties of the final composite products. Table 2.1 summarizes commonly used thermosetting resins and their properties. Epoxy resins are especially popular due to their high strength, chemical resistance, and thermal stability. The properties of the epoxy matrix also play a crucial role in determining damage mechanisms in composite structures. Some of the common failure modes in composites, such as fiber debonding or delamination, are usually determined by properties of the matrix material. Epoxy resins are widely used in polymer composite fabrication due to their low viscosity and moderate processing temperature, which allows for efficient fiber wetting and improved interfacial bonding with the

reinforcement material. Additionally, it exhibits excellent mechanical properties, including high strength, stiffness, and impact resistance, making it suitable for demanding structural applications [67,68]. They also offer superior chemical resistance, thermal stability, and minimal shrinkage during curing, which contribute to their widespread use in industries such as aerospace, automotive, marine, and construction.

Table 2.1. Physical and mechanical properties of selected thermosetting resins [69–72]

Properties	Polymer resin		
	Epoxy	**Vinyl ester**	**Polyester**
Density (g/cm^3)	1.2 – 1.4	1.15 – 1.35	1.1 – 1.4
Tensile strength (MPa)	55 – 130	73 – 81	34.5 – 104
Young's Modulus (GPa)	2.75 – 4.1	3.0 – 3.5	2.1 – 3.45
Poisson's ratio	0.38 – 0.40	0.36 – 0.39	0.35 – 0.39
Coefficient of Thermal Expansion (10^{-6}/°C)	45 – 65	50 – 75	55 – 100
Viscosity (mPa.s) at 25 °C	550	520 – 620	620

2.7. Potential of BFRPs in Automotive Structures

The automotive industry is undergoing a significant transformation, driven by stringent environmental regulations, fuel efficiency goals, and the global shift toward sustainable mobility [6]. In response, most vehicle manufacturers are increasingly turning to advanced composite materials that offer a combination of lightweighting potential, mechanical performance, and environmental benefits. BFRP composites have recently gained attention in this context due to their unique balance of strength, sustainability, and cost-effectiveness [26,55]. This section discusses the possible application of BFRPs in automotive structures, focusing on their role in lightweighting, crashworthiness, and performance relative to conventional FRP materials.

2.7.1. Lightweight and Sustainability Trends in Automotive

Reducing vehicle weight is a key strategy for enhancing fuel efficiency and lowering CO_2 emissions [73,74]. Traditional metallic materials such as steel and aluminum have good mechanical performance, but contribute significantly to vehicle weight. In contrast, FRP composites offer high strength-to-weight ratios, enabling substantial weight reductions without compromising structural integrity [75]. However, many commonly used FRP materials are not environmentally friendly and present challenges in terms of recyclability and end-of-life disposal. BF offers an eco-friendly alternative to synthetic fibers. In addition to weight savings, the use of BFRPs aligns with the global sustainability goal in the automotive and other related sectors. BFs are non-toxic, recyclable, and more abundant than CFs and GFs. Their lower embodied energy contributes to improved life cycle assessments (LCAs) of vehicles, particularly in electric and hybrid models, where every kilogram saved can directly extend battery range and reduce environmental impact.

2.7.2. Use of BFRP in Load-Bearing Components

One of the most promising uses of BFRP composites is in crash-resistant and load-bearing parts of a vehicle, such as bumper beams, side impact beams, and structural pillars. These components often include hat-shaped or tubular reinforcements (see Fig. 2.8), which are designed to absorb and manage impact energy to protect occupants during a collision. Research has shown that BFRP composites can deliver competitive energy absorption performance, especially when optimized through appropriate fiber orientations, suitable matrix selection, and enhanced fiber–matrix interfacial bonding. Their ability to undergo progressive failure mechanisms through delamination, fiber breakage, and matrix cracking allows for gradual

energy dissipation, which is highly beneficial in crash scenarios where controlled deformation is critical for the safety of the passengers.

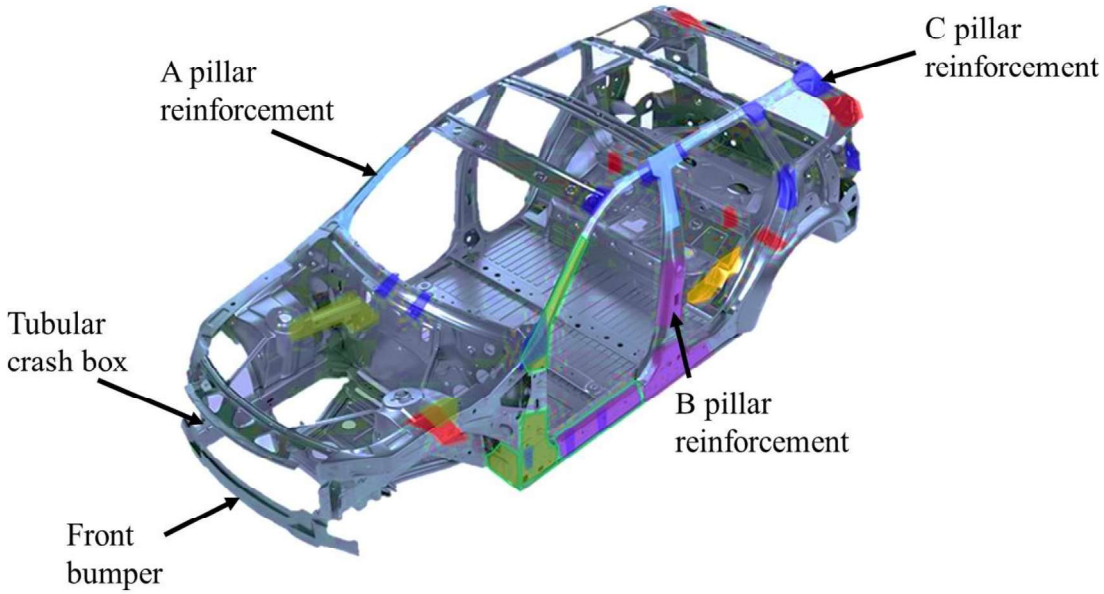

Fig. 2.8. Key energy absorbing components in automotive structural design [76]

2.8. Enhancement of Basalt Fiber Reinforced Polymer Composite

Based on the literature survey, it has been shown that epoxy resin is the most widely used matrix material in fabricating BFRP composites. The increasing attention on BF/Epoxy composites is due to the combination of high strength, durability, and thermal stability of the resulting composite, making them a promising alternative for structural applications. However, the compatibility issues between BF and any polymer resin have been a major challenge in achieving the desired performance. These challenges primarily stem from the relatively weak interfacial bonding between the hydrophilic BF and the hydrophobic polymer resin, which can negatively affect load transfer efficiency and overall mechanical performance. To address these challenges, researchers have explored various enhancement strategies aimed at improving interfacial adhesion, mechanical performance, and overall composite durability. Among these

strategies, surface modifications such as plasma treatment, acid etching, and nanoparticle deposition, as shown in Fig. 2.9, have been employed to enhance the fiber-matrix interface, leading to improved stress transfer and better composite integrity. Additionally, epoxy toughening modifications have been investigated to enhance the fracture toughness and impact resistance of the developed composites. These modifications include the incorporation of nano-reinforcements such as carbon nanotubes, graphene oxide, and silica nanoparticles, as well as the addition of thermoplastic toughening agents to improve the flexibility and toughness of the epoxy matrix.

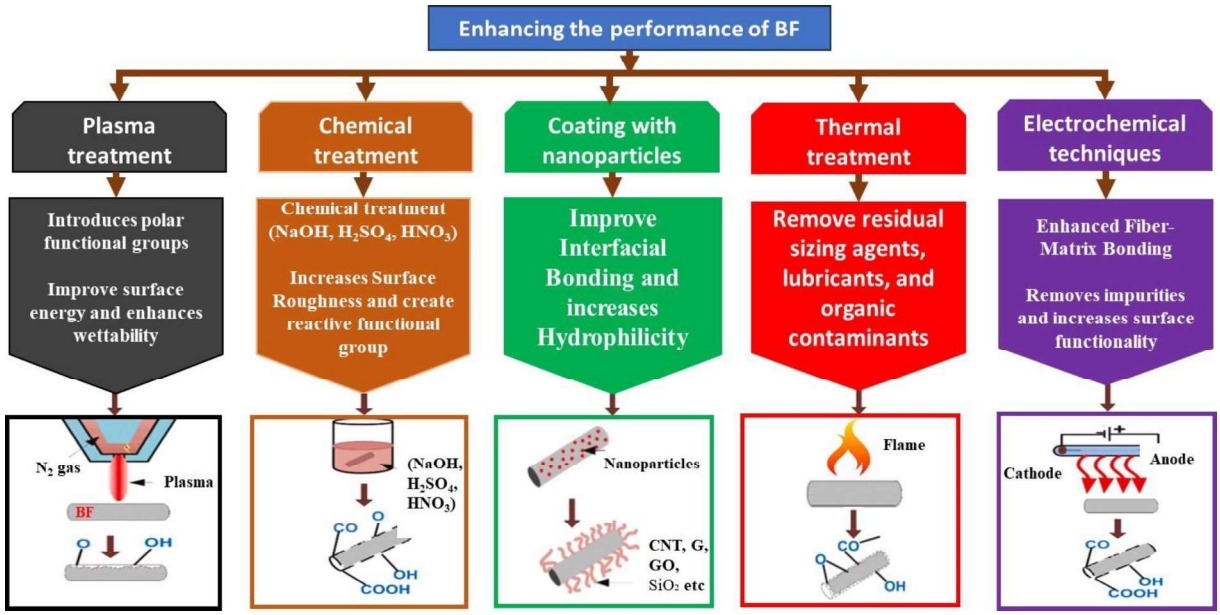

Fig. 2.9. Different methods of improving the interfacial bonding strength of BF [77]

By addressing the interfacial bonding challenges between BF and matrix resins, researchers have reported improvement in the mechanical strength, durability, and overall performance of BFRP composites. The continuous research on performance enhancement techniques, including chemical treatments, nanofiller incorporation, and hybrid reinforcement strategies, has shown great promise in improving the properties and longevity of BFRP

composites for lightweight structural applications. Such advancements are especially beneficial in high-performance industries where materials are subjected to extreme mechanical loads, thermal stresses, and harsh environmental conditions.

2.8.1. Chemical Treatment

Acidic and alkaline treatments are among the most commonly employed surface modification techniques used to enhance the functionality of BF for improved adhesion with polymer resins in composite fabrication. These treatments effectively modify the fiber surface by removing impurities, altering surface roughness, and introducing functional groups that promote better interfacial bonding with the matrix. Acidic treatments, such as sulfuric acid (H_2SO_4) and hydrochloric acid (HCl), help in etching the fiber surface, increasing surface energy, and enhancing wettability [62,78]. On the other hand, alkaline treatments, typically using sodium hydroxide (NaOH), aid in eliminating surface impurities, increasing fiber roughness, and improving fiber-matrix interaction. Lee et al [62] employed potassium hydroxide (KOH) and sulfuric acid (H_2SO_4) treatments to modify the surface properties of BFs and strengthen their interfacial bonding with the epoxy matrix. The findings revealed the formation of a micro-etched layer on the fiber surface after the sequential treatment with both solutions. This led to improved mechanical interlocking between the BF and epoxy resin and enhanced ILSS performance.

2.8.2. Hybridization with Other Fibers

Hybridization techniques are extensively utilized to improve the performance of BFRPs by integrating BF with other reinforcement materials, such as CF or GF. This method results in hybrid composites that leverage the distinct advantages of each fiber type, enabling the customization of mechanical, thermal, and durability properties to suit specific application needs. By strategically combining two or more different fibers to form hybrid composites, a balanced

performance profile can be achieved, overcoming the individual limitations of each fiber type while optimizing key attributes such as stiffness, impact resistance, and interfacial bonding strength. The integration of CF into BF-reinforced polymer, for example, enhances tensile strength, interlaminar shear strength, and stiffness due to improved interfacial bonding, while the addition of GF can improve cost-effectiveness and impact resistance.

Alshgari et al. [79] examined the mechanical properties of BF/CF hybrid polymer composites by varying the mass fractions of both fibers in an epoxy matrix (see Table 2.2). Their findings revealed that increasing the carbon fiber content significantly improved the tensile and flexural strengths of the hybrid composite. However, a higher carbon fiber ratio resulted in reduced impact energy. The optimal hardness was achieved when basalt and carbon fibers were present in equal proportions, as shown in Fig. 2.10. Sun et al. [80] investigated the mechanical properties of BF/CF/epoxy hybrid composites through experimental, analytical, and numerical approaches. Their findings demonstrated that the incorporation of carbon fibers (CFs) and variations in stacking sequences had a significant effect on flexural strength and modulus, while their influence on tensile modulus was relatively minimal.

Table 2.2. The weight ratio of the BF/CF hybrid composite [79]

Sample code	Weight of carbon fiber mat (g)	Weight of basalt fiber mat (g)	Weight of epoxy matrix (g)	Weight of composite laminate (g)
A	75	15	130	220
B	60	30	130	220
C	45	45	130	220
D	30	60	130	220
E	15	75	130	220

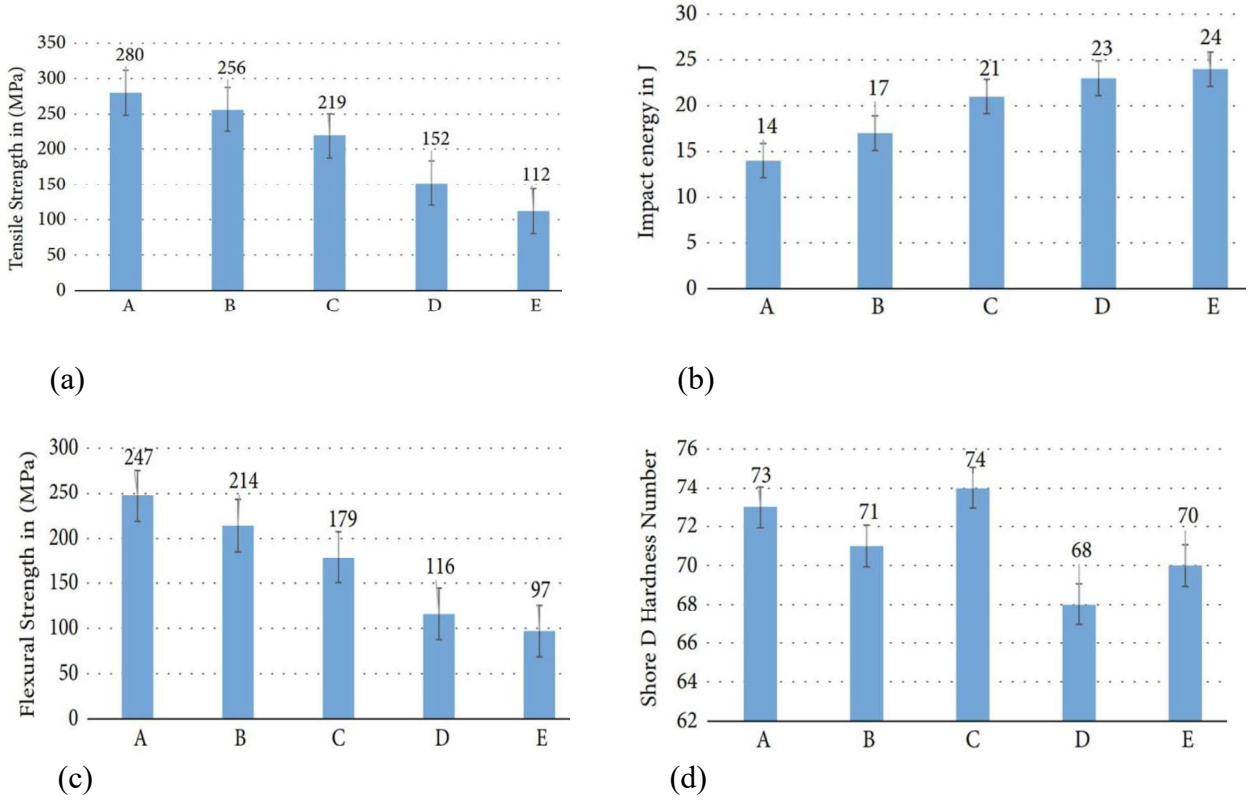

Fig. 2.10. Mechanical performances of carbon/basalt fiber hybrid composite: (a) Tensile strength, (b) Impact energy, (c) Flexural strength, (d) Hardness number [79]

Natarajan et al. [81] studied the impact of hybridization on the mechanical and thermal properties of BF/E-glass polymer composites produced using vacuum-assisted resin transfer molding. Their results showed that higher E-glass fiber content significantly enhanced the tensile and flexural properties of the hybrid composite, albeit with a slight decrease in impact resistance. Thermogravimetric analysis revealed that the hybrid composite containing 35% basalt and 34% E-glass had the lowest decomposition temperature at 381.10 °C, demonstrating its suitability for high structural-load applications. In general, hybridization allows for tailored material properties by adjusting fiber ratios, orientations, and stacking sequences to meet specific engineering requirements. This adaptability makes hybrid fiber-reinforced composites suitable for a wide range of applications, including aerospace, automotive, marine, and construction industries, where customized material properties are crucial for efficiency, safety, and sustainability.

2.8.3. Modification with Nanoparticle

One of the most effective approaches for addressing the compatibility issues between BF and polymer matrices is the incorporation of nanoparticles. This strategy has been widely recognized for its ability to enhance mechanical properties, improve aging resistance, and strengthen interfacial bonding between the fiber and polymers [64,82–84]. The integration of nanoparticles can be achieved through two primary methods: direct dispersion into the polymer matrix or surface modification of the fibers. In the first approach, nanoparticles such as silica, carbon nanotubes (CNTs), graphene oxide, and nanoclay are uniformly dispersed within the resin, leading to improved matrix toughness and enhanced load transfer from the matrix to the fiber. The second method involves coating or grafting nanoparticles onto the BF surface, creating a rougher texture that promotes mechanical interlocking and better adhesion with the polymer matrix. This surface functionalization enhances fiber-matrix interactions, reducing delamination and improving stress distribution. This grafting approach has shown significant improvement in the performance of BF-reinforced polymer composites, making them more suitable for high-end applications in aerospace, automotive, and construction industries. Few researchers have explored and reported the effectiveness of these techniques, as highlighted in the following Sections.

2.8.3.1. Direct Dispersion in Matrix Resin

Bulut et al. [85] investigated the effect of incorporating nanoclay particles into BFRP composites to improve their mechanical performance. The results indicated that nanoclay particles enhanced edgewise impact resistance by 16.8% at 0.5 wt%. Ary Subagia et al. [86] demonstrated that the addition of tourmaline particles to BFRP composites increases the surface area for strong interfacial interaction at the BF/epoxy interface, enhances load transfer, and

improves mechanical performance. He et al. [87] reported that adding silica nanoparticles to basalt fiber/polylactic acid (BF/PLA) composites enhanced tensile strength and interlaminar fracture toughness due to improved interfacial bonding provided by the nanoparticles.

2.8.3.2. Attaching the Nanoparticle to the BF Surface

In an effort to enhance the weak interfacial bonding between BFs and polyamide 6 (PA6), Wang et al. [66] applied carboxylated carbon nanotubes (CNTs) onto the BF surface using an environmentally friendly fiber sizing method. The CNTs were uniformly dispersed, improving surface roughness and wettability, which led to enhanced mechanical properties of the composites. With 1.5 g/L CNT sizing, the tensile and flexural strengths increased by 17.5% and 36.0%, respectively, while wear resistance improved by 40.5%. Zhang et al. [88] chemically grafted 1,6-hexanediol diglycidyl ether (HDE) onto continuous BF using KH550 as a coupling agent to improve interfacial adhesion with epoxy resin. This modification enhanced infiltration, reduced interface defects, and improved load transfer, significantly increasing tensile strength. The optimal surface coverage was achieved at CBFs-g-2%-KH550-g-HDE, as confirmed by SEM analysis. The modified composite exhibited a 56% strength increase compared to unmodified CBF/EP composites. However, uneven surface coverage led to defects, reducing reinforcement efficiency. Similarly, Xiang et al. [67] enhanced the interfacial bonding of BF/epoxy composites by grafting carboxylated multi-walled carbon nanotubes (CNTs) onto BF using a silane coupling agent (KH560). The study found that at an optimal 5% mass fraction of KH560, the ILSS of the modified composite (BF-5%KH560-CNT/EP) increased by 25.5% compared to the unmodified composite. Mittal and Rhee [89] showed that coating BF with graphene improves interfacial bonding and the mechanical performance of the composite. Rong et al. [65] reported that surface electrostatic assembly of graphene oxide (GO) in basalt fiber-

reinforced polyamide 6 (PA6) composites significantly enhanced the ILSS by 85.1% and impact strength by 43.2%. This method shows promise for improving the surface characteristics of BFs and expanding their industrial applications. Tian et al. [90] utilized electrospun polyacrylonitrile (PAN) nanofibers to improve the interfacial properties of BFRP composites and reported that the modification increased the interfacial shear strength of the composites by 31.33%.

2.9. Nanocellulose

Nanocellulose is a renewable and versatile material derived from plants, which is the most abundant biopolymer on Earth. It is often extracted from plant fibers, bacteria, or algae and processed to produce nanoscale cellulose structures. NC exhibits unique mechanical, thermal, and optical properties, making it a promising material for various applications, including in composite materials, electronics, medical devices, and packaging. It has been increasingly explored for reinforcing polymers due to its remarkable strength-to-weight ratio, biodegradability, renewability, and high surface energy. NC's eco-friendly nature and ability to improve the mechanical properties of composites make it an attractive alternative to synthetic nanoparticles.

2.9.1. Types of Nanocellulose

Nanocellulose was first identified in 1838 by French chemists Anselme Payen and Jean-François Persoz, who successfully isolated cellulose from plant materials and recognized it as a complex carbohydrate. Payen later presented their findings to the French Academy of Sciences, officially establishing cellulose as a fundamental structural component of plant cell walls. Cellulose is a polymer composed of repeating units of β-D glucose linked by β-1,4-glycosidic bonds, as shown in Fig. 2.11. It is an insoluble polysaccharide that provides strength and rigidity to plant cell walls. Cellulose derived from lignocellulosic biomass primarily exists in two nanostructured forms depending on the synthesis method: Cellulose Nanofibers (CNF) and

Cellulose Nanocrystals (CNC). These two forms differ in their structure, properties, and potential applications, making them suitable for various industries, including composites, biomedical engineering, packaging, and coatings.

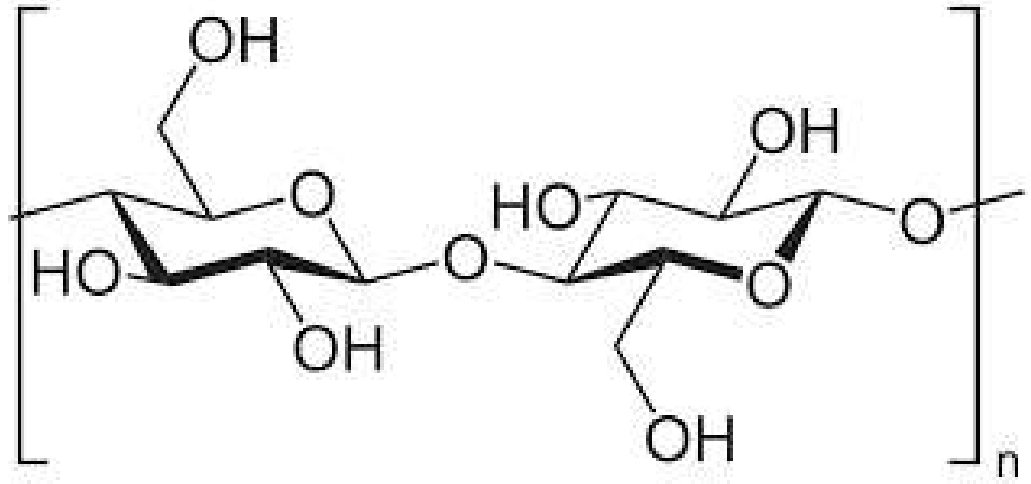

Fig. 2.11. Structure of cellulose [91]

2.9.1.1. Cellulose Nanofiber (CNF)

Cellulose Nanofibers (CNF) are long, flexible fibers that are extracted through mechanical processes, such as grinding or homogenization, usually involving a chemical pretreatment process such as TEMPO oxidation. It is sometimes referred to as nano-fibrillated cellulose. CNF typically has a diameter in the range of a few nanometers and lengths up to several micrometers. They exhibit high surface area, mechanical strength, and flexibility, making them suitable for various applications, including composites, films, and coatings. Due to their ability to form strong hydrogen bonds, CNFs are especially valuable as reinforcing agents in composite materials. Their high-water retention capacity and their ability to form transparent films also open up possibilities in the packaging and electronics industries.

2.9.1.2. Cellulose Nanocrystals (CNC)

Cellulose Nanocrystals (CNC) are crystalline, rod-like nanoparticles with high mechanical strength and stiffness. They are obtained by hydrolyzing cellulose fibers using strong chemicals, such as sulfuric and hydrochloric acid, or sodium hydroxide, which breaks down the amorphous regions of cellulose, leaving behind the crystalline regions. CNCs typically have a size range of 2–20 nm in diameter and a length of 100–500 nm. Due to their rigid structure, CNCs exhibit excellent strength, high thermal stability, and exceptional reinforcing properties. They are used in applications such as nanocomposites, films, hydrogels, and biomedical devices. CNCs also have unique optical properties, such as birefringence and the ability to form chiral nematic liquid crystals, which are useful in sensing and display applications. The schematic representation and properties of both CNC and CNF are shown in Fig. 2.12 and Table 2.3, respectively.

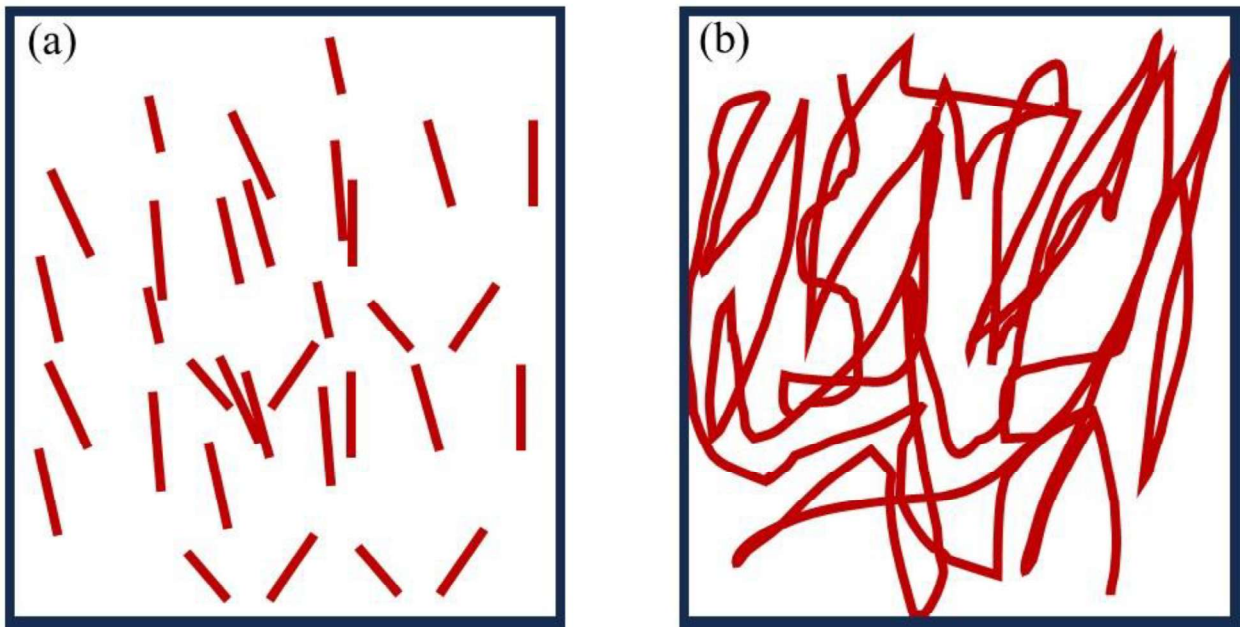

Fig. 2.12. Morphology of Nanocelluloses: (a) CNC and (b) CNF

Table 2.3. Physicochemical properties of nanocellulose [92]

Product specification	Cellulose nanofiber (CNF)	Cellulose nanocrystal (CNC)
Appearance	White odorless powder	White odorless powder
Surface property	hydrophilic	Hydrophilic
Moisture content	3-7%	4-6%
Granular size	1-50 μm	1-50 μm
crystallinity	50 ± 5%	88%
pH	6-8	6-7
Average aspect ratio	300	22
Zeta potential	-56.1 mV	-37.0 mV

2.9.2. Advantages of Nanocellulose

Nanocellulose offers several advantages, especially when compared to traditional synthetic materials. One of its key benefits is high mechanical strength; nanocellulose exhibits exceptional tensile strength, making it an excellent reinforcement material in composites. Its high surface area and stiffness enhance the mechanical properties of composites, improving their strength without significantly increasing the weight, a critical factor in industries such as aerospace and automotive. In addition to its mechanical properties, nanocellulose is also a renewable material derived from abundant agricultural wastes such as wood and plants. This makes it an attractive alternative to fossil-based materials, contributing to the development of more sustainable materials and supporting the transition to circular economies. Unlike synthetic nanoparticles, NC is a biodegradable and renewable material, offering an eco-friendly solution for applications where disposal or long-term environmental impact is a great concern. Nanocellulose offers several intrinsic advantages for surface and interfacial modification of FRP composites. Its high density of hydroxyl functional groups promotes strong physicochemical interactions, including hydrogen bonding, enhancing interfacial adhesion and load transfer. In addition, NC exhibits a

stiffness that is closely matched to that of BF, reducing interfacial stiffness mismatch and minimizing stress concentrations at the fiber–matrix interface. Its lightweight nature further contributes to improved specific mechanical performance without compromising structural efficiency. Additionally, the high surface area of NC allows for easy functionalization, enabling the attachment of functional groups to tailor its properties for specific applications. This functionalization enhances its ability to interact with other materials, such as polymers, improving the overall performance of composite materials.

2.9.3. NC-modified FRP and its Challenges

In recent times, there has been a rapid growth in the utilization of multi-scale reinforcement in composite development by incorporating nanomaterials to modify fiber surfaces. This trend opens up opportunities for creating novel hierarchical composite materials with improved mechanical performance, suitable for diverse applications such as automotive, electronics, aerospace, and construction. The nano-scale dimensions of these integrated nanomaterials within polymer microstructures play a crucial role in significantly enhancing surface interactions between fibers and the polymer matrix, thereby leading to improved mechanical properties. Based on the literature study, carbon-based nanomaterials emerge as the most commonly employed multi-scale nanomaterials for enhancing the surface characteristics of fibers and improving the mechanical performance of the resulting composites. Nevertheless, the associated drawbacks, such as high cost, toxicity, and non-renewability issues, have spurred researchers to explore alternatives that are more sustainable, easy to process, and environmentally friendly. The potential of NC in enhancing the performance of CFRPs [28–30,93] and GFRPCs [4,5,94,95] has been well-documented. By dispersing the NCs into the polymer matrix, the researchers aimed to enhance the composite's interfacial bonding between

the fiber and resin through matrix toughening effects. The strong hydrogen bonding and nanostructure of NCs contribute to improving load transfer efficiency, reducing microcrack propagation, and enhancing energy absorption during mechanical loading. However, challenges such as agglomeration of NCs, nonuniform dispersion within the resin, and an increase in resin viscosity have significantly restricted this approach.

2.10. Development of Hat-Shaped BFRP Composite

The design of hat-shaped components in composite structures is widely recognized for their high energy absorption and structural efficiency, making them ideal for crashworthy applications. FRPs, especially CFRPs, are widely studied and applied in transportation sectors such as aerospace, marine, and automotive, due to their high strength-to-weight ratio, corrosion resistance, and contribution to fuel efficiency [9,96]. In addition, the deformation behavior and energy absorption characteristics of CFRPs under various loading conditions and geometries have been extensively studied, providing valuable insights into their structural performance under stress and their suitability for high-performance applications in the automotive industry [97–100]. However, limited literature exists specifically on BFRP hat-shaped components. This gap is especially evident when considering bio-based enhancements such as NC modification, highlighting a research area this study aims to address.

2.10.1. Fabrication and Experimental Procedure

In drop-weight impact testing, span length plays a critical role in controlling the deformation modes and failure mechanisms of composite structures, especially in determining whether failure is dominated by shear or bending. To accurately assess how NC modification affects mechanical response, particularly improvements in shear resistance or bending behavior, it is essential to test the composite under varying span lengths. Hence, the hat-shaped BFRPs

were fabricated and evaluated at three different span lengths: 80 mm, 140 mm, and 200 mm. Key impact parameters such as strain rate sensitivity, contact force history, peak load, and time to failure are all influenced by span length. These parameters not only provide fundamental insight into the structural behavior of the modified composite under realistic loading conditions but also serve as crucial inputs for validating finite element simulations. By varying span length, a more comprehensive evaluation of the real-world performance and energy absorption capabilities of the NC-modified BFRP composite can be achieved.

2.10.2. Modeling and Simulation

Finite element analysis (FEA) has become an essential tool in evaluating the structural behavior of composite materials under dynamic, static, or quasi-static loading conditions. Several studies have focused on modeling FRPs to assess their mechanical performance under various loading conditions [97–100]. Abaqus, a widely used FEA software, has been extensively employed for this modeling, particularly in crashworthiness applications and general impact conditions [101,102]. The simulation of impact and crash scenarios allows researchers to predict failure mechanisms, optimize material performance, and enhance structural design efficiency [103]. Chen et al. [103] utilized Abaqus to model the damage behavior of FRP structures and evaluate their suitability for high-impact applications. The study examined the energy absorption behavior of CFRP and GFRP hat-shaped composite tubes under quasi-static and dynamic axial crushing loads. Experimental and numerical results indicated that CFRP exhibited a 23.3% reduction in energy absorption at higher loading rates, whereas GFRP maintained a stable response. The FEA accurately predicted the crushing behavior, providing valuable insights for the crashworthiness design of composite structures. Similarly, Rozylo et al. [104] investigated the structural behavior and failure mechanisms of top-hat-shaped CFRP composite columns

under eccentric compressive loading. The study examined the buckling, post-buckling, and load-carrying capacity of the structure through experimental testing and FEA in Abaqus. Nonlinear numerical simulations, incorporating Hashin's failure theory and progressive failure analysis, closely matched the experimental results.

To validate the experimental findings and optimize the geometry before fabrication, FEA was performed using Abaqus. This helped assess preliminary structural behavior and refine key design parameters. Geometric factors such as flange width, corner radius, wall thickness, and specimen length were found to significantly influence deformation responses and failure mechanisms. Optimizing these parameters enabled a focused evaluation of the enhanced interlaminar strength and energy absorption introduced by NC modification, offering valuable insights into the crashworthiness and structural reliability of the composite for practical applications.

The numerical validation plays a critical role in ensuring the accuracy and reliability of experimental results by providing a computational framework to predict structural behavior under various loading conditions. By comparing numerical simulations with experimental data, discrepancies can be identified, helping refine both the experimental setup and modeling assumptions. This process enhances confidence in the experimental findings while allowing for the optimization of material properties, boundary conditions, and failure mechanisms. Furthermore, numerical simulation reduces the need for extensive physical testing, saving time and resources while ensuring that the experimental results are both consistent and reproducible. In a study conducted by Koricho et al. [105], the behavior of a woven fabric carbon/epoxy composite T-joint was investigated using experimental and numerical methods to analyze its load-carrying capacity and failure mode. Numerical simulations accurately predicted stress

distribution and stiffness, with an error of less than 3% compared to experimental results. According to Hashin's failure criteria, the first ply failure occurred at 3.746 kN in simulations, while experimental tests showed failure at 3.4 kN, corresponding to the first load drop, highlighting a strong correlation between simulated and observed deformation patterns. This underscores the reliability of numerical simulation in predicting energy absorption and failure mechanisms of composite structures.

Similarly, Lombarkia et al. [106] investigate the failure mechanisms of plain weave CFRP hat-shaped cross-section specimens under quasi-static crushing loads. Their study reported that numerical simulations using stacked-shell models in Abaqus/explicit accurately predicted the crushing behavior, failure modes, and energy absorption characteristics. The simulation results showed strong agreement with experimental data, validating the effectiveness of finite element modeling in replicating real-world structural responses.

The application of the Abaqus solver for simulation in the present study aligns with previous research on modeling and simulating hat-shaped FRP components, including CFRP and GFRP under impact loading. These studies have demonstrated the effectiveness of numerical simulations in predicting crushing behavior and failure mechanisms in FRP composites. However, despite the progress in understanding the energy absorption behavior of CFRP and GFRP, there remains a notable gap in the literature regarding the energy absorption capabilities and failure mechanisms of BFRPs, particularly in crashworthiness and impact-resistant applications. This gap highlights the need for further investigations into BFRP-based composite structures through experimental and numerical analyses to assess their feasibility as viable alternatives for high-performance energy-absorbing applications. Given their superior mechanical properties, environmental advantage, and cost-effectiveness, BFRPs have the

potential to serve as viable alternatives to traditional composite materials in automotive and other lightweight structural applications. This study builds upon existing literature by employing Hashin's failure criteria in Abaqus explicit dynamic analysis to evaluate the crashworthiness and structural performance of CNC-modified and unmodified BFRPs and compare the results with experimental findings.

2.10.3. Damage Criteria

Composite materials exhibit complex failure mechanisms due to their heterogeneous and anisotropic nature. Unlike metals, which often fail through well-defined yielding, composites may undergo multiple interacting damage processes such as fiber breakage, matrix cracking, fiber–matrix debonding, and delamination. To predict and model these failures, several damage and failure criteria have been developed over the years. These criteria provide mathematical frameworks that relate applied stresses or strains to the onset of damage, enabling engineers and researchers to evaluate the structural integrity of composite components under different loading conditions. Given the diversity of failure mechanisms in composites, no single model can universally capture all aspects of damage progression. Therefore, it is essential to review the most widely adopted criteria to understand their theoretical basis, predictive capabilities, and limitations. The following sections discuss the commonly used approaches, including Maximum Stress/Strain, Tsai–Hill, Tsai–Wu, and Hashin criteria. Among these, the Hashin criterion is adopted in the present study because it not only accounts for the anisotropic nature of composites but also distinguishes between fiber- and matrix-dominated failure modes under different loading conditions. This mode-dependent formulation provides more realistic predictions of damage initiation and progression, making it particularly suitable for evaluating the impact behavior of BFRP composites where both shear- and tension-driven failures may occur.

2.10.3.1. Maximum Stress/Strain Criterion

These criteria represent lamina failure when any single stress (or strain) component exceeds its allowable; they require only uniaxial strengths (or failure strains) in the fiber and transverse directions, plus in-plane shear. Their appeal is simplicity and speed, making them staples of preliminary sizing. However, by ignoring stress interactions and failure mechanisms, they can be non-conservative under multiaxial loads and provide no guidance on post-initiation degradation—hence they are rarely used alone for progressive damage.

2.10.3.2. Tsai–Hill Criterion

This criterion extends the von Mises yield condition, originally formulated for isotropic materials, to describe the anisotropic behavior of composites. It is a quadratic interaction criterion derived from Hill's anisotropic yield theory, which provides a single smooth failure surface that captures combined stress effects better than maximum stress/strain. It is popular in laminate optimization and as a fast FE check. Its main drawback is the lack of tension/compression asymmetry and failure-mode resolution (fiber vs. matrix), so it typically serves as an initiation check rather than a complete damage model. The Tsai-Hill criterion predicts failure when the failure index in a laminate reaches one (1).

2.10.3.3. Tsai–Wu Criterion

This is an extension of Tsai–Hill's criteria by adding linear and quadratic terms that account for tensile–compressive asymmetry and broader interactions. It fits well within FE workflows and offers a smooth envelope conducive to sensitivity studies. The practical challenge is identifying the interaction coefficients (commonly); without biaxial data, assumptions may compromise accuracy. Like Tsai–Hill, it signals initiation but must be paired with a degradation law for progressive damage.

2.10.3.4. Hashin's Criterion

In the modeling of FRPs, key considerations include material modeling, element selection, failure criteria, and contact conditions. Researchers have employed different damage models to simulate composite failure accurately. Hashin's criterion is widely adopted to model intralaminar damage, as it effectively distinguishes between fiber–and matrix–dominated failure modes within individual plies as shown in equations 2.1-2.4. However, Hashin's model does not capture interlaminar failures, such as delamination, which play a critical role in the structural response of laminated composites under dynamic and impact loading. To address this limitation, cohesive zone modeling (CZM) was incorporated alongside Hashin's criterion. CZM enables the explicit simulation of delamination initiation and propagation at ply interfaces by defining a traction–separation relationship. This approach has proven effective in analyzing the progressive failure of FRP structures under impact loading.

Tensile fiber failure ($\sigma_f^T \geq 0$) (2.1)

$$F_f^t = \left(\frac{\sigma_{11}}{X^T}\right)^2 + \alpha \left(\frac{\tau_{12}}{S^L}\right)^2$$

Occurs when fibers fail due to excessive tension along the fiber direction.

Compressive fiber failure ($\sigma_f^C < 0$) (2.2)

$$F_f^c = \left(\frac{\sigma_{11}}{X^C}\right)^2$$

Occurs when fibers fail due to compression along the fiber direction.

Matrix tension ($\sigma_m^T \geq 0$) (2.3)

$$F_m^t = \left(\frac{\sigma_{22}}{Y^T}\right)^2 + \left(\frac{\tau_{12}}{S^L}\right)^2$$

Occurs when the matrix cracks under transverse tension

Matrix compression ($\sigma_m^C \geq 0$) (2.4)

$$F_m^c = \left(\frac{\sigma_{22}}{2S^T}\right)^2 + \left[\left(\frac{Y^C}{2S^T}\right)^2 - 1\right]\left(\frac{\sigma_{22}}{Y^C}\right)^2 + \left(\frac{\tau_{12}}{S^L}\right)^2$$

Occurs due to matrix crushing under transverse compression.

where X^T and X^C, Y^T and Y^C, S^L and S^T denote the longitudinal tensile and compressive strengths, transverse tensile and compressive strengths, longitudinal and transverse shear strengths, respectively. The coefficient (α) in Equation (2.1) governs the influence of shear stress on the fiber tensile failure initiation criterion.

2.11. Delamination Behavior With CZM

Cohesive zone modeling is a robust and widely adopted computational framework used to investigate interfacial delamination phenomena in FRP composites [107,108]. Delamination, the separation of layers within laminated composites, is one of the most common and critical failure modes in FRPs, particularly under impact, fatigue, or out-of-plane loading conditions. It provides an accurate approach to simulating delamination by explicitly representing the fracture process zone at the interfaces between composite laminates using predefined cohesive elements. In the context of FRP composites, cohesive elements are strategically inserted along potential delamination paths, typically between plies, where interfacial failure is likely to occur. These cohesive elements mimic the behavior of the resin-rich regions that bond the laminate layers together and are governed by a constitutive law that models delamination [109]. Various

traction–separation laws have been developed and are typically categorized based on their shape, such as bilinear, exponential, or trapezoidal. Among these, the bilinear model is the most widely used due to its simplicity and ease of implementation. In this study, a bilinear traction–separation law was adopted, as illustrated in Fig. 2.13, and defined by parameters such as the normal and shear interfacial strengths, penalty stiffness, and critical energy release rates in Modes I and II. These parameters were calibrated based on experimental data to ensure an accurate representation of the delamination behavior. While the critical energy release rates (Modes I or II fracture toughness) may be experimentally determined through standard fracture tests, the interfacial strength in the normal and shear directions, as well as the penalty stiffness, are difficult to obtain experimentally. Therefore, these parameters are commonly adopted in numerical simulations [110], although in some cases the interfacial strengths are assumed to be equal to the in-plane intralaminar strengths of the composite [111,112]. Turon et al. [113] proposed an empirical equation to estimate the penalty stiffness K, as shown in Eq. (2.5).

$$K = \frac{\alpha E_3}{t} \tag{2.5}$$

where t is the thickness of the adjacent sub-laminate and α is a dimensionless scaling parameter significantly greater than 1. The through-thickness modulus, E_3 (perpendicular to the lamina), was approximated as the epoxy matrix modulus since the bonding between two adjacent layers depends only on matrix properties. In their study, Turon et al. proposed that α should be greater than 50 for accurate simulation of various problems. However, this value must be selected appropriately for each specific material. Choosing a value that is too low may introduce excessive compliance into the CEs, while excessively high values can lead to numerical instability, convergence issues, and increased computational cost.

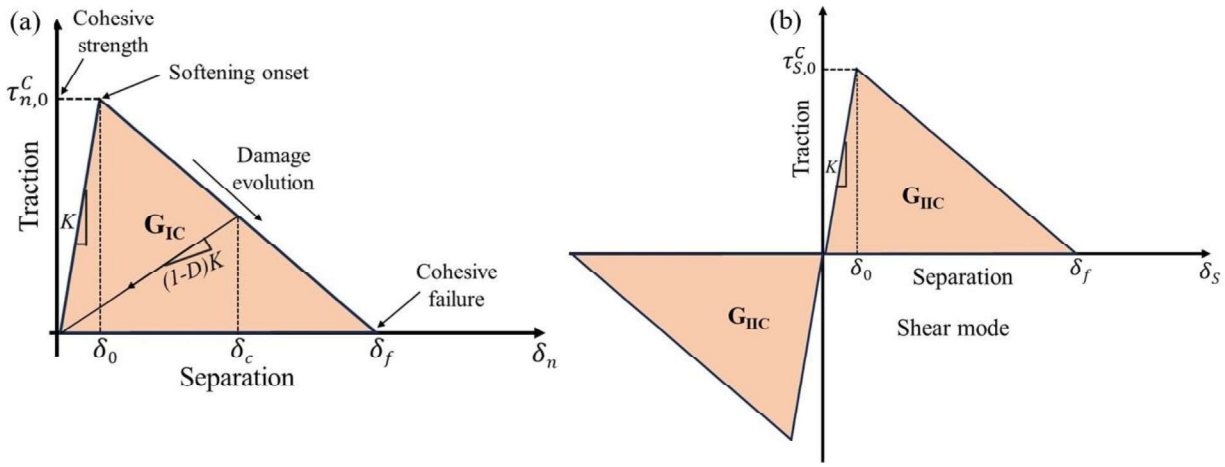

Fig. 2.13. Bilinear traction-separation law for cohesive modeling: (a) Opening mode and (b) Sharing mode

The traction–separation law typically exhibits an initial linear elastic region, where the interface resists separation with increasing stiffness (K). Once the applied stresses exceed a defined damage initiation criterion (such as maximum stress or quadratic nominal stress), the cohesive elements begin to degrade in stiffness, entering a softening regime that represents progressive damage. Full decohesion and delamination occur when the fracture energy, which represents the area under the traction–separation curve, is fully dissipated. This fracture energy is mode-dependent and includes Mode I (G_{IC}), Mode II (G_{IIC}), or combinations thereof in mixed-mode loading. CZM allows for a detailed and realistic simulation of delamination growth by accounting for the nonlinear and irreversible nature of interfacial failure. It is particularly useful in evaluating the influence of material modifications, such as the surface grafting of NC onto BF, on delamination resistance. Enhancements in interfacial adhesion, as observed in NC-grafted BFRPs, can be directly captured in CZM simulations by defining the cohesive properties such as fracture energy, interfacial stiffness, and maximum traction values in Abaqus.

The cohesive strengths play a critical role in governing the initiation of interfacial failure (D = 0), as they directly influence the onset and progression of damage at the ply interfaces. When the interfacial traction exceeds the defined strength threshold, a progressive softening process is triggered, characterized by the evolution of damage and ultimately leading to complete delamination (D = 1) as expressed in Eq. (2.6) with reference to Fig. 2.13. The total work required to achieve full delamination corresponds to the fracture toughness (G_{IC} or G_{IIC}) of the interface, which is quantified by the area under the traction–separation curve. An accurate definition of these strengths is essential to reliably capturing both the initiation and propagation phases of delamination in composite structures under dynamic loading conditions.

$$D = \begin{cases} 0, & \delta_c \leq \delta_0 \\ 1, & \delta_c = \delta_f \end{cases} \tag{2.6}$$

D is the damage variable, δ_0 is displacement at damage initiation, $\delta_c$is the critical separation and $\delta_f$is the separation at complete cohesive delamination failure.

Delamination onset is often predicted using a quadratic stress criterion, which accounts for the combined effects of normal and shear stresses acting at the ply interface [114]. This approach assumes that damage initiates when a normalized combination of the stress components reaches a critical value, capturing the interaction between different failure modes. The criterion is commonly expressed as shown in Eq. (2.7).

$$\left(\frac{\tau_n}{\tau_n^c}\right)^2 + \left(\frac{\tau_s}{\tau_s^c}\right)^2 + \left(\frac{\tau_t}{\tau_t^c}\right)^2 = 1 \tag{2.7}$$

Where τ_n is the effective normal stress, τ_s and $\tau_t$are the shear stresses in the two tangential directions. τ_n^c, τ_s^c, and τ_t^c are the corresponding cohesive strengths in the normal and shear directions.

The progression of interfacial damage was modeled using the Benzeggagh–Kenane (B–K) fracture criterion, which describes energy dissipation based on the mixed-mode loading ratio. According to this approach, once the damage initiation condition is met, the cohesive traction reduces progressively to zero, depending on the amount of energy released during crack growth. The B–K model is particularly well-suited for simulating delamination in composites under mixed-mode loading, as it allows the critical energy release rate to vary according to the relative contributions of Mode I and Mode II, as defined in Eq. (2.8).

$$G_C = G_{IC} + (G_{IIC} - G_{IC}) \left(\frac{G_{II}}{G_I + G_{II}}\right)^{\eta} \quad (2.8)$$

G_{IIC}, G_{IC} are the critical energy release rates in pure Mode II and Mode I, respectively, η is an empirical parameter, also known as the B-K law constant that controls the curvature of the mixed-mode fracture envelope, and G_C is the mixed-mode fracture toughness.

2.12. Critical Research Gaps and Scientific Positioning of the Developed BFRP

Despite growing interest in basalt fiber-based composites as environmentally compatible alternatives to conventional glass- and carbon-fiber-reinforced systems, the development of a stable and durable fiber–matrix interface remains a critical unresolved challenge. BFs exhibit relatively smooth and chemically inert surfaces, which limit effective interfacial adhesion with polymer matrices. Consequently, many BFRP systems continue to suffer from inefficient load transfer, premature interfacial delamination, reduced impact resistance, and performance degradation under service-relevant loading conditions. Although incremental improvements have been reported, an environmentally compatible interfacial modification strategy capable of simultaneously enhancing mechanical performance, durability, and structural reliability has yet to be fully established. To address these limitations, previous studies have extensively explored

the incorporation of conventional nanoparticles such as carbon nanotubes, graphene-based fillers, and silica nanoparticles, either within the polymer matrix or at the fiber–matrix interface. However, these approaches have not consistently addressed the fundamental interfacial limitations of BFRP systems. High surface energy and strong van der Waals interactions frequently lead to nanoparticle agglomeration, resulting in non-uniform dispersion and localized stress concentrations. In addition, many inorganic and carbon-based nanoparticles exhibit limited chemical affinity with BFs and polymer matrices, relying primarily on physical adsorption rather than strong interfacial bonding. Their high stiffness may also induce interfacial mismatch, thereby compromising toughness and damage tolerance. Furthermore, issues related to processing complexity, increased resin viscosity, cost, and potential health concerns significantly restrict their industrial scalability.

In contrast, NC incorporation represents a fundamentally different and underexplored strategy for interface engineering in BFRP composites. Unlike rigid zero-dimensional nanoparticles, NCs, particularly cellulose nanofibers, possess a high-aspect-ratio fibrillar morphology capable of forming interconnected reinforcing networks at the fiber–matrix interface. Moreover, the abundance of hydroxyl functional groups on NC surfaces enables strong physicochemical interactions and facilitates the formation of a stable interphase, which is critical for improving interfacial strength, delamination resistance, and long-term durability. Importantly, NC is renewable and biodegradable, thereby aligning with the sustainability and lightweighting requirements of modern automotive structures. As shown in Table 2.4, the present study adopts an integrated experimental and numerical framework to systematically address the major limitations reported in the literature, thereby establishing its scientific contribution and relevance to structural automotive applications. Specifically, this work defines a clear scientific position by

linking NC type, morphology, and incorporation strategy to interfacial performance, mechanical behavior, durability, and structural suitability for automotive applications. Table 2.5 presents a quantitative comparison of the mechanical performance of the developed BFRP composite with previously reported related systems. The results demonstrate that the NC-grafted BFRP developed in this study achieves a more balanced enhancement in interlaminar shear strength, impact resistance, and fracture toughness, thereby validating the effectiveness of the proposed interface-engineering approach.

Table 2.4. Mapping of identified research gaps to the present study

Identified research gap	**Present study approach**
Limited understanding of the influence of NC morphology on interfacial behavior	Development of a surface grafting strategy for anchoring nanocellulose onto silane-functionalized basalt fiber surfaces to improve fiber–matrix compatibility and enhance interfacial stress transfer.
Limited understanding of the influence of NC morphology on interfacial behavior	Systematic investigation of the effects of CNC and CNF on interfacial bonding characteristics and failure mechanisms of BFRP composites.
Insufficient correlation between interfacial modification and bulk mechanical performance	Comprehensive mechanical characterization of the developed composites, including tensile strength, impact, and interlaminar shear strength evaluations.
Poor understanding of durability under service conditions	Assessment through moisture absorption and durability studies, with emphasis on the retention of mechanical properties after environmental exposure.
Limited structural validation for automotive applications	Validation through experimental structural testing and FE modeling of damage initiation and interfacial failure behavior.

Table 2.5. Quantitative comparison of interfacial modification strategies on the performance of BF-based composites

Composite system	Tensile strength (MPa)	ILSS (MPa)	Impact strength (kJ/m^2)	Ref
BF-PDA/PEI-C-CNTs/epoxy (UD)	370.7 (28.9 %)	60.9 (34.4%)	—	[115]
Al_2O_3/BF/Epoxy (Satins)	146.42 (9%)	—	—	[116]
BF-mono/di-amino silane/PP (Satins)	158 (22.4%)	—	21.4 (21%)	[117]
BF-tourmaline micro/nano/Epoxy (Plain)	357.2 (16%)	—	—	[86]
Silane-treated BF/Epoxy (Plain)	276.8 (11.2%)	33 (10%)	170.4 (10.3%)	[118]
BF/GO/PA6 (Plain)	—	38.9 (85%)	147 (43.2 %)	[65]
BF/CNTs/Epoxy (UD)	318.9 (12.5%)	—	105.3 (25.5%)	[67]
Nanoclay/BF/Epoxy (Plain)	325.5 (7.61%)	—	107.5 (16.9%)	[85]
NC-grafted BF/Epoxy (1.5 wt.% CNC) (Twill)	458 (16%)	50 (79%)	205 (107%)	**This study**

CHAPTER THREE

3. RESEARCH METHODOLOGY

3.1. Introduction

This chapter presents the methodological framework and procedures adopted in conducting the study. It outlines the overall research design and the steps undertaken to achieve the study's objectives. The research was conducted through a series of interrelated projects, each addressing specific aspects of material development, characterization, and structural integration. The methodology was structured to ensure a systematic and comprehensive investigation of the research problem. Each phase of the study built upon the findings of the previous one, allowing for iterative refinement and validation of results. The approach combined both experimental and analytical techniques, integrating qualitative and quantitative data to provide a holistic understanding of the composites' performance and behavior. Furthermore, the chapter briefly describes the equipment as well as the materials used in the study.

3.2. Materials Used

The fabrication of the BFRP composites required a range of materials, including matrix materials, reinforcing fibers, and auxiliary materials to ensure proper lamination and curing. This section presents a summary of the materials employed in the study, whereas detailed information regarding supplier names, material grades, purity levels, and other specifications is provided in Chapter Four.

3.2.1. Reinforcement material

- ✓ Woven BF mats (200 g/m²) served as the primary reinforcement. The BFs were selected for their superior mechanical strength, high temperature resistance, eco-friendliness, and corrosion resistance compared to traditional carbon and glass fibers.

- ✓ Nanocellulose was incorporated as a secondary reinforcement to enhance the interfacial bonding between the BF and the epoxy matrix. The NC particles acted as a reinforcement modifier, improving load transfer efficiency, stiffness, and toughness of the composite.

3.2.2. Matrix material

- ✓ A thermosetting epoxy resin was used as the polymer matrix. The epoxy provided excellent adhesion, chemical resistance, and dimensional stability.
- ✓ A compatible amine-based hardener was mixed with the epoxy resin in a ratio of 1:0.25 by weight as recommended by the manufacturer to initiate the cross-linking reaction during curing.

3.2.3. Auxiliary materials

- ✓ A silane-based coupling agent was used to create reactive sites between the BFs and NCs before resin impregnation. This surface modification enhanced the chemical compatibility between the inorganic basalt fibers and the organic nanocellulose, promoting stronger interfacial adhesion and more efficient stress transfer within the composite structure.
- ✓ A silicone-based release agent was applied to the mold surface to prevent adhesion between the composite laminate and the steel mold, ensuring easy demolding after curing.
- ✓ A nylon peel ply layer was used to achieve a textured surface finish and to facilitate the removal of excess resin during vacuum bagging.
- ✓ A polyester breather fabric was placed above the peel ply to allow uniform air evacuation and resin distribution during vacuum processing.
- ✓ A flexible nylon vacuum bagging film was used to seal the laminate assembly and maintain uniform pressure under vacuum conditions.

- ✓ Butyl-based sealant tape was used to ensure airtight sealing between the vacuum bag and the mold surface.
- ✓ Polished steel molds were used to shape the composite specimens according to the specified geometry and dimensions of all the fabricated composites, including the hat-shaped BFRP component.
- ✓ Additional materials such as hand brushes, rollers, measuring cups, and mixing sticks were used during the hand lay-up process to ensure uniform resin impregnation and fiber wetting.

3.3. Equipment and Methods Used

This section outlines the equipment and experimental methods used for composite fabrication, characterization, and mechanical evaluation, with brief justification for their selection.

3.3.1. Mixing and homogenization

- ✓ High-speed mechanical stirring was used to disperse NCs within the epoxy matrix, followed by vacuum degassing to eliminate entrapped air before composite fabrication. The key processing parameters, including mixing speed, mixing duration, and temperature conditions, are summarized in this section, while the full experimental details are provided in Chapter Four.

3.3.2. Curing equipment

- ✓ A controlled autoclave curing chamber was used to provide uniform temperature and pressure during the curing of BF/epoxy composites. Autoclave curing was selected for its ability to promote complete polymerization, reduce void formation, and efficiently

remove excess resin, thereby ensuring consistent interfacial bonding and optimal mechanical properties compared with ambient or oven curing.

3.3.3. Material characterization

- ✓ XPS was used for the surface chemical characterization of the modified BFs due to its high surface sensitivity and quantitative capability. Alternative techniques such as FTIR and AFM lack the surface-specific chemical sensitivity required for interfacial analysis.
- ✓ SEM was used to examine fiber surfaces, interfacial regions, and fracture morphologies, allowing correlation between microstructural features and mechanical behavior. These techniques were selected over lower-resolution methods to ensure accurate evaluation of interface-specific phenomena.
- ✓ Mechanical properties were evaluated using a UTM following standardized procedures to ensure reliable and reproducible data, while dynamic structural performance was assessed using an impact testing tower to capture loading responses beyond quasi-static conditions.

3.4. Numerical Simulation Approach

Abaqus was employed for the numerical simulation of the optimized BFRP composites due to its superior capability for modeling composite damage and interfacial behavior compared with other commercial FE solvers such as ANSYS. In this study, the BFRP laminate was modelled as an anisotropic material to account for its direction-dependent mechanical properties. The fiber–matrix interface was represented using CZM based on traction–separation laws to simulate stiffness degradation, delamination, and progressive interfacial failure. Appropriate boundary conditions, including fixed supports and applied loads or displacements, were defined to replicate the experimental loading conditions. In addition, a suitable failure criterion (e.g., Hashin criterion) was adopted to predict fiber and matrix damage under structural loading.

3.5. Overview of the Research Organization

This study was organized into two major components, each addressing a distinct research objective. The initial phase focused on material formulation and testing to establish the mechanical properties of BFRP composites. While the second phase explored the integration of these materials into structural components through design optimization and performance evaluation, as highlighted in Fig. 3.1. The Fig. summarizes the two major projects undertaken in the study. Each of these projects is described in detail in the subsequent chapters to provide a coherent understanding of the research progression. The overall process ensured a progressive transition from material-level understanding to full-scale application assessment. Chapters Four and Five describe the material development and mechanical testing of BFRP composites, while Chapter Six focuses on their structural integration, performance evaluation, and validation within the context of automotive design.

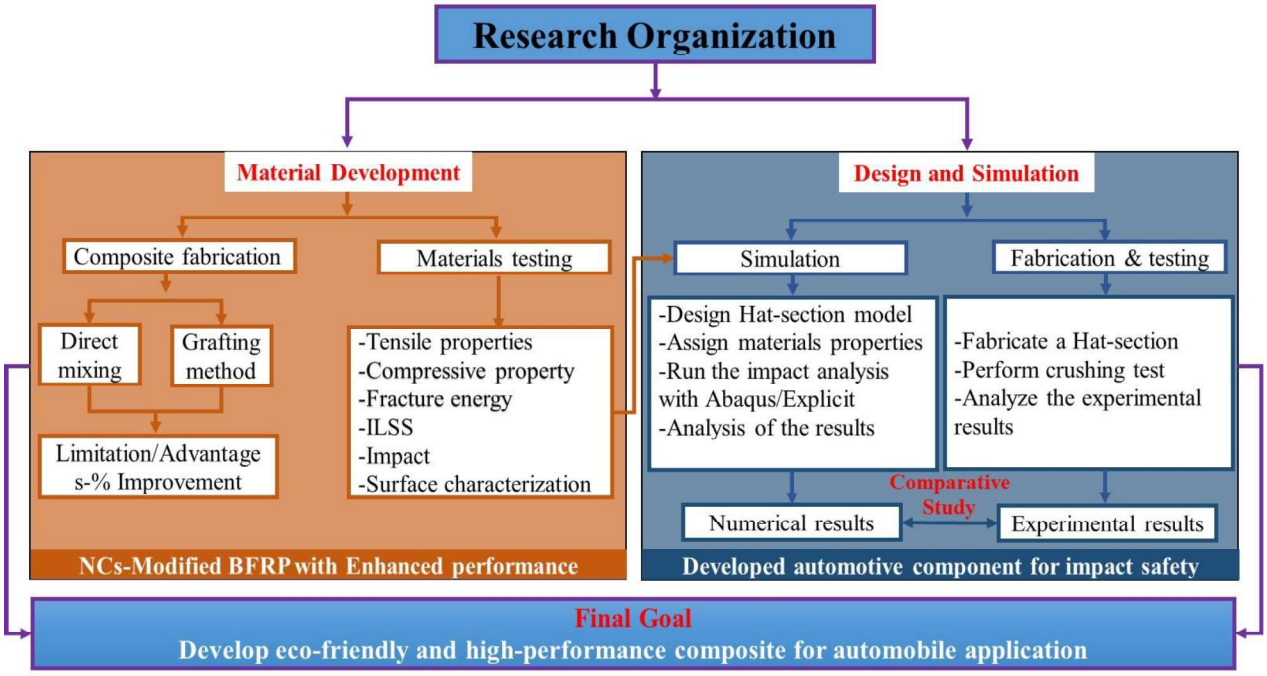

Fig. 3.1. Research methodology framework for the development of NC-modified BFRP composites for automobile applications

CHAPTER FOUR

4. EFFECT OF NC DISPERSION ON BF/EPOXY COMPOSITES

4.1. Introduction

Basalt fiber reinforced polymer composites have gained widespread adoption across various industries, including aerospace, automotive, marine, and structural engineering, due to their exceptional mechanical properties, high corrosion resistance, and environmental friendliness. These composites offer a lightweight yet durable alternative to traditional composite materials, making them ideal for applications requiring high strength-to-weight ratios and long-term durability.

However, despite their advantages, BFRPs are susceptible to certain damage mechanisms that can compromise their performance and longevity. Common issues include interfacial debonding and delamination, as shown in Fig. 4.1, which usually arise due to weak interfacial bonding strength between BF and polymer matrix. These defects not only weaken the structural integrity of the composite but also reduce its long-term reliability. Addressing these challenges through advanced material modifications and improved fabrication techniques is crucial for enhancing the overall durability and effectiveness of BFRP composites in demanding applications. Both thermoplastic and thermosetting polymers are commonly used as matrix materials in the production of BFRP composites. Among them, thermosetting polymers, particularly epoxy resins, are widely preferred due to their low viscosity and relatively low processing temperatures, which facilitate effective fiber wetting and enhance interfacial bonding. In this study, the term BFRP specifically refers to basalt fiber-reinforced epoxy composites. Epoxy resins also exhibit superior mechanical properties, including high strength, stiffness, and excellent chemical resistance, making them well-suited for demanding structural applications

across industries such as aerospace, automotive, and civil engineering [67]. Their ability to maintain structural integrity under various environmental conditions further contributes to their widespread use in composite manufacturing. Despite their advantages, epoxy resins have certain limitations, such as brittleness and low fracture toughness.

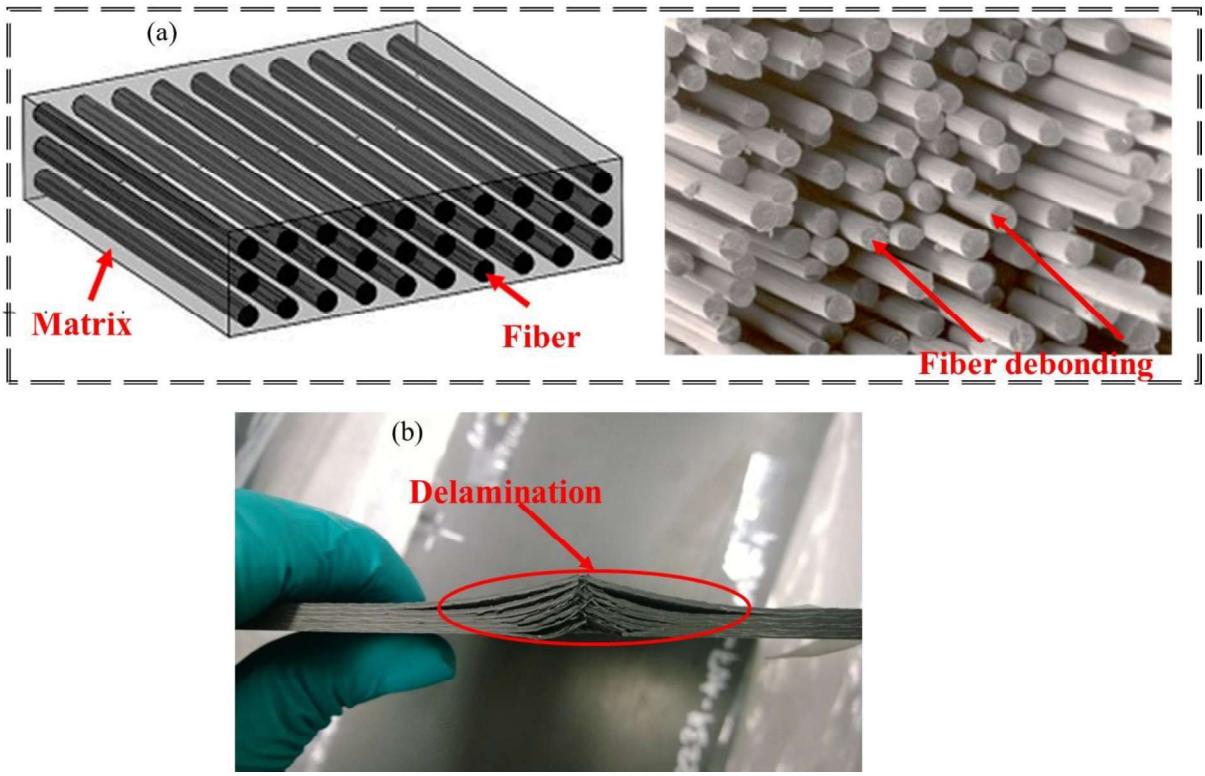

Fig. 4.1. Common damage mechanisms in BFRP composite: (a) fiber debonding and (b) interfacial delamination

To overcome these challenges, researchers have explored various approaches, including the incorporation of nanoparticles, additives, and hybrid reinforcement strategies, to improve matrix toughness and enhance impact resistance. Previous studies have consistently shown that incorporating nanomaterials into FRPs can significantly enhance fiber–matrix adhesion and improve matrix toughness [5,30]. Two primary techniques are commonly employed to achieve these enhancements: matrix modification and fiber surface treatment, both of which have been

thoroughly investigated in this study. Matrix modification involves dispersing nanomaterials within the resin to enhance matrix toughness and improve mechanical properties, while fiber surface modification entails directly treating the fiber surface with nanomaterials to strengthen interfacial bonding.

In this study, an eco-friendly nanomaterial, nanocellulose (NC), was utilized to enhance the performance of BFRP composites using both methods. However, one of the major challenges in incorporating NC into fiber-reinforced polymers (FRPs) is its poor dispersibility within the polymer matrix. This issue stems from the inherently hydrophilic nature of NC, which contrasts with the predominantly hydrophobic characteristics of most polymer matrices, such as epoxy resins, leading to difficulties in achieving uniform dispersion and effective reinforcement. As a result, NC tends to aggregate or form clusters within the matrix rather than dispersing uniformly, leading to inefficient stress transfer and inconsistencies in mechanical properties. Despite these challenges, some researchers have successfully demonstrated this approach in enhancing the performance of FRPs by controlling processing parameters such as mixing time, temperature, and the weight percentage of NC in the polymer matrix. Parveen et al. [5] utilized cellulose microcrystals (CMC) to enhance the glass fiber/epoxy matrix interface and reported that a 1 wt.% CMC dispersion achieved optimal performance, significantly improving interlaminar shear strength by 65% and flexural strength by 76%. Shao et al. [30] reported that the addition of cellulose nanofibers (CNFs) to epoxy matrices enhanced the fatigue life of carbon fiber/epoxy composites, with 0.3 wt.% CNF achieves the longest fatigue life. CNF modification improved adhesive strength at the fiber–matrix interface, reducing interfacial debonding. At 0.8 wt.% CNF, debonding was nearly eliminated, emphasizing the importance of optimizing CNF content for improved fatigue resistance.

However, this approach has not been widely explored in BFRP composites, highlighting the need for further investigation as demonstrated in this chapter. The limited research in this area highlights the critical need to optimize NC dispersion specifically for BFRP systems to fully understand the associated challenges and the extent of its potential benefits. Proper dispersion of NCs plays a crucial role in enhancing interfacial bonding, mechanical strength, and overall composite performance. However, without systematic investigation, the effectiveness of NC integration in BFRP composites remains uncertain. To evaluate the impact of NC modification, mechanical testing was conducted, including tensile, short beam shear, and impact strength assessments. Additionally, a detailed morphological analysis of the fracture surface was performed using field emission scanning electron microscopy (FESEM) to examine fiber–matrix interactions, crack propagation, and failure mechanisms. The results were compared with those of unmodified (reference) BFRP composites to assess improvements in structural integrity, interfacial adhesion, and resistance to mechanical stress. This comparative analysis provides valuable insights into the effectiveness of NC incorporation and helps establish guidelines for optimizing its application in BF/Epoxy composites.

4.2. Materials and Methods

4.2.1. Materials

Twill-woven BFs with an area density of 210 g/m² (Keunyung, Republic of Korea) were used as reinforcement materials. The epoxy resin employed was bisphenol A diglycidyl ether (YD-128; Kukdo Chemical, Republic of Korea), with an epoxide equivalent weight of 185–190 $g \cdot eq^{-1}$ and a density of approximately 1.16 g/cm³ at 25 °C. The curing agent used was 4,4-methylenedianiline (MDA; density: 1.15 g/cm³; Aldrich Chemical, Republic of Korea). The mixing ratio of epoxy to hardener was maintained at 1:0.25. CNF and CNC powders were

commercially obtained from ANPOLY (Republic of Korea). CNF, with an average aspect ratio of 300 and a zeta potential of –56.1 mV, was produced via TEMPO-mediated oxidation, sterilized, and spray-dried. CNC, on the other hand, was produced via acid hydrolysis, with an average aspect ratio of 22 and a zeta potential of –37.0 mV. The key properties of CNF and CNC, as provided by the manufacturer, are listed in Table 2.3.

4.2.2. Preparation and Mixing of NCs into Epoxy Resin

The CNF and CNC powders were first accurately weighed and oven-dried at 50 °C until a constant weight was achieved to ensure complete moisture removal. This drying step was essential to prevent any adverse effects of residual moisture on the resin curing process and the overall quality of the final composite. Following this, the NC powders were incorporated into the epoxy resin at varying weight percentages ranging from 0.3 wt.% to 0.7 wt.%, with increments of 0.2 wt.%. This concentration range was selected based on previous studies, which reported that NC contents above 0.5 wt.% can significantly increase resin viscosity and promote agglomeration, leading to poor dispersion and difficult fiber wetting during composite fabrication [119]. Although rheological or viscosity measurements were not directly conducted in this study, the increase in matrix volume fraction presented in with increasing NC content indirectly indicates a corresponding rise in viscosity, thereby leading to restricted resin flow during processing. To ensure effective dispersion of the NCs within the resin matrix, the mixtures were stirred continuously at room temperature for a minimum of 15 h using a mechanical stirrer at a constant speed of 500 rpm, as shown in Fig. 4.2. This prolonged and controlled mixing process was done to achieve a uniform distribution of the NC particles, which is key to enhancing the interfacial bonding, matrix toughness, and mechanical performance of the resulting composite. After the initial mixing phase, the appropriate amount of hardener was

added to the NC/Epoxy mixture. This was further stirred for an additional 30 minutes to ensure proper homogenization. To eliminate any entrapped air bubbles that may have formed during the mixing stages, the final mixture underwent a vacuum degassing procedure. This step was critical, as air voids can significantly weaken the mechanical properties and structural integrity of the cured composite material [5,95].

Fig. 4.2. Mechanical stirring setup for dispersion of NCs into epoxy resin

4.2.3. NC-Dispersed BFRP Fabrication

The composites were fabricated using the hand layup method, where degassed epoxy resin was carefully impregnated onto desized BFs to ensure uniform distribution and proper wetting of the fibers. This process was crucial for achieving strong interfacial bonding between the fibers and the matrix. After layup, the laminates were vacuum bagged to remove excess resin and trapped air, which could otherwise lead to defects such as voids or weak interlaminar bonding. The vacuum bagging process ensured consistent fiber volume fraction and improved overall

composite quality. The laminates were then cured in an autoclave at 125 °C under a controlled pressure of 7 bar for 3 h, which facilitated complete polymerization of the epoxy matrix.

4.2.4. Mechanical Property

The tensile, compressive, and ILSS tests were performed using a universal testing machine (UTM; ST-1002, SALT, Republic of Korea) equipped with a 30 kN load cell. A crosshead displacement rate of 2 mm/min was applied during all tests, which were conducted at room temperature. The tensile specimens were prepared in accordance with the ASTM D3039 standard, with dimensions of 100 mm × 15 mm × 0.6 mm. To ensure precise strain measurements along the longitudinal axis, a uniaxial strain gauge was affixed to the center of each specimen. This setup enabled the accurate recording of strain under tensile loading conditions, allowing for the determination of tensile modulus.

A short-beam shear test was conducted following the ASTM D2344 standard. The test specimens had a span-to-depth ratio of 4:1, and the specimen width was twice the thickness. The dimensions of the ILSS test specimens were 18 mm × 6 mm × 3 mm, and the span length was 12 mm. The ILSS was calculated as follows:

$$\tau = 0.75\frac{P}{bd}, \qquad 3.1$$

where τ is the ILSS (MPa); P is the maximum force (N); and b and d are the specimen width and thickness (mm), respectively.

The Izod impact strength was conducted using a low-energy pendulum impact tester (IT 504, Tinius Olsen, United Kingdom) following the ASTM D256 standard. Before the test, a 2 mm deep "V" notch was precisely created at the center of each specimen using an impact

specimen notcher (Model 899, Tinius Olsen, United Kingdom) to serve as a stress concentrator. The dimensions of the impact specimens were 63.5 mm × 12.7 mm × 3 mm. The pendulum energy used for testing was 12.6 J, and all tests were conducted at room temperature. For reliability and accuracy, at least five tests were conducted for each specimen type.

4.2.5. Scanning Electron Microscopy

The fracture surfaces of the composites after ILSS tests were analyzed using a field-emission scanning microscope (NOVA NanoSEM 450, FEI, USA). The specimens were mounted on the sample holder with carbon tape to ensure stability during analysis. To enhance the conductivity of the specimen and achieve high-quality images, a thin platinum coating (~14 nm thick) was applied using a sputter coater. SEM imaging was performed at an accelerating voltage of 10 kV to enable detailed visualization of the microstructural features and failure mechanisms.

4.3. Results and Discussion

4.3.1. Tensile Property

The mechanical performance of BFRP composites fabricated by directly mixing the two types of NCs into the epoxy resin shows slight differences, primarily due to variations in their morphological structures and dispersion behaviors. CNCs are crystalline in nature with relatively small particle sizes, while CNFs have a fiber-like and entangled structure. These distinct morphologies significantly influence their reinforcing effects and dispersibility in the epoxy resin. However, both CNCs and CNFs tend to form agglomerations within the polymer matrix, particularly at higher concentrations. This aggregation limits their effectiveness in achieving optimal reinforcement of the composite. The average optimal tensile strength for both NC-mixed BFRP composites was increased by 10%, reaching 430 MPa, as shown in Fig. 4.3. The abovementioned increase can be attributed to the matrix toughening effect, which promotes more

uniform stress distribution within the composite structures [86]. However, the stiffness of the composites decreased with the addition of NCs to the epoxy resin. This reduction in stiffness is primarily due to the increased viscosity of the resin and the decreased fiber volume fraction caused by the incorporation of NCs [120]. A slight increase in stiffness was observed at 0.5 wt.% NCs, likely due to the optimal dispersion of NCs within the epoxy resin. At this concentration, the NC particles are more uniformly distributed, improving resin flow and enhancing the overall matrix properties without significantly disrupting fiber wet-out. This balance results in a temporary stiffness enhancement before the negative effects of excessive NC loading, such as agglomeration and increased viscosity, begin to dominate. As the NC concentration increased from 0.5 wt.% to 0.7 wt.%, only the tensile strength of CNC-modified BFRPs showed improvement, while the stiffness of both CNC- and CNF-modified BFRPs continued to decline. This reduction in stiffness is attributed to the challenges of achieving uniform fiber impregnation at higher NC concentrations. Since stiffness is primarily governed by the fiber's properties, insufficient resin penetration and fiber wet-out at elevated NC loadings compromise the composite's structural integrity, leading to a decline in overall stiffness. Similar observations were reported by [5,120]. The increased viscosity of the resin impairs its ability to flow efficiently and fully saturate the fiber bundles. As a consequence, resin-rich regions and voids develop within the composite, weakening fiber–matrix bonding and compromising overall structural integrity. This phenomenon directly impacts the fiber volume fraction, as poor impregnation leads to a relative increase in resin content at the expense of fiber reinforcement.

Table 4.1 illustrates this effect, showing that the average fiber volume fraction in NC-modified BFRPs decreased to 50%, while void content increased to 6.6%. These changes

highlight the challenges of achieving optimal fiber wet-out and uniform dispersion at higher NC concentrations, ultimately affecting composite performance.

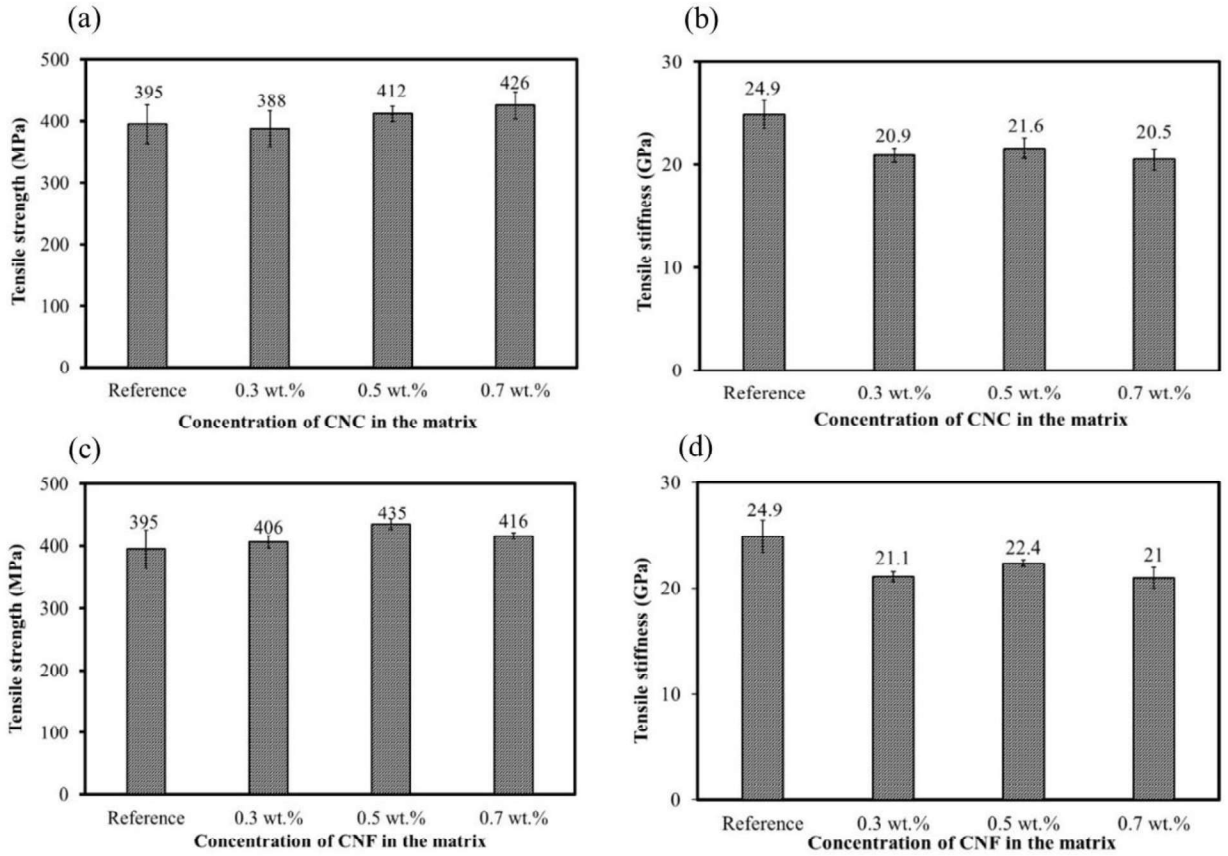

Fig. 4.3. Tensile strength and stiffness of BFRPs at different concentrations of NCs in epoxy matrix: (a & b) CNC and (c & d) CNF

Table 4.1. Fiber volume fraction and void content in NC-mixed BFRP composites

Sample (%)	Fiber volume fraction (%)	Matrix volume fraction (%)	Actual density (g/cm^3)	Void content (%)
Reference				
—	65	35	1.98	5.3
CNF-mixed BFRP				
0.3	58	42	1.88	5.5
0.5	58	42	1.83	6.2
0.7	52	48	1.78	6.3
CNC-mixed BFRP				
0.3	59	41	1.91	4.5
0.5	58	42	1.84	5.6
0.7	50	50	1.75	6.9
CNF-grafted BFRP				
0.5%	62	38	1.95	4.9
1.0%	62	38	1.98	3.4
1.5%	60	40	1.94	3.8
2.0%	55	45	1.84	5.6
CNC-grafted BFRP				
0.5%	63	37	1.96	4.9
1.0%	63	37	1.97	4.4
1.5%	61	39	1.94	3.0
2.0%	58	42	1.91	4.0

4.3.2. Interlaminar Shear Strength

The incorporation of NCs into the epoxy resin does not significantly improve the ILSS of BFRP composites, as evidenced in Fig. 4.4. Although some enhancements are observed, they are limited with increasing NC content. This can be attributed primarily to poor dispersion of NCs and the resulting increase in resin viscosity, which hinders effective fiber wetting and restricts the removal of excess resin between adjacent BF layers. These fabrication limitations result in the formation of resin-rich zones, ultimately compromising interlaminar bonding and reducing the initial stiffness (slope) of the modified BFRPs, as shown in the ILSS–displacement curves in

Fig. 4.4(b) and 4.4(c). In Fig. 4.4(a), the ILSS of CNC-mixed BFRP improves by approximately 25%, from 28 MPa in the reference sample to 35 MPa at 0.5 wt.% CNC loading. However, increasing the CNC content to 0.7 wt.% does not yield additional gains. This stagnation arises from CNC agglomeration at higher loading due to inadequate dispersion, which results in localized stress concentrations and increased void content, as confirmed by SEM analysis in Fig. 4.5(b). These resin-rich areas impair shear stress transfer across the fiber-matrix interface, explaining both the drop in the initial slope and the unstable post-peak behavior of the curves.

In Fig. 4.4(c), CNF-modified composites exhibit a more modest ILSS increase of 10% at 0.7 wt.% compared to the reference. However, the ILSS displacement curves in Fig. 4.4(d) showed a higher initial slope than the CNC counterpart. This behavior is consistent with the improved dispersion of CNFs, attributed to their higher negative zeta potential, which leads to stronger electrostatic repulsion and a reduced tendency for agglomeration. Fig. 4.5(c) confirms this, showing a more uniform fractured surface morphology with fewer resin-rich zones, indicating better interfacial bonding and matrix continuity. Nevertheless, despite superior dispersion, CNFs contain a higher fraction of amorphous regions, limiting their capacity to reinforce the matrix at a molecular level compared to the more crystalline CNCs. Consequently, while CNFs enhance toughness and reduce agglomeration-induced defects, their structural limitations result in only modest ILSS gains. The reference sample, shown in Fig. 4.5(a), exhibits smooth fractured surfaces and exposed fiber surfaces, indicative of interfacial failure and poor bonding. This explains the low ILSS and steep post-peak drop observed in the reference curves of Fig. 4.4.

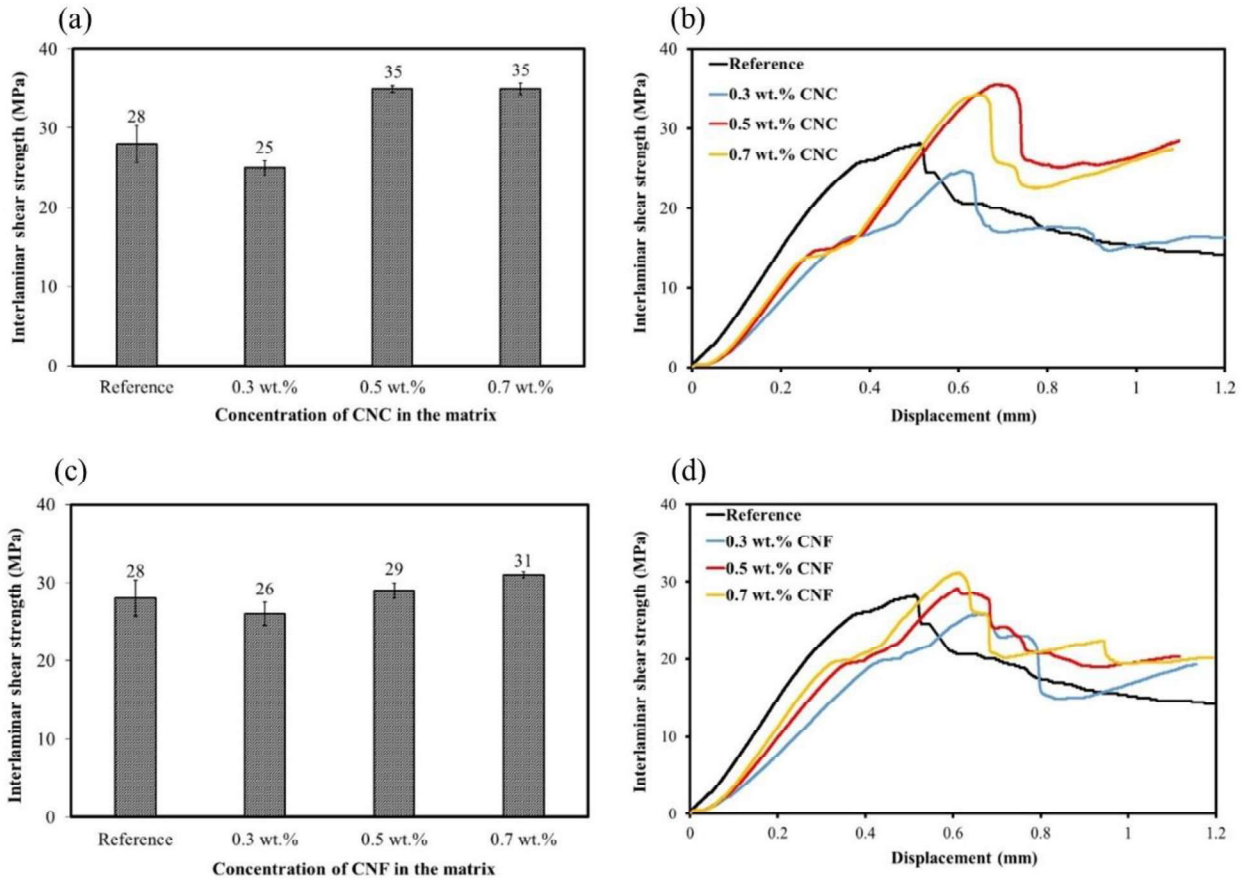

Fig. 4.4. ILSS and Shear stress-displacement curve at different concentrations of NCs in epoxy matrix: (a & b) CNC and (c & d) CNF

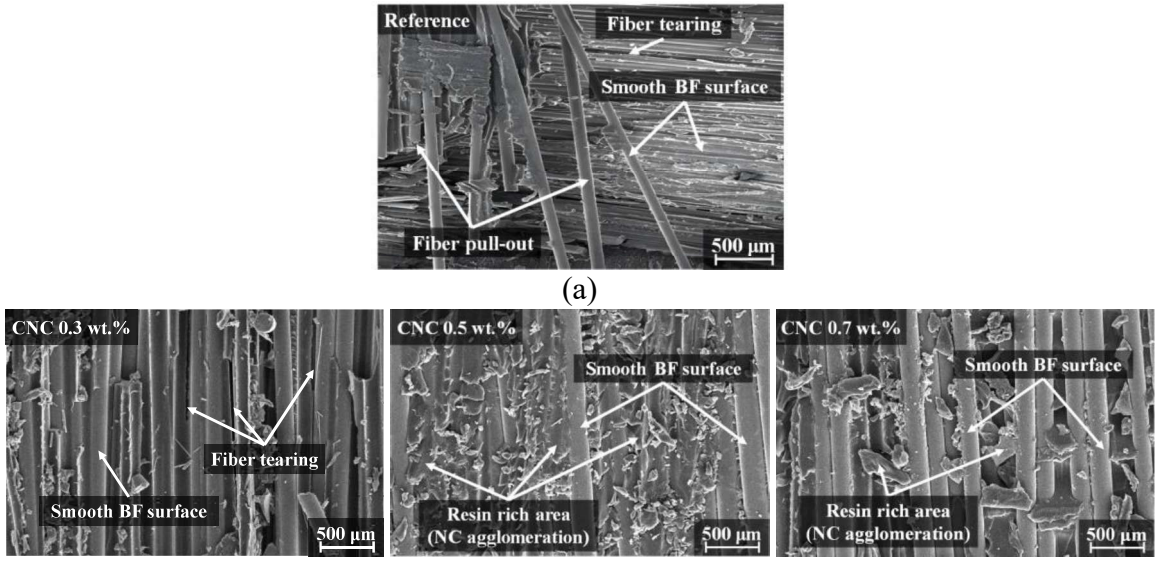

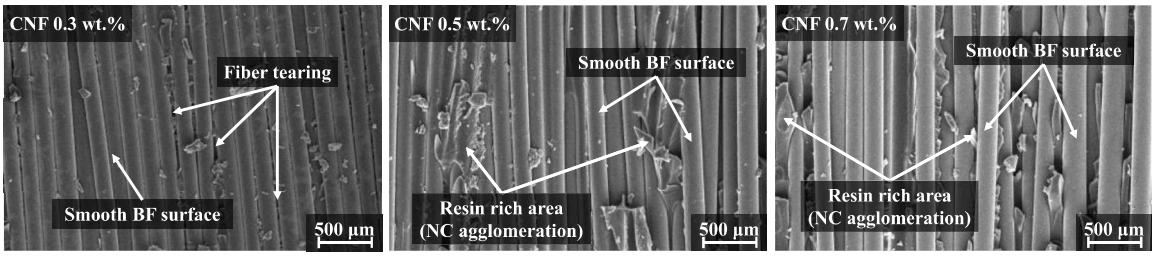

(c)

Fig. 4.5. Microstructural fractured surfaces of BFRPs after the ILSS test at different concentrations of NCs in epoxy resin: (a) Reference, (b) CNC, and (c) CNF

4.3.3. Izod Impact Strength

Fig. 4.6 illustrates the Izod impact strength of BFRP composites modified with CNCs and CNFs at varying concentrations within the epoxy matrix. The observed trend closely aligns with the ILSS results, highlighting the influence of NC dispersion on impact resistance. For CNC-modified BFRPs, impact strength peaks at 0.5 wt.% CNC loading, showing a 30% improvement compared to the reference BFRP composite. However, further increasing the CNC content to 0.7 wt.% results in a decline in impact resistance, likely due to agglomeration and reduced matrix uniformity. In contrast, CNF-modified BFRPs exhibit a steady increase in impact strength up to 0.7 wt.% CNF, achieving a maximum improvement of approximately 16%. Additionally, CNC-enhanced composites consistently outperform their CNF counterparts in impact resistance. This can be attributed to the superior matrix toughening effect of highly crystalline CNCs, which improve energy absorption by promoting controlled delamination and crack deflection under impact loading. However, this toughening effect does not extend beyond the critical concentration of 0.5 wt.% CNCs due to the aggregation of NC nanoparticles, which introduces defects into the composite structure [121,122].

As the concentration of NC increases, a noticeable decline in impact strength, ILSS, and tensile properties is observed, particularly in CNC-mixed BFRP composites. This degradation in

mechanical performance is primarily attributed to inadequate and inconsistent fiber–matrix impregnation. At higher NC concentrations, the epoxy resin's viscosity increases significantly, impeding its ability to flow smoothly and fully infiltrate the fiber bundles. As a result, resin-rich regions, voids, and fiber-matrix debonding sites develop within the composite structure, leading to stress concentrations and premature failure under mechanical loading. Furthermore, the uneven distribution of NC particles exacerbates these issues by promoting agglomeration, which disrupts the uniform dispersion needed to enhance matrix toughness. This uneven dispersion weakens the composite rather than reinforcing it, negating any potential benefits of NC inclusion.

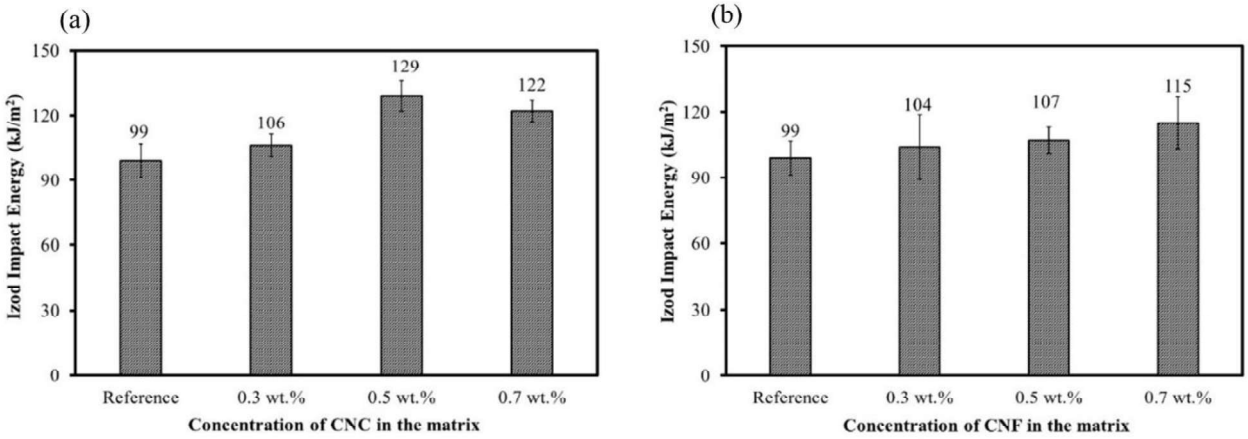

Fig. 4.6. Izod impact strength of BFRPs at different concentrations of NCs in epoxy resin: (a) CNC and (a) CNF

4.4. Concluding Remark

Direct mixing of NCs into epoxy resin resulted in only moderate improvements due to challenges such as poor dispersion, particle aggregation, and increased resin viscosity, particularly at higher NC concentrations. These limitations hindered the enhancement of impact strength, ILSS, and tensile properties, emphasizing the inefficiency of this method in significantly improving the interfacial bonding between basalt fibers and epoxy resin. Consequently, these findings suggest that alternative approaches, such as surface grafting of NCs

onto the fiber surface before resin infusion, may provide a more effective strategy for enhancing the overall mechanical performance of BF/epoxy composites. This alternative method has been thoroughly investigated in this study, with detailed findings presented in Chapter Five.

CHAPTER FIVE

5. IMPROVING BF/EPOXY BONDING USING NC GRAFTING APPROACH

5.1. Introduction

Incorporating NC directly into epoxy resin has proven challenging due to its poor dispersibility in hydrophobic media, often resulting in agglomeration, increased viscosity, and inconsistent distribution. However, their strong affinity for water, owing to their hydrophilic nature, allows them to form stable aqueous suspensions. To overcome the limitations of direct mixing (as discussed in Chapter Four), a novel grafting strategy was developed. In this method, NCs were first dispersed in water (see Fig. 5.1) and then chemically grafted onto silanol-functionalized BF surfaces before resin infusion. This approach enables precise localization of NCs at the fiber–matrix interface, where reinforcement is most effective. This leads to improving the interfacial adhesion, enhanced stress transfer, and reducing the likelihood of fiber delamination during mechanical testing. Additionally, grafting NCs onto the BF surface mitigates issues such as NC sedimentation and an increase in resin viscosity, ultimately contributing to greater consistency and mechanical performance in the composite structure.

Attaching nanoparticles, such as multi-walled carbon nanotubes (MWCNTs) [67], graphene [89], graphene oxide [65], or carbon nanotubes (CNTs) [66], onto the surface of BFs has been reported as a highly effective approach for enhancing the performance of BFRP composites, outperforming the conventional direct mixing method. Unlike simple mixing, which often suffers from issues like poor nanoparticle dispersion and increased resin viscosity, this surface modification technique directly alters the BF surface chemistry and morphology. As a result, it increases the surface functionality of the fibers and significantly improves fiber–matrix

adhesion, leading to notable enhancements in mechanical properties such as tensile strength, ILSS, and impact resistance.

Fig. 5.1. Homogeneous dispersion of NCs in aqueous solution

5.2. Materials and Methods

5.2.1. Materials

Twill-woven BF fabrics were employed as the reinforcing material, while a bisphenol A–based epoxy resin system served as the polymer matrix. The resin was cured with 4,4′-methylenedianiline (MDA), following the procedure outlined in Section 4.2.1. Before NC grafting, the BF surfaces were functionalized using an amino-based silane coupling agent to enhance interfacial compatibility and promote effective chemical bonding with the NCs.

5.2.2. Grafting Techniques and Reaction Mechanisms of NC on the BF Surface

The grafting of NC onto BF was carried out in a sequential step, as schematically represented in Fig. 5.2. The initial stage involved subjecting the commercial BFs to flame

treatment to effectively eliminate the factory-applied sizing agent. This step was essential, as residual sizing could interfere with subsequent chemical modifications by inhibiting the formation of strong chemical bonds between the fiber surface and the NC, ultimately weakening fiber–matrix interactions [120,123,124]. In addition to removing surface contaminants, the flame treatment also enhanced the reactivity of the fiber surface, improving its compatibility with the silane coupling agent and enabling more effective grafting of NC. Following the desizing process, a 1 wt.% aqueous solution of a silane coupling agent (N-2-(aminoethyl)-3-aminopropyltrimethoxysilane, KBM-603) was prepared. The solution was adjusted to approximately 4 pH using acetic acid, a necessary condition to increase the solubility of the silane in water and to catalyze its hydrolysis. The desized BFs were immersed in this solution, allowing for uniform coating. The fibers were then oven-dried at 100 °C for 2 h to promote the hydrolysis of the methoxy groups (–OCH_3) on the silane coupling agent to form silanol groups (–Si–OH). The unstable silanol groups underwent self-condensation to form a siloxane network (–Si–O–Si–), which linked the primary amine (–NH_2) and secondary amine (–NH) groups from the aminoethyl and aminopropyl chains of KBM-603, respectively [125]. This creates reactive sites for interaction with the hydroxyl groups (–OH) on the NCs through hydrogen bonding, as illustrated in Fig. 5.3 and confirmed by the XPS analysis in Fig. 5.7. The NCs, dispersed in deionized water, were then applied to the silane-treated BFs via a hand lay-up technique. This method allowed for uniform deposition of NC onto the fiber surfaces. To preserve the NC's structure and ensure a smooth, homogeneous coating, the treated fibers were dried at a controlled low temperature of 60 °C overnight using a conventional oven. The final amount of grafted NC was regulated by the concentration of NC in the aqueous dispersion, carefully matched to the NC-to-resin mass ratio used in the earlier NC mixing method (Section 4.2.2). This ensured that

the NC content in the final BFRP composites remained consistent across both treatment approaches, enabling a fair comparison of their effects on the composite performance.

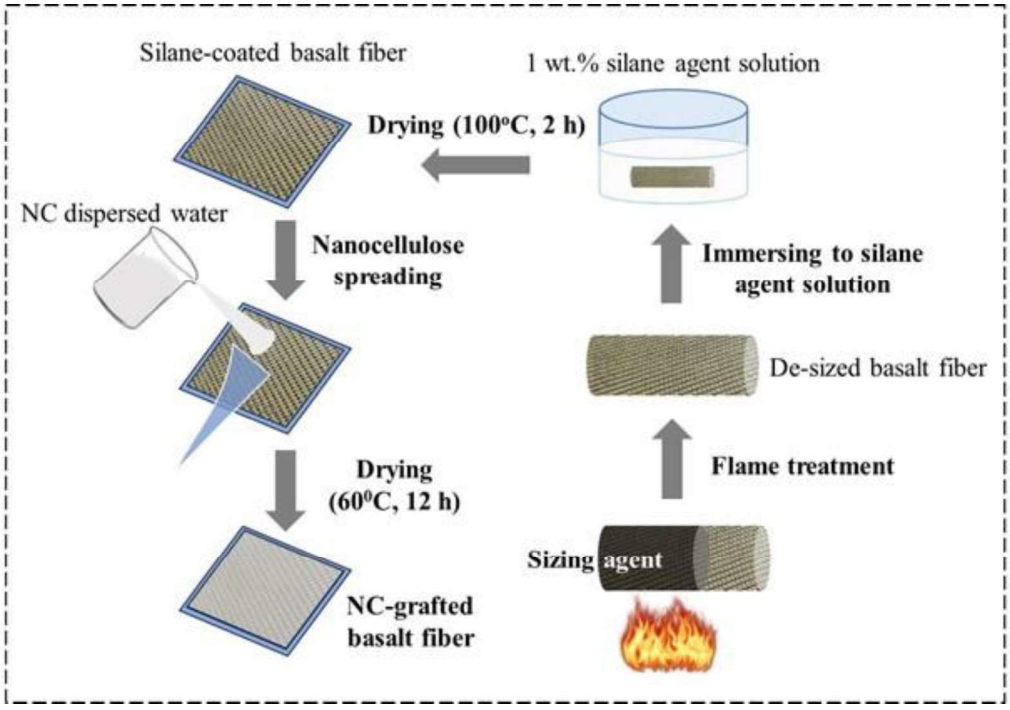

Fig. 5.2. Schematic representation of the NCs-grafted BFRP process

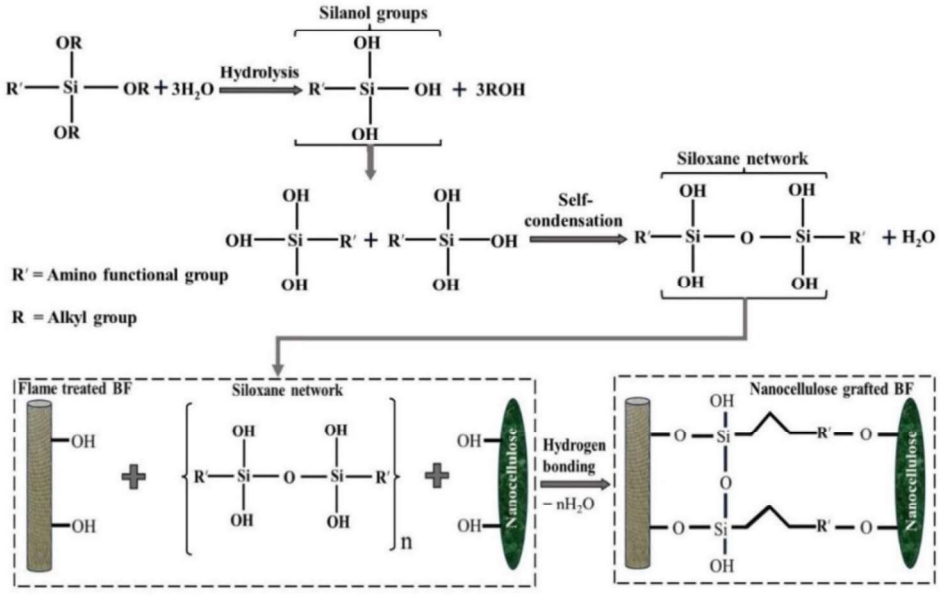

Fig. 5.3. Schematic diagram for the silane functionalization process and the bonding mechanism of nanocellulose on BF surfaces [92,125]

5.2.3. NC-Grafted BFRP Fabrication

The fabrication process was carried out using the conventional hand lay-up method, where the previously degassed epoxy-hardener mixture was uniformly applied to the NC-grafted BF to ensure thorough fiber impregnation. For tensile testing specimens, three layers of BF fabric were stacked, while a total of 18 layers were assembled for specimens intended for impact and interlaminar shear strength (ILSS) testing to meet the required thickness according to ASTM standards. After stacking, the laminates were vacuum bagged to remove excess resin and entrapped air from the layup, thereby minimizing void formation and ensuring better fiber–matrix adhesion. A constant vacuum pressure of 760 mm/Hg was maintained throughout the curing process to ensure optimal consolidation of the composite structure. The laminates were then cured in an autoclave under a pressure of 7 bar for 3 h at a temperature of 125 °C. A controlled heating and cooling rate of 5 °C/min was employed to minimize thermal stresses and prevent premature degradation or warping of the composite layers. The final cured composites exhibited average thicknesses of approximately 0.6 mm for tensile specimens and 3 mm for impact and ILSS specimens, respectively. To prepare specimens for mechanical testing, the cured laminates were precision-cut using a water jet cutting machine (T500-3015, Tops Co. Ltd., Republic of Korea). The cutting process was performed at a speed of 650 mm/min using a 0.82 mm nozzle, while the water pump pressure was maintained in the range of 60,000 to 70,000 psi. This method ensured accurate specimen dimensions with minimal thermal or mechanical damage to the edges, preserving the integrity of the composite structure for reliable testing.

5.2.4. Mechanical Property

The mechanical characterizations of the composites, including tensile property, ILSS, and impact resistance, were carried out following the same standardized procedures described in Section 4.2.4. Additionally, the analysis of the fractured surfaces of the composites after ILSS testing was performed using the same methodology outlined in Section 4.2.5. These consistent tests ensured the reliability and comparability of the results across different sample sets and modification methods.

5.2.5. X-ray Photoelectron Spectroscopy (XPS)

To study the chemical modifications occurring on the BF surface at various stages of the NC grafting process, XPS analysis was conducted using a Thermo Fisher Scientific (USA). This technique enables the identification of elemental composition and chemical bonding states, providing insight into surface functional group transformations. The spectral data were collected specifically for the O1s (528–540 eV) and C1s (280–292 eV) binding energy regions, which are indicative of key functional groups such as hydroxyl, carbonyl, and siloxane bonds formed during silane treatment and NC grafting. An Al–Kα radiation source was employed for excitation, offering high-resolution and accurate surface analysis. To ensure precision, the measurement spot size was maintained at 400 μm, while the energy step size was set to 0.10 eV per scan.

5.2.6. Moisture Absorption Test

A moisture absorption test was conducted to analyze the durability of the NC-grafted BFRP in a moisture-rich environment. This test is important because NCs possess high affinity for moisture, which could impact the composite's performance by increasing its moisture absorption [126,127]. The test was conducted specifically on the optimally formulated NC-grafted BFRP composites (1 wt.% CNFs, 1.5 wt.% CNFs, 1 wt.% CNCs, 1.5 wt.% CNCs, and

the reference) according to ASTM D5229. Pre-dried composite samples were submerged in a distilled water bath at a constant temperature of 50 °C. The specimens were periodically removed, gently wiped with cotton wool to remove water droplets, and weighed using a precise digital balance. The weight gain of each sample was regularly monitored and recorded at 24 h intervals until the specimens reached their saturation point. After the moisture absorption phase, the samples were subjected to mechanical characterization to evaluate the extent of degradation in ILSS, impact, and tensile strengths caused by moisture exposure. These tests were conducted under the same standards and conditions with the dried samples. The results of the moisture-exposed specimens were then compared with those of the dried samples to assess the effect of moisture absorption on the mechanical properties of the composite.

5.2.7. Fracture Toughness Test

Mode I and Mode II interlaminar fracture toughness were evaluated using the double cantilever beam (DCB) and end-notched flexure (ENF) methods, in accordance with ASTM D5528/D5528M [128] and ASTM D7905/D7905M [129], respectively. The Mode I fracture test corresponds to the opening mode, in which crack propagation is induced by tensile stresses acting normal to the crack plane, whereas Mode II corresponds to the sliding mode, in which crack propagation is induced by shear stresses acting parallel to the crack plane and perpendicular to the crack front, as illustrated in Fig. 5.4. For specimen preparation, a thin polyimide insert film was embedded at the mid-plane of the laminate during fabrication to create a predefined starter crack with an initial crack length of 50 mm, as specified by the relevant ASTM standards. The fabricated specimens were then cut to the required dimensions in accordance with the standard test geometries. Fracture toughness tests were carried out using a universal testing machine (Instron 240, UK) at a constant crosshead speed of 1.5 mm/min.

For the Mode I test, loading blocks were attached to both ends of the specimen, and the specimen was loaded under displacement control until crack initiation and stable crack propagation occurred. The crack length was monitored at 0.5 s intervals using digital image correlation (DIC), as illustrated in Fig. 5.5. In addition, vertical reference lines were marked at 1 mm intervals along a 60 mm span from the initial crack tip to facilitate crack length measurement. The load–displacement data obtained during the test were synchronized with the DIC images and subsequently used to calculate the Mode I fracture toughness using Equation (4.1). For the Mode II test, both pre-cracked (PC) and non-pre-cracked (NPC) specimens were tested using initial crack lengths of 20, 30, and 40 mm. The specimens were subjected to three-point bending in accordance with ASTM D7905, and the compliance calibration method was employed to determine the Mode II fracture toughness using Equation (4.2).

$$G_{IC} = \frac{3P\delta}{2Ba} \tag{4.1}$$

$$G_{IIC} = \frac{3mP_{max}^2 a_0^2}{2B} \tag{4.2}$$

Where P, B, and δ are the force, width of the specimen, and the crosshead displacement, respectively. P_{max} is the maximum force at crack length (a_0) equal to 30 mm, and m is the slope of the compliance (C) vs. crack length cube data as shown in Equation (4.3).

$$C = A + ma^3 \tag{4.3}$$

$C = \frac{1}{C_0}$, where C_0 is the slope of force versus displacement, and A is the intercept on the C-axis (see Fig. 5.6).

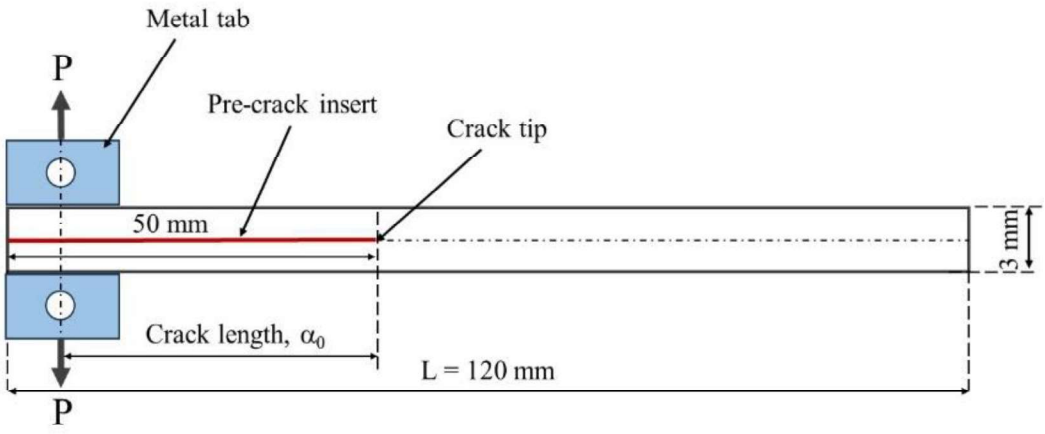

(a)

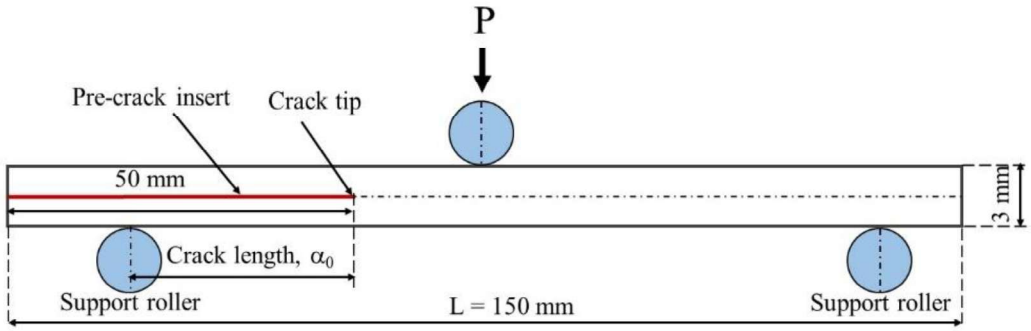

(b)

Fig. 5.4. Specimen testing configuration (a) DCB and (b) ENF

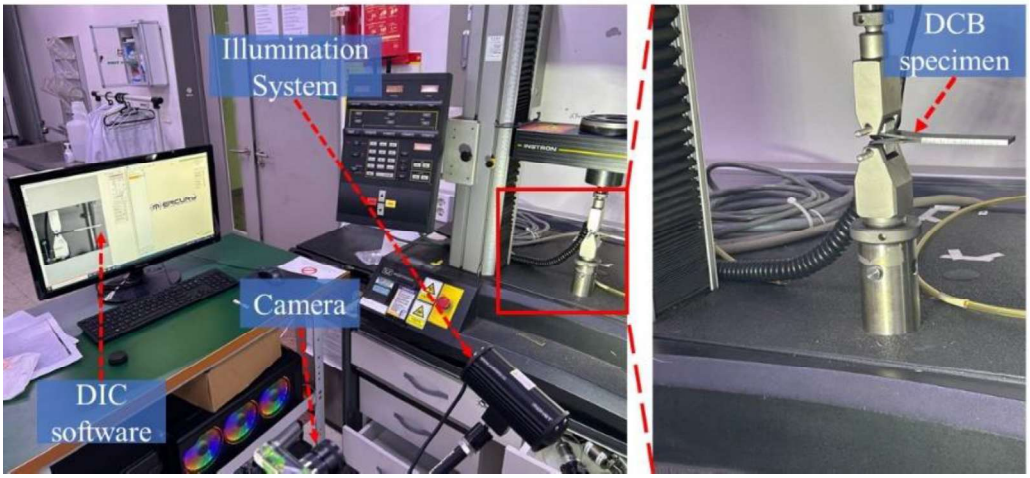

Fig. 5.5. DCB experimental setup

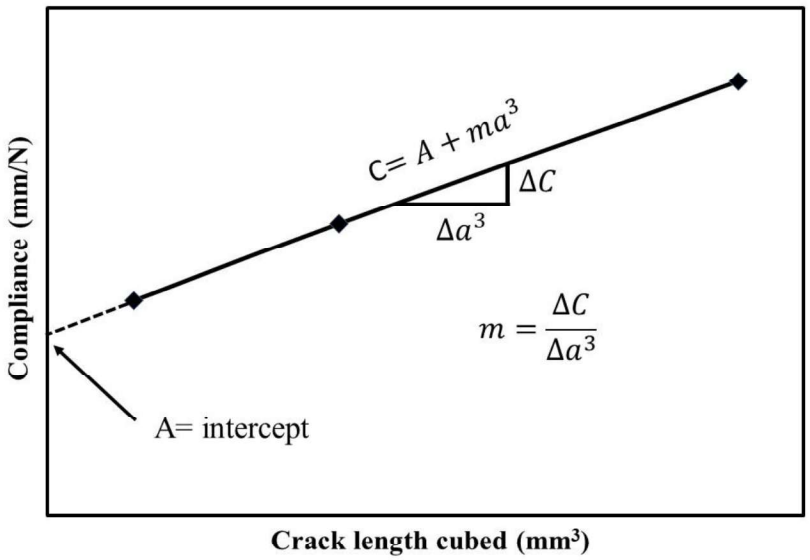

Fig. 5.6. Compliance coefficient determination

5.3. Results and Discussion

5.3.1. Surface Functional Groups of BF, NCs, and NC-Grafted BFs

To confirm the successful implementation of the NC-grafting process, the surface chemical composition and functional groups of BFs and NCs were characterized using XPS. The results, presented in Fig. 5.7 and reduction in surface carbon content, indicating the effective removal of the carbon-rich sizing layer. This change serves as a critical indicator of successful surface preparation for subsequent silane functionalization and NC grafting [130]. Moreover, the flame treatment not only removed the sizing agent but also introduced a higher concentration of oxygen-containing functional groups, such as hydroxyl (–OH), carboxyl (–COOH), and carbonyl (C=O) onto the BF surface via high-temperature oxidation. This chemical transformation, clearly as observed in Fig. 5.7(b) and (c), the observed carbon–oxygen functional groups are attributed to residual sizing agents remaining after decomposition [131,132], which further enhance the surface reactivity of the BFs. The presence of these polar groups plays a crucial role in promoting stronger chemical interactions with the silane coupling agent and nanocellulose, thereby enhancing the overall grafting efficiency.

The appearance of silicon and nitrogen peaks, as shown by the survey spectra in Fig. 5.7(a), confirms the successful functionalization of the BF surface by silane coupling agent [132,133]. The O1s spectra of the silane-treated BF, shown in Fig. 5.7(d), reveal characteristic peaks associated with Si-O-Si bonds at 530.8 eV, further demonstrating the effectiveness of the silane coupling agent coating process [132]. In addition, silane treatment increases the O/C ratio, indicating the presence of polar functional groups that enhance interfacial compatibility. This aligns with findings by Jia et al. [134], who reported that silane functionalization increased the concentration of oxygen-containing groups on the BF surface. While XPS is limited in detecting elements buried beneath surface coatings, several pieces of evidence collectively support the successful grafting of NCs onto the silane-treated BFs. Fig. 5.7(e–h) shows that the O1s spectra of NC-grafted BFs exhibit peak shapes and binding energies closely matching those of the corresponding CNC and CNF powders. The deconvoluted peaks of C-O (66.4%) and O=C-OH (33.6%) at 532.8 eV in the CNC powder are maintained after grafting, with comparable values of 66.1% and 33.9%, respectively. A similar trend was observed with the CNF powder and the CNF-grafted BF, as shown in Fig. 5.7(g) and (h), respectively. These peaks indicate that the NCs have been effectively attached onto the BF surface, which provides a reactive interface and enhances the fiber–matrix interaction in the composite material. Additionally, the marked increase in the O/C ratio and the disappearance of both Si and N signals after the NCs grafting step strongly suggest complete surface coverage by the oxygen-rich NC layers. This loss of Si and N peaks is attributed to the surface-sensitive nature of XPS (typically limited to ~5–10 nm), where the NC overlayer effectively shields underlying silane-related elements. Together, these provide strong evidence that the NC grafting reaction occurred successfully. The C1s spectra of the NC-grafted BF reveal new peaks associated with covalent bonding between the NCs and the

protonated amino functional groups (NH_3^+) introduced by the silane coupling agents [135]. This covalent bonding improved the chemical interaction between the NC layer and the silane-treated BF. Notably, a distinct peak attributed to C-NH_2 was observed at 287.5 ± 0.2 eV in both CNC- and CNF-grafted BFs. This peak highlights the presence of amino functional groups on the BF surface during the NC grafting process. The amino groups significantly enhance the adhesion between the NC-treated BF and the epoxy resin due to their high reactivity that promotes strong chemical bonding at the fiber–matrix interface [63]. Among the treatments, CNC grafting demonstrated the most effective adherence to the silane-treated BF surface, with a higher proportion of C-NH_2 (39.0%) compared to CNF (24.5%), indicating superior interfacial interaction and improved mechanical performance as observed in CNC-grafted BFRPs.

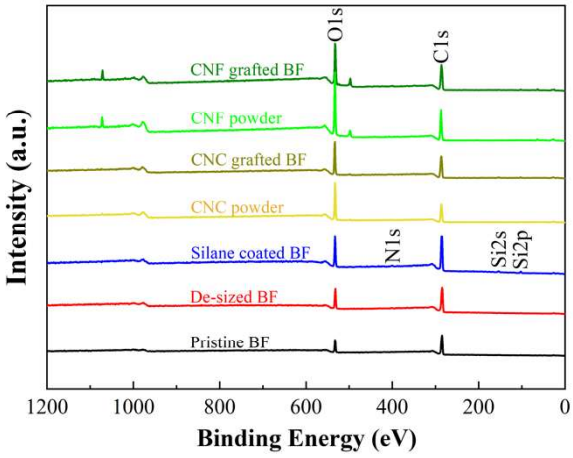
O1s
C1s
CNF grafted BF
CNF powder
CNC grafted BF
CNC powder
Silane coated BF
N1s
Si2s
Si2p
De-sized BF
Pristine BF
Intensity (a.u.)
1200
1000
800
600
400
200
0
Binding Energy (eV)

(a)

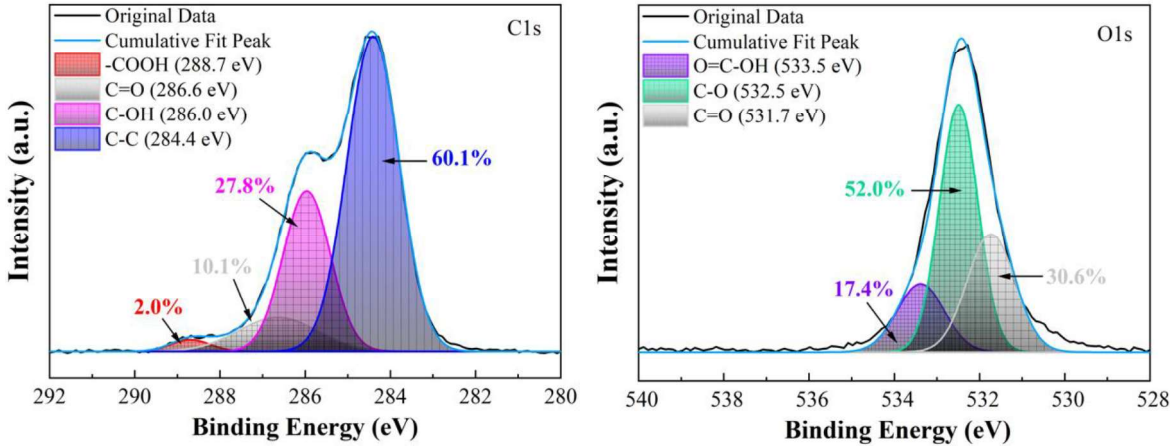
Original Data
Cumulative Fit Peak
-COOH (288.7 eV)
C=O (286.6 eV)
C-OH (286.0 eV)
C-C (284.4 eV)
C1s
60.1%
27.8%
10.1%
2.0%
Intensity (a.u.)
292
290
288
286
284
282
280
Binding Energy (eV)
Original Data
Cumulative Fit Peak
O=C-OH (533.5 eV)
C-O (532.5 eV)
C=O (531.7 eV)
O1s
52.0%
17.4%
30.6%
Intensity (a.u.)
540
538
536
534
532
530
528
Binding Energy (eV)

(b)

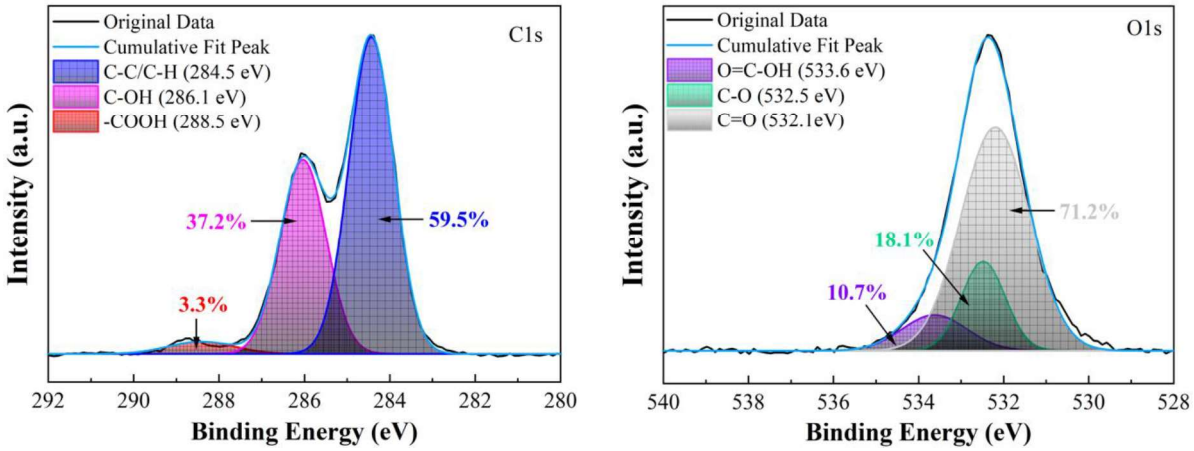
Original Data
Cumulative Fit Peak
C-C/C-H (284.5 eV)
C-OH (286.1 eV)
-COOH (288.5 eV)
C1s
37.2%
59.5%
3.3%
Intensity (a.u.)
292
290
288
286
284
282
280
Binding Energy (eV)
Original Data
Cumulative Fit Peak
O=C-OH (533.6 eV)
C-O (532.5 eV)
C=O (532.1eV)
O1s
71.2%
18.1%
10.7%
Intensity (a.u.)
540
538
536
534
532
530
528
Binding Energy (eV)

(c)

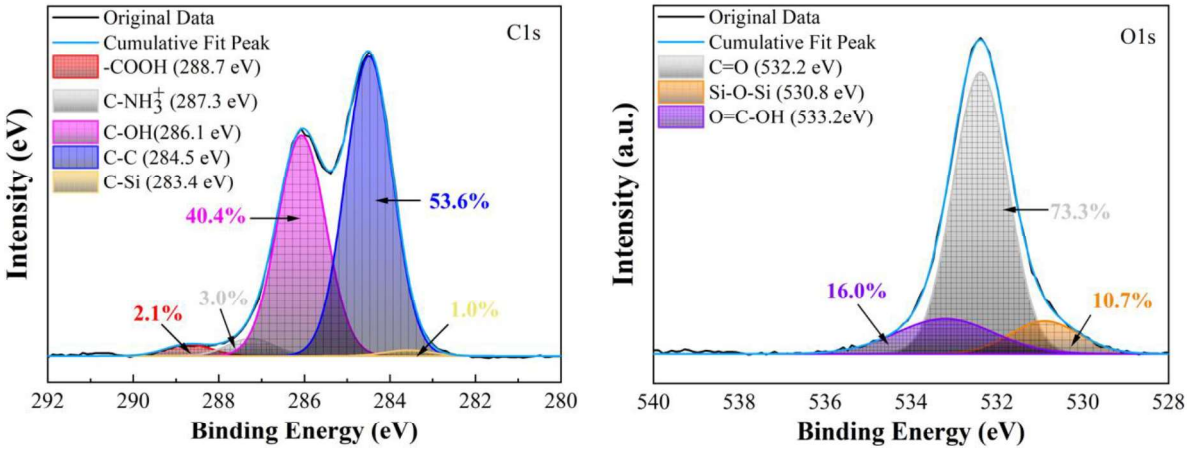
Original Data
Cumulative Fit Peak
-COOH (288.7 eV)
C-NH3+ (287.3 eV)
C-OH(286.1 eV)
C-C (284.5 eV)
C-Si (283.4 eV)
C1s
Intensity (eV)
40.4%
53.6%
2.1%
3.0%
1.0%
Binding Energy (eV)
Original Data
Cumulative Fit Peak
C=O (532.2 eV)
Si-O-Si (530.8 eV)
O=C-OH (533.2eV)
O1s
Intensity (a.u.)
73.3%
16.0%
10.7%
Binding Energy (eV)

(d)

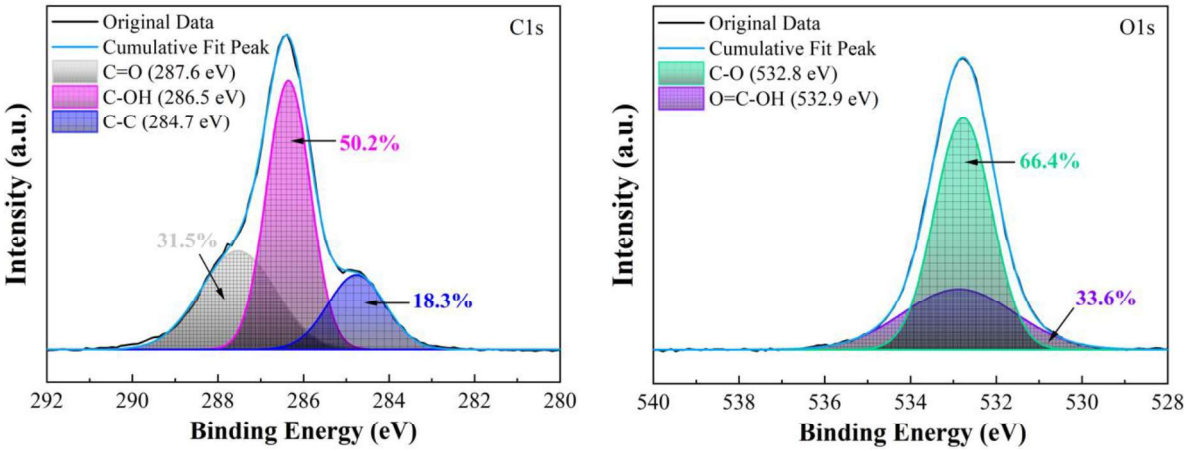
Original Data
Cumulative Fit Peak
C=O (287.6 eV)
C-OH (286.5 eV)
C-C (284.7 eV)
C1s
Intensity (a.u.)
50.2%
31.5%
18.3%
Binding Energy (eV)
Original Data
Cumulative Fit Peak
C-O (532.8 eV)
O=C-OH (532.9 eV)
O1s
Intensity (a.u.)
66.4%
33.6%
Binding Energy (eV)

(e)

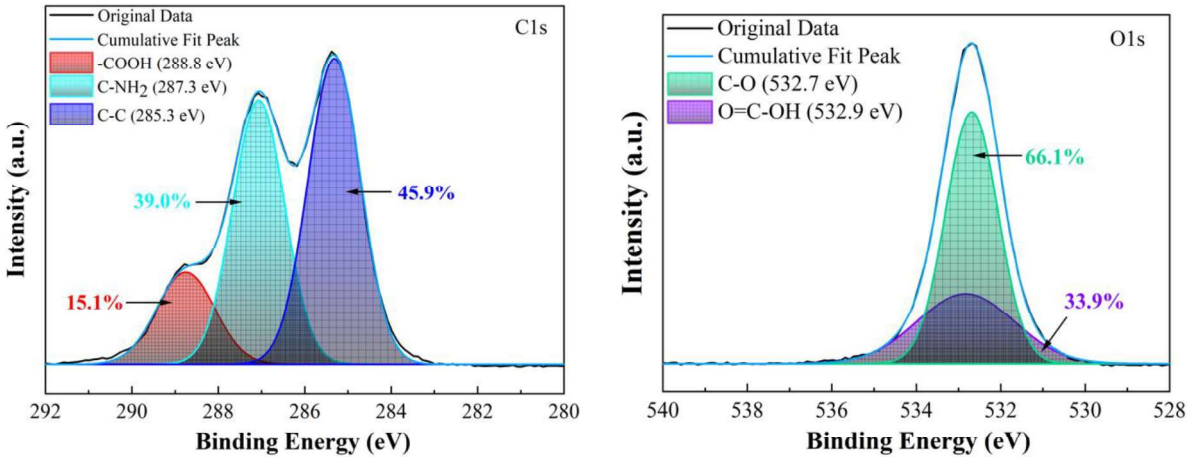
Original Data
Cumulative Fit Peak
-COOH (288.8 eV)
C-NH2 (287.3 eV)
C-C (285.3 eV)
C1s
Intensity (a.u.)
39.0%
45.9%
15.1%
Binding Energy (eV)
Original Data
Cumulative Fit Peak
C-O (532.7 eV)
O=C-OH (532.9 eV)
O1s
Intensity (a.u.)
66.1%
33.9%
Binding Energy (eV)

(f)

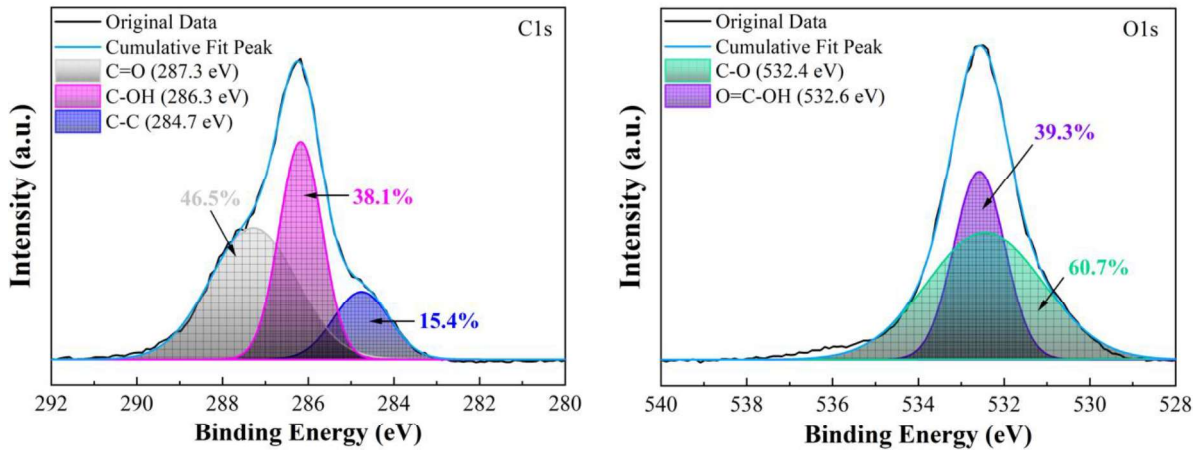

(g)

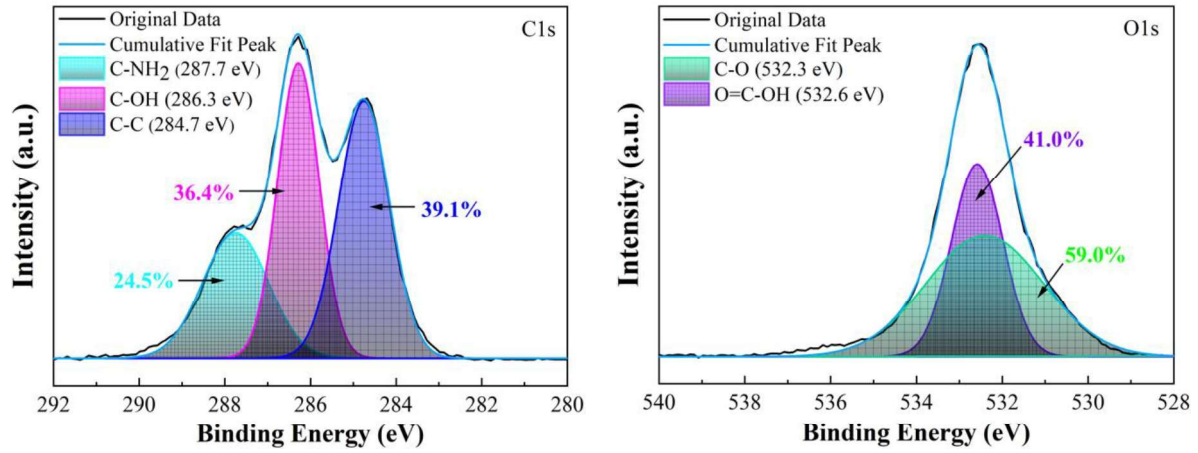

(h)

Fig. 5.7. XPS spectra results: (a) Survey spectrum, (b) Pristine BF, (c) Flame treated BF, (d) Silane treated BF, (e) CNC powder, (f) CNC-grafted BF, (g) CNF powder, and (h) CNF-grafted BF

Table 5.1. Atomic composition of NC powders and BF after grafting processes

Samples	Atomic Composition (%)				Atomic ratio (%)		
	Carbon (C)	Oxygen (O)	Silicon (Si)	Nitrogen (N)	O/C	Si/C	N/C
Pristine BF	80.0	20.0	0.00	0.00	0.25	0.00	0.00
Flame-treated BF	76.7	21.6	0.00	1.7	0.28	0.00	0.02
Silane-coated BF	72.0	21.4	3.5	3.1	0.30	0.05	0.04
CNC-grafted BF	66.0	31.7	2.3	0.00	0.48	0.04	0.00
CNF-grafted BF	62.5	35.6	1.82	0.00	0.57	0.03	0.00
CNC powder	57.6	42.4	0.00	0.00	0.74	0.00	0.00
CNF powder	55.0	45.0	0.00	0.00	0.82	0.00	0.00

5.3.2. Tensile Strength and Stiffness

The tensile behavior of NC-grafted BFRP composites is presented by the stress-strain curves in Fig. 5.8. As shown in Fig. 5.8(a), the CNC-modified composites exhibit an initial increase in tensile strength with rising CNC content, reaching an optimal performance at 1 wt.%. Beyond this point, specifically at 2 wt.%, the tensile strength plateaus or slightly declines. This reduction is likely due to poor epoxy infiltration caused by the increased CNC layer at higher concentrations, which leads to resin-rich zones and inadequate fiber wetting. These localized defects can initiate early failure and reduce load-bearing efficiency under tensile stress. In contrast, Fig. 5.8(b) shows that CNF-modified composites maintain a more consistent enhancement in tensile strength across all loading levels. The 1.5 wt.% CNF sample demonstrates the highest tensile performance. This improvement is attributed to the unique morphology of CNFs, which possess a high aspect ratio and an entangled network structure.

These characteristics facilitate better stress transfer between the matrix and fibers and contribute to improved crack bridging and deflection, thereby increasing both strength and toughness.

As illustrated in Fig. 5.9, the 1 wt.% CNC- and 1.5 wt.% CNF-grafted samples exhibit tensile strength improvements of approximately 16% and 22.8%, respectively, compared with the reference sample. The stiffness followed a similar trend, increasing alongside the strength, and did not show any significant reduction as compared to the results typically observed with the direct mixing method. This improvement indicates that surface grafting of NC enhances the fiber–matrix interfacial bonding without adversely affecting the resin's rheology, thereby preserving both strength and stiffness in the final composite. The effectiveness of NC grafting is strongly influenced by NC type and morphology. CNFs, due to their fibrous structure and ability to form continuous reinforcing networks, outperform CNCs in terms of tensile enhancement. Their alignment along the fiber axis and better mechanical interlocking make them a more efficient toughening agent in BFRP composites. Moreover, surface grafting ensures strong fiber–matrix adhesion without affecting resin flow, leading to a structurally uniform and mechanically robust composite laminate.

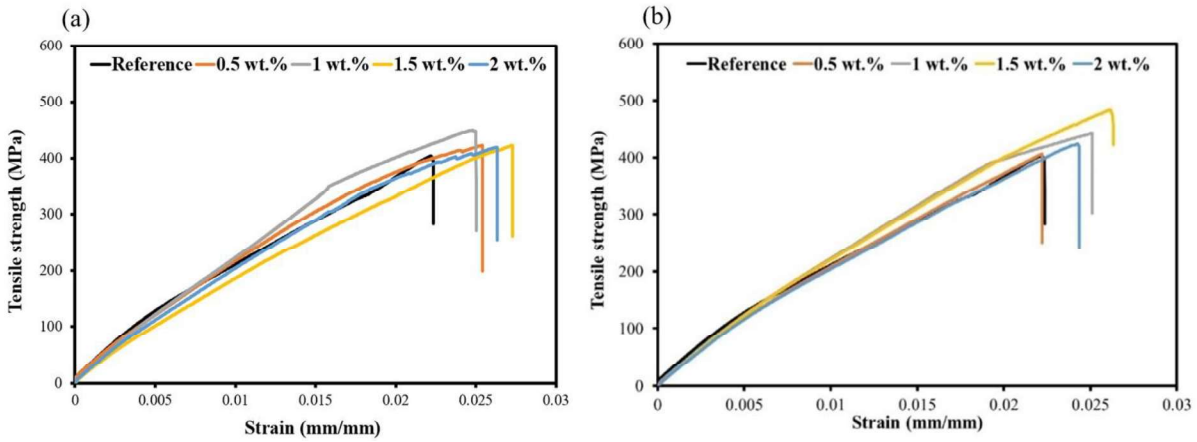

Fig. 5.8. Stress-strain curve of BFRPs at different concentrations of NCs in the grafting solution: (a) CNC and (b) CNF

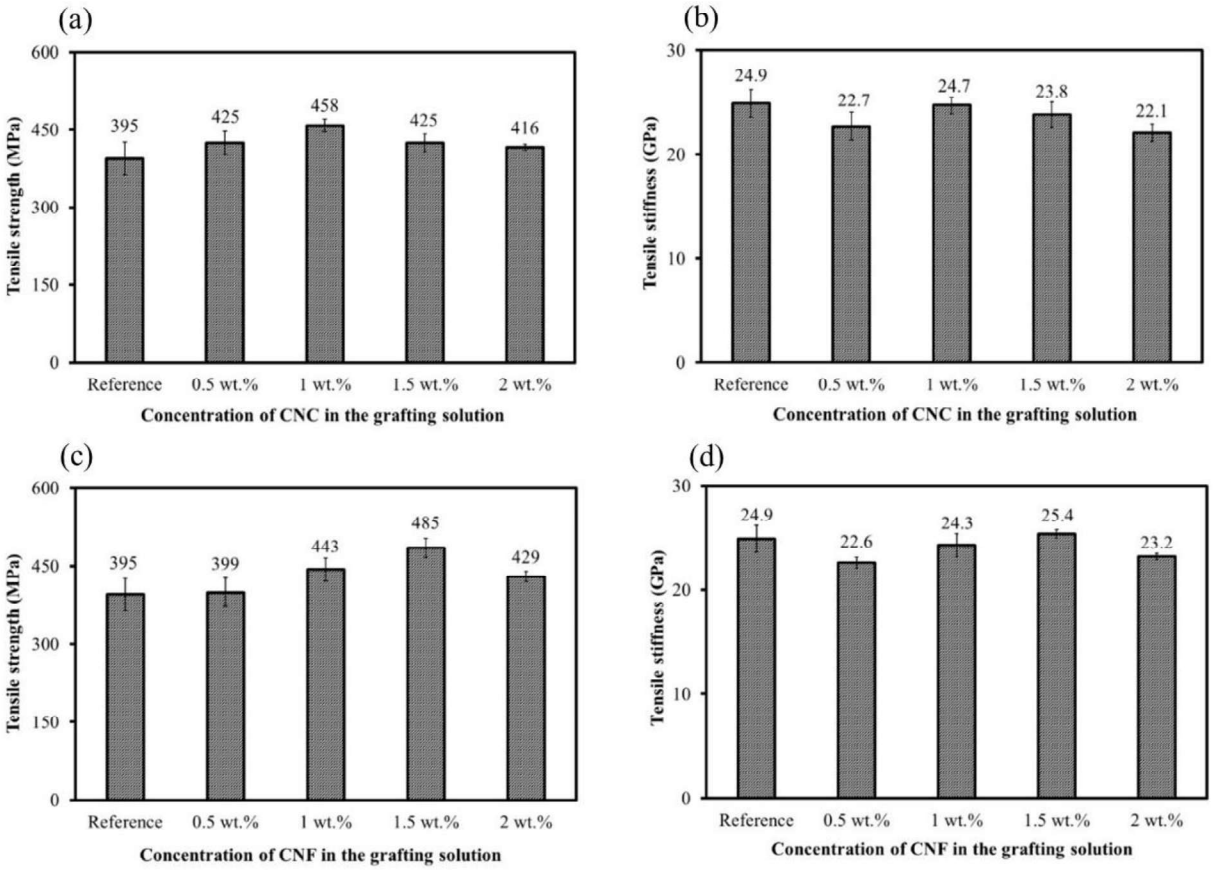

Fig. 5.9. Tensile strength and stiffness of BFRPs at different concentrations of NCs in the grafting solution: (a & b) CNC and (c & d) CNF

5.3.3. Interlaminar Shear Strength

The ILSS of FRPs is largely influenced by the quality of the interfacial bonding between fiber and matrix [136,137]. As shown in the ILSS–displacement curves in Fig. 5.10(a) and (b), the reference exhibits a lower initial slope compared with the NC-grafted samples, indicating reduced interfacial stiffness and early delamination due to poor bonding between BF and the epoxy matrix. The relatively smooth and inert surface of untreated BFs results in weak mechanical interlocking and insufficient chemical interaction with the resin, thereby compromising shear stress transfer efficiency across the ply. This weak interface causes premature failure, visible as an early and abrupt drop in load after peak stress. In contrast, the

samples modified with NC, particularly at 1.5 wt.% of both CNC and CNF, display a markedly different behavior, characterized by higher peak load, delayed failure onset, and a more gradual post-peak decline. These responses suggest enhanced interfacial bonding strength, which is lacking in the reference sample. The plateau and secondary load-bearing behavior observed in the CNF-modified samples (Fig. 5.10(b)) further confirm enhanced fiber–matrix adhesion. This improved interfacial bonding helps resist delamination and promotes more stable and progressive failure rather than abrupt separation.

Notably, the NC-grafted BFRP composites demonstrate substantial improvements in ILSS compared with the reference sample. Specifically, the ILSS increases from 28 MPa in the reference composite to 50 MPa for the CNC-grafted and 45 MPa for the CNF-grafted BFRPs at an optimal loading of 1.5 wt.% for both NC types. These values correspond to improvements of approximately 79% and 61%, respectively. The ILSS enhancement in the NC-grafted BFRPs is mainly due to three reasons. First, grafting NCs onto BFs increases effective surface area (surface roughness) and mechanical interlocking between fiber and matrix [138]. It effectively enhances the bonding between composite constituents, thereby delaying crack propagation under short-beam bending forces [30,139,140]. Secondly, as evidenced by the XPS results shown in Fig. 5.7, the increased oxygen-based functional groups on the BF surface introduced by the surface modification process facilitate the formation of hydrogen and covalent bonds with the epoxy matrix during the curing process. This enhances molecular contact and interfacial interactions within the composite laminates, thereby improving delamination resistance [141–143]. Lastly, the matrix toughening effect, resulting from the interaction between the resin and NCs, also contributes to the overall improvement, as discussed in Chapter Four.

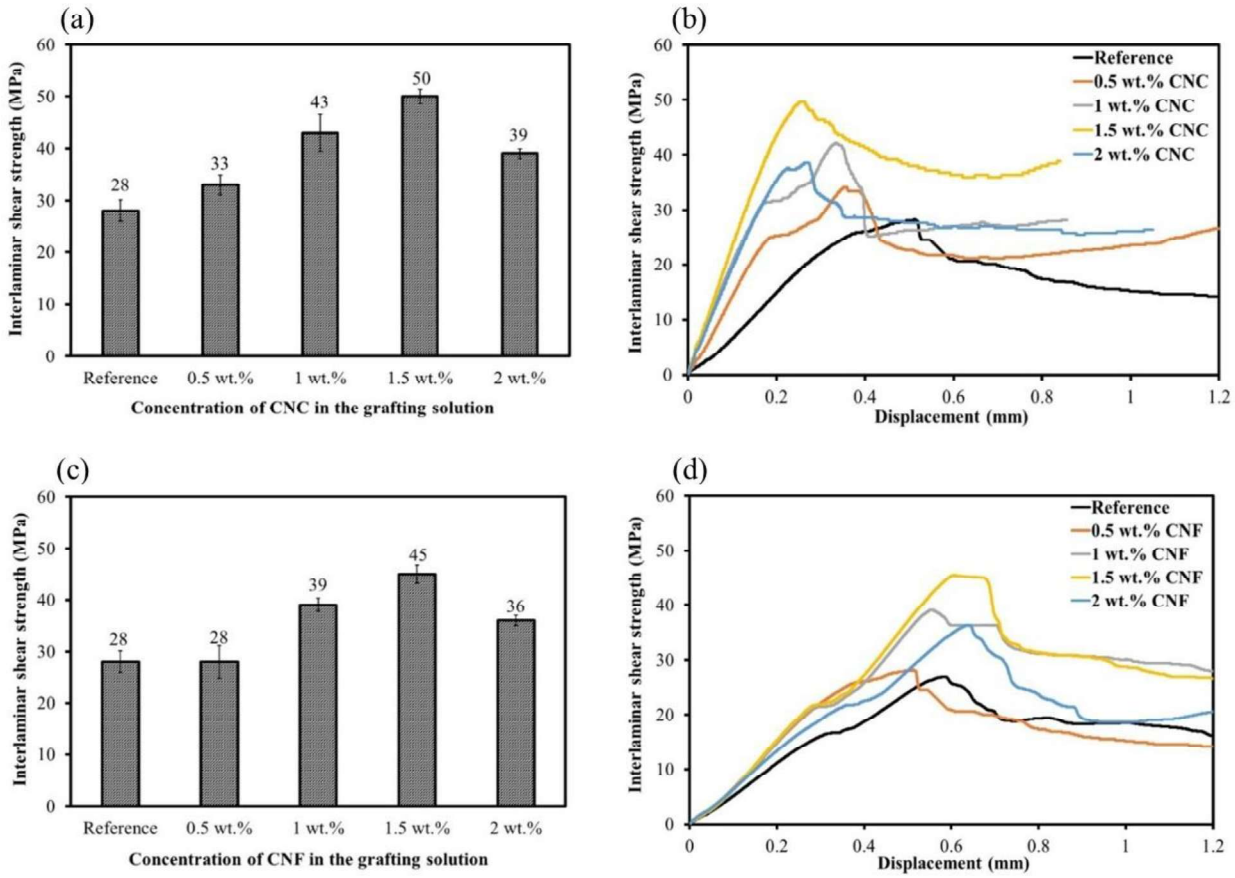

Fig. 5.10. ILSS and Shear stress-displacement curve at different concentrations of NCs in the grafting solution: (a & b) CNC and (c & d) CNF

The ILSS results are highly dependent on the concentration of NCs in the grafting solution. As shown by the SEM images in Fig. 5.11, the roughness of the fractured surface increases, and the BF surface is covered with the matrix by NC grafting. This demonstrates that NC grafting effectively increased the interfacial bonding strength between BF and epoxy resin. At a low concentration of 0.5 wt.%, ILSS performance was not significantly improved by the grafted NCs compared to the reference BFRP. This limited improvement can be attributed to insufficient NC particles on the fiber surfaces, resulting in discontinuities within the composite structure. These lead to nonuniform interface bonding, creating areas with insufficient fiber-matrix coatings, as illustrated in Fig. 5.11(a). Such inconsistencies within the composite structure act as localized

stress concentration zones, significantly reducing the material's resistance to delamination. These stress concentrators facilitate the initiation and propagation of microcracks under mechanical loading, leading to interlaminar fractures and ultimately, premature failure of the composite. The presence of these defects undermines the load transfer efficiency between the fiber and matrix, compromising the overall structural integrity and durability of the BFRP system. For 1.0 wt.% cases, the surface roughness of the fractured surface was largely increased with complicated crack propagation as shown in Fig. 5.11(b), due to relative uniformity in the NC coatings. The uniform distribution of NCs promotes efficient resin impregnation and improves fiber wetting, which significantly enhances the interlaminar bonding strength. In cases of 1.5 wt.%, continuous interfaces with grooves and ridges are formed across the surface, creating a more complex and rough failure surface. This enhanced surface texture facilitates better mechanical interlocking between the fiber and the epoxy matrix, allowing the composite to withstand prolonged delamination propagation and achieve higher ILSS values before failure occurs [144]. The high degree of crystallinity and relatively small size of CNC form strong interfacial interactions with the BF surface, leading to more cohesive bonding between adjacent laminate layers.

As shown in Fig. 5.11(c), the result is a continuous and defect-free interface between the BF and epoxy matrix, with no observable signs of fiber delamination or interfacial separation following mechanical failure. Similarly, CNF, characterized by its long, fibrous morphology and entangled network structure, enhances mechanical interlocking at the fiber–matrix boundary. This structure effectively hinders crack initiation and suppresses crack propagation under applied stress. The improved resistance to crack growth contributes significantly to the enhanced interlaminar shear strength (ILSS) observed in the CNF-grafted BFRPs, underscoring the role of nanocellulose morphology in enhancing interfacial strength [145,146]. However, as the thickness

of the NC grafting layer covering the BF surfaces increases, resin impregnation into the fiber bundles diminishes. As a result, resin-rich areas were formed due to NC agglomeration or clustering, which weakened the interlaminar shear strength, as shown in Fig. 5.11(d) [120,147]. The weakened interface facilitates crack initiation and propagation within the BFRPs, thereby reducing the ILSS values of the CNC- and CNF-grafted BFRPs to 38 MPa and 36 MPa, respectively.

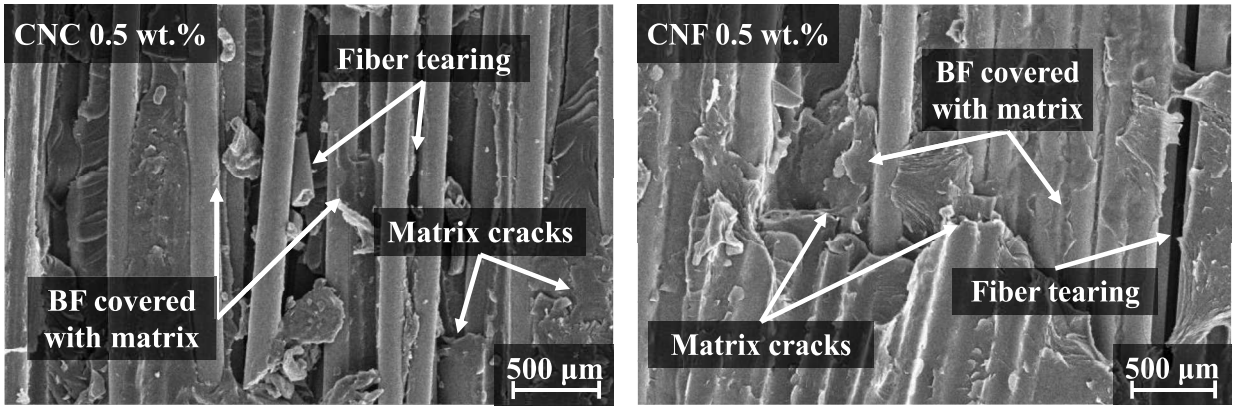

(a)

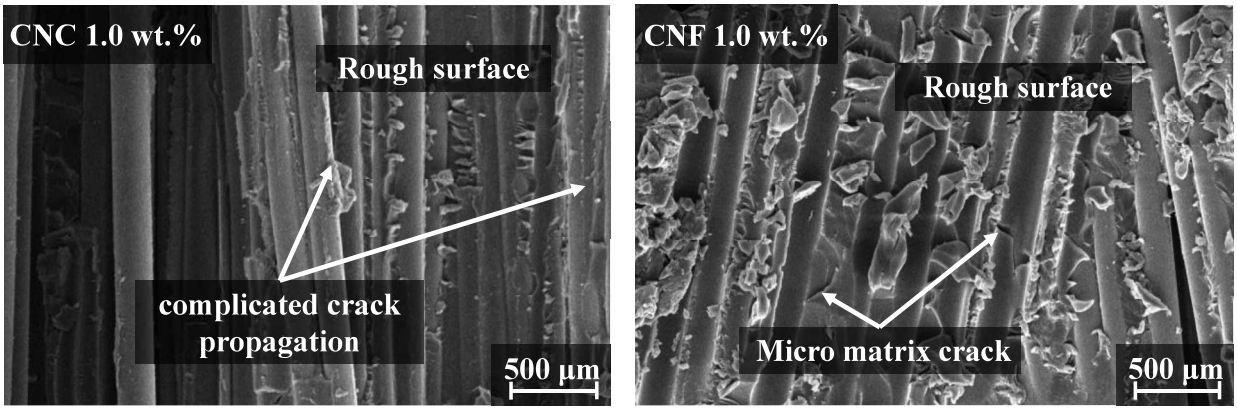

(b)

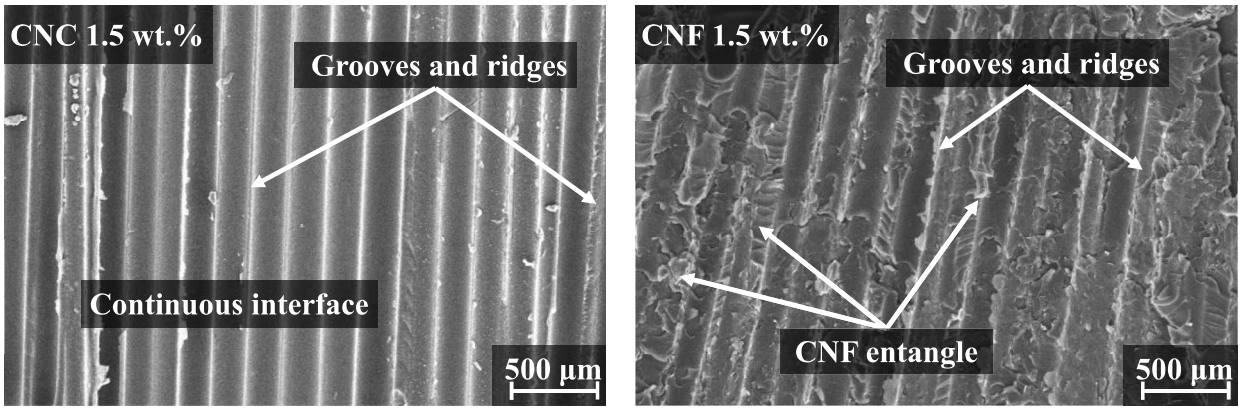

(c)

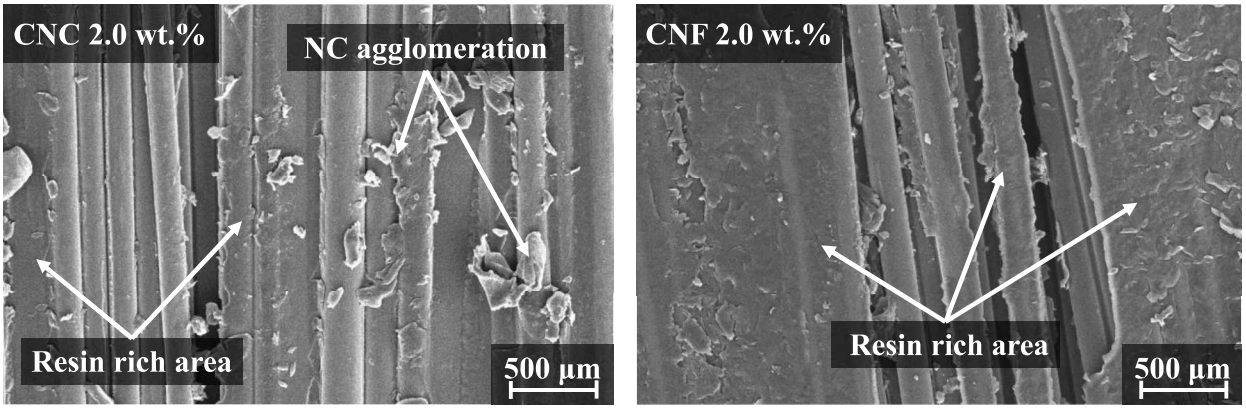

(d)

Fig. 5.11. Microstructural fractured surfaces of BFRP after the ILSS test at different concentrations of NCs in the grafting solution: (a) 0.5 wt.%, (b) 1 wt.%, (c) 1.5 wt.%, and (d) 2 wt.%

5.3.4. Izod Impact Strength

Fig. 5.12 illustrates the Izod impact strength of NC-grafted BFRPs at varying NC concentrations in the grafting solution. The results indicate that grafting NCs onto BF surfaces significantly enhances the impact performance of BFRPs. This improvement can be attributed to the stronger interfacial bonding between the fibers and the epoxy matrix, which facilitates better energy absorption during impact loading. The average impact strength of the CNC-grafted BFRPs increases with the concentration of CNCs in the grafting solution, reaching an optimal value of 205 MPa at 1.5 wt.%, which is a 107% increase compared to the reference. By contrast,

the optimal impact strength of the CNF-grafted BFRP is 172 MPa, achieved at 1 wt.% CNFs, indicating a 74% enhancement in impact performance over the reference sample. To achieve high impact strength and maximize energy absorption in FRPs, it is essential to promote fiber breakage mechanisms that require substantial energy dissipation. However, in practice, delamination often emerges as the dominant mode of failure under impact loading. This interlaminar separation between adjacent plies significantly compromises the structural integrity of the composite. In the reference sample, this delamination behavior is prominently visible on the impact fracture surface, as illustrated in

Fig. 5.13(a), highlighting the lack of effective interfacial bonding. The pronounced delamination under impact force occurs due to the weak interlaminar bonding strength. Therefore, the impact strengths of the BFRPs are closely related to their ILSS [65,148]. The improvement in interlaminar bonding strength enhances energy absorption during delamination while also promoting greater fiber breakage, resulting in additional energy dissipation under impact. At the optimal NCs addition, the primary failure modes are dominated by fiber breakage, with minimal evidence of delamination, as shown in Fig. 5.13(b) and (c). This outcome is primarily attributed to the robust mechanical interlocking between the fibers and the epoxy resin, which effectively impedes the propagation of impact energy across the fiber–matrix interface. This mechanism enhances energy absorption through delamination during crack propagation. However, as the concentration of NCs exceeds the optimal level, the failure mode transitions back to delamination, accompanied by a decrease in impact strength. This reduction in performance at higher NC concentrations arises from diminished resin wettability, which limits its ability to infiltrate the densely NC-grafted fibers. The increased thickness of the NC-grafted

layer creates challenges such as uneven resin distribution and void formation, ultimately weakening the interface between the fiber laminate and the epoxy resin [149].

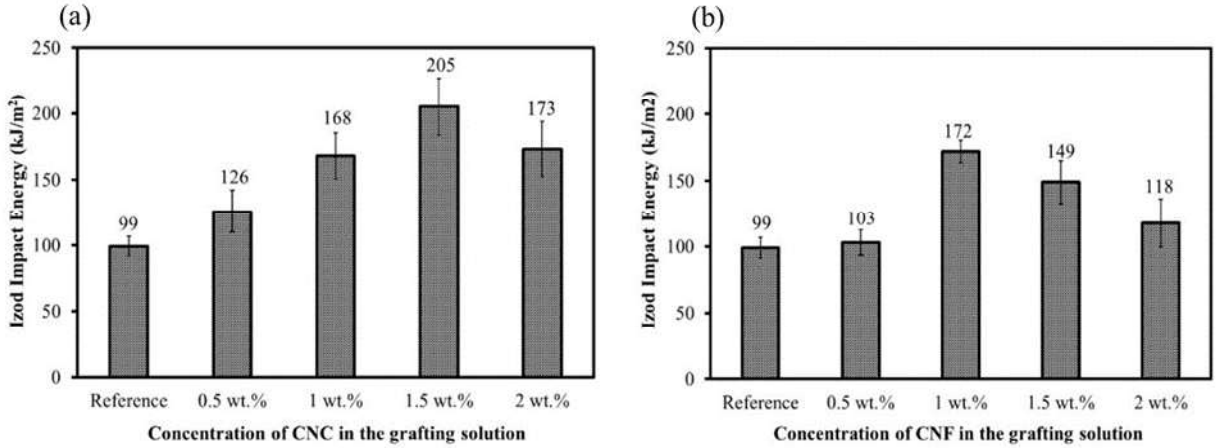

Fig. 5.12. Izod impact strength of BFRPs at different concentrations of NCs in the grafting solution: (a) CNC and (a) CNF

(a)

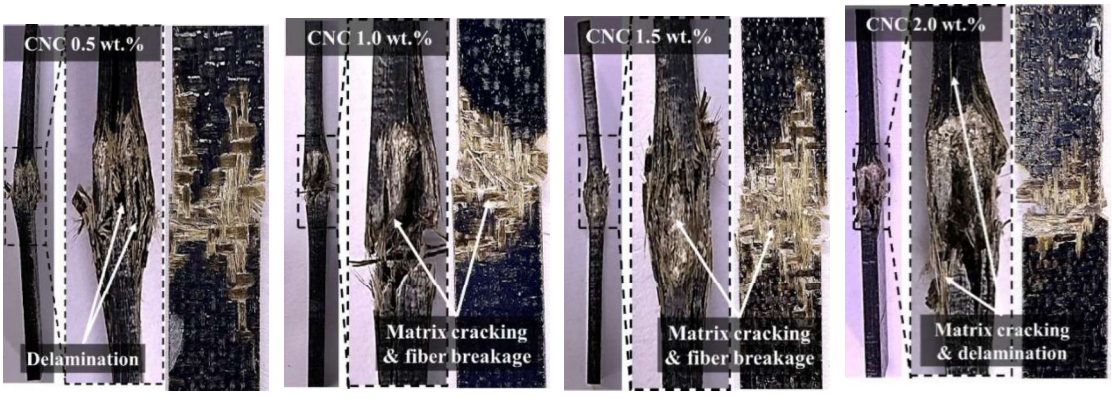

(b)

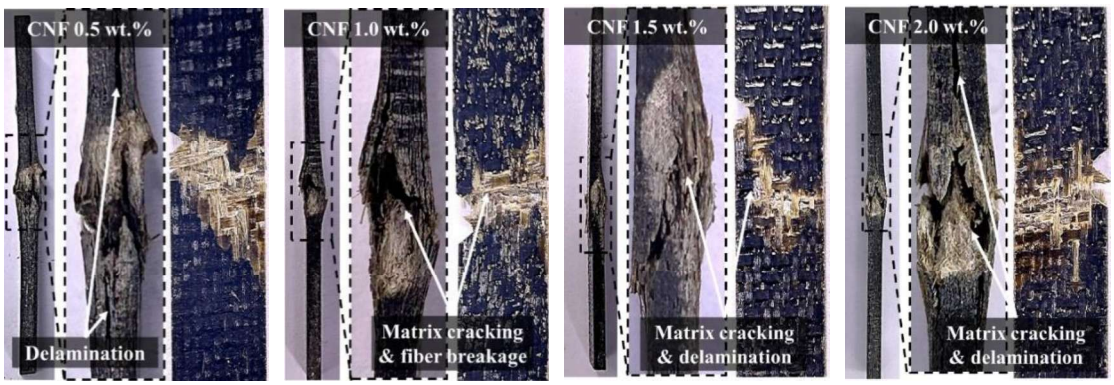

(c)

Fig. 5.12. Impact fractured surfaces of the NC-grafted BFRP at different concentrations: (a) Reference, (b) CNC, and (c) CNF

5.3.5. Moisture Absorption of NC-grafted BFRP

The results of the moisture absorption tests indicated that all the evaluated BFRP composites exhibited a typical diffusion behavior consistent with Fick's law. At the initial stage of exposure, the moisture uptake increased almost linearly with time, signifying a constant rate of diffusion driven by a concentration gradient between the surrounding environment and the dry composite matrix. This linear phase represents the early stage of water ingress, primarily through micro voids and fiber–matrix interface. As the diffusion process progressed, the absorption rate began to decelerate and eventually plateaued, as shown in Fig. 5.13, indicating that the composites had approached their moisture saturation point. Full saturation was observed around 120 h, closely matching the trends reported in previous studies by Pandian et al. [150]. This saturation behavior reflects the equilibrium state where the rate of moisture ingress equals the rate of internal redistribution, highlighting the diffusion-limited nature of water absorption in most polymer composites. The percentage moisture absorptions (M_t) was calculated using Equation (4.4), providing quantitative insights into the diffusion process and its influence on the composite properties.

$$M_t = \frac{W_t - W_o}{W_o} \times 100\% \,, \tag{4.4}$$

where W_t is the weight of the composite specimen at time t after moisture exposure and W_o is the initial dry weight of the composite specimen before moisture exposure.

Grafting NCs onto the BFs significantly enhances the composite's resistance to moisture absorption compared with the reference sample. Among the evaluated composites, the CNC-grafted BFRPs exhibited the lowest moisture absorption, outperforming their CNF-grafted counterparts. In contrast, the reference BFRP sample showed a maximum moisture uptake of 1.2% at saturation. This value significantly decreased to 0.8% and 1.0% for the composites grafted with optimal concentrations of CNC and CNF, respectively. The notable reduction in water absorption is primarily attributed to the improved fiber–matrix interfacial bonding achieved through NCs grafting. The incorporation of NCs creates a more cohesive and tightly packed composite structure by minimizing interfacial voids and microchannels that typically serve as pathways for moisture ingress. This densification effect not only enhances mechanical performance but also imparts superior moisture resistance, making the modified composites more suitable for applications in humid or aqueous environments [151].

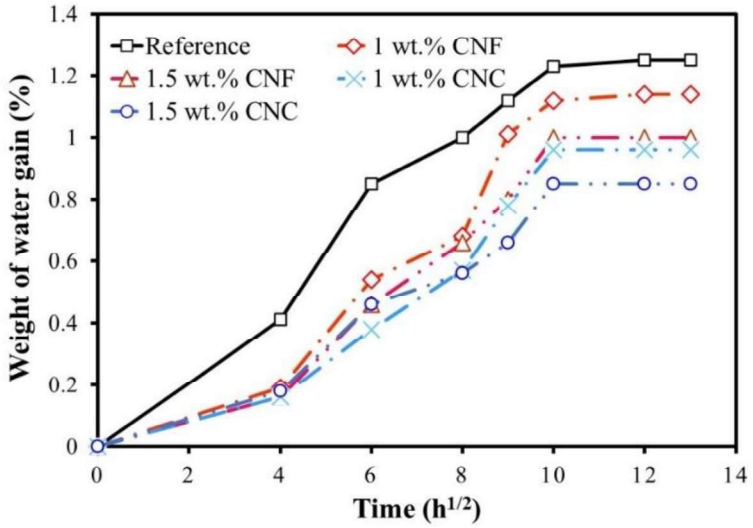

Fig. 5.13. Moisture absorption curves for the optimum NCs-grafted and reference BFRP

The effect of moisture absorption on the mechanical performance of NC-grafted BFRP composites was assessed after prolonged exposure beyond the saturation threshold. As illustrated in Fig. 5.14, the mechanical properties, including tensile strength and stiffness, ILSS, and Izod impact strength, were evaluated for both NC-grafted and reference samples following moisture exposure at 50 °C for 168 h. For all the tested samples, a noticeable decline in mechanical performance was observed when compared with their dry counterparts. Specifically, the tensile strength of the CNF- and CNC-grafted BFRPs decreased by 5.6% and 7.4%, respectively, after moisture conditioning. These reductions indicate that, despite the enhanced interfacial bonding introduced by NC grafting, some degree of moisture-induced degradation still occurs, though to a lesser extent than in the untreated reference composite. In comparison, the reference sample exhibits a higher reduction of approximately 8.9% over the same exposure period as shown in Fig. 5.14(a). As shown in Fig. 5.14(b), the ILSS of the reference sample decreases by 14.3% after exposure to moisture relative to the dry condition. For the composites grafted with 1.5 wt.% CNFs and CNCs, the ILSS decreases by 14.2% and 8.3%, respectively. The Izod impact strength shows the same trend as illustrated in Fig. 5.14(c). The impact strength of the reference sample decreases by 15% relative to that under dry conditions. By contrast, the CNF-grafted BFRP with 1 wt.% CNF concentration shows an 8.7% reduction only. Similarly, the CNC-grafted BFRP experiences a 6.8% reduction in impact strength at 1.5 wt.% compared with that under dry conditions. These reductions in mechanical performance are primarily attributed to the plasticization effect of water on the epoxy matrix, which weakens the bonding strength at the fiber–matrix interface [150]. When FRPs are exposed to moisture, water molecules infiltrate the matrix through the interface, causing it to swell and soften. This softening lowers the threshold for crack initiation, leading to a degradation of the mechanical properties [152]. However, the

strengthened interface resulting from NC modification improves the moisture resistance due to the interfacial sealing effect, which restricts moisture diffusion along the fiber–matrix boundary. It acts as an interfacial nano-bridge that improves wetting and reduces voids. The dominant effect becomes reduced capillary transport rather than the intrinsic hydrophilicity of NC.

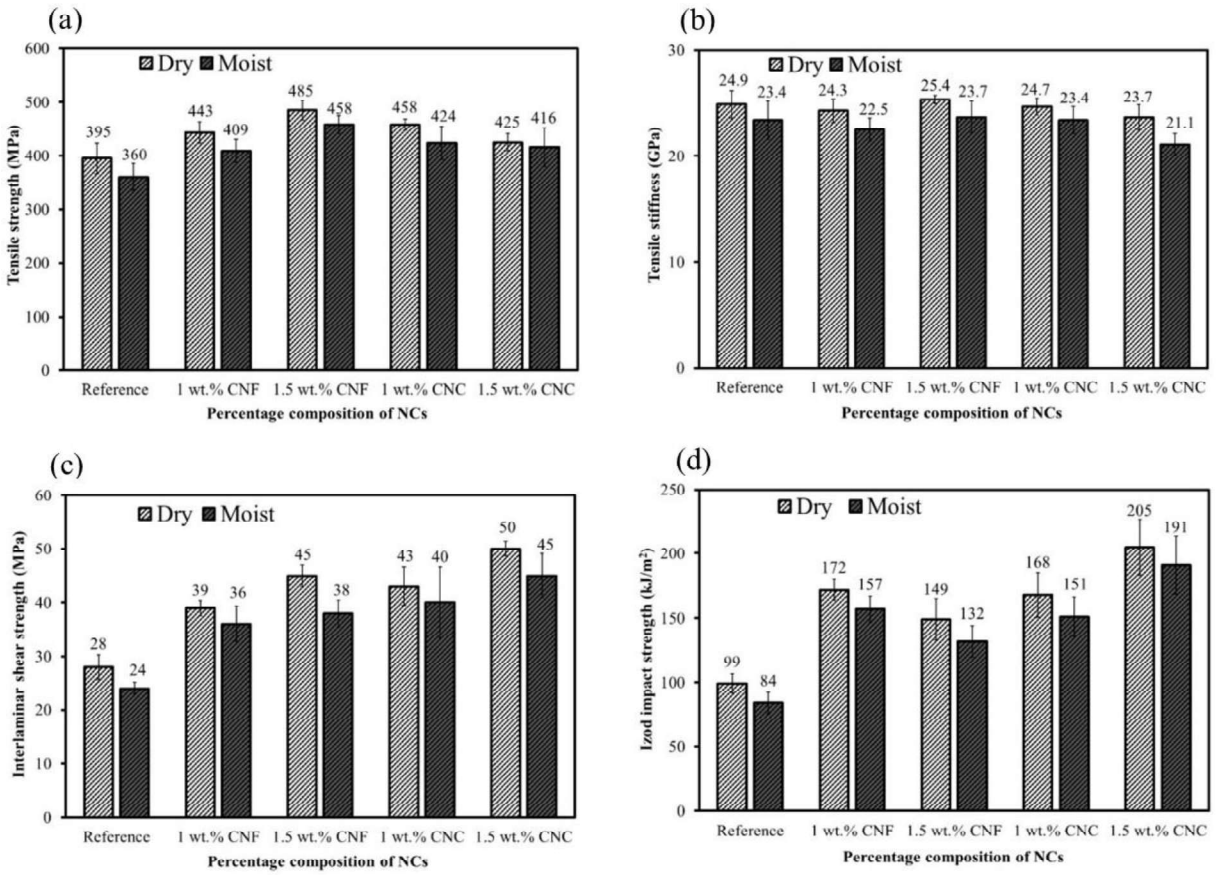

Fig. 5.14. Moisture absorption effects on mechanical properties of NCs-modified BFRP after 168 h at 50 °C: (a) Tensile strength, (b) Stiffness, (c) ILSS, and (d) Izod impact strength

5.3.6. Fracture Toughness of Optimized NC-Grafted BFRP Composite

The Mode I and Mode II fracture toughness of the optimally modified BFRP (grafted with 1.5 wt.% CNC) was evaluated and compared with that of the reference BFRP, as shown in Fig. 5.16(a). The corresponding compliance and compliance coefficient values as calculated from Equation 4.3 are provided in the Appendix (Table A1). For the reference BFRP, the Mode I

fracture toughness was 0.293 kJ/m². In comparison, the 1.5 wt.% CNC-grafted BFRP exhibited a significant enhancement in Mode I fracture toughness, increasing by 75% relative to the reference composite and reaching a value of 0.508 kJ/m². Similarly, both NPC and PC Mode II fracture toughness values showed considerable improvements, increasing from 0.573 and 0.589 kJ/m² for the reference sample to 0.932 and 1.186 kJ/m², respectively. As shown in Fig. 5.16(b), 1.5 wt.% CNC-grafted BFRP shifts the crack propagation mode of the reference BFRP from unstable to stable propagation. This change is likely due to the abrupt crack growth and rapid resistance drops caused by the weak interlaminar bonding strength of the reference BFRP [153]. The limited fracture toughness during PC tests is primarily attributed to the weak interfacial bonding in the reference BFRP, causing erratic crack growth and less energy absorption compared with the CNC-grafted BFRP. CNC-grafted BFRP inhibits crack growth, reflecting its enhanced toughness mechanisms and improved ability to withstand progressive crack propagation based on the bridging effect of the CNC, as shown in Fig. 5.16(c). This occurs because grafted CNC on BF strengthens the mechanical engagement with the epoxy and increases the strain energy required for the crack to propagate along the fiber–matrix interface [154,155]. The Mode I resistance and Mode II force–displacement curves are presented in Fig. 5.17. As shown in the Mode I resistance curve (Fig. 5.17(a)), the 1.5 wt.% CNC-grafted BFRP demonstrates a more gradual slope and sustained crack propagation, indicative of improved crack resistance and energy absorption capabilities. This behavior suggests that the enhanced fiber–matrix interface, resulting from CNC grafting, delays the onset of interfacial debonding and resists crack growth more effectively than in the untreated composite.

In Mode II, the force–displacement curve of the CNC-grafted BFRP for both PC and NPC exhibits a higher peak load and a broader area under the curve compared with the reference (Fig.

5.17(b)). This signifies an increase in shear resistance and improved toughness under sliding failure conditions. The denser and more cohesive interfacial region formed through CNC grafting likely contributes to better load transfer and inhibits fiber pull-out and matrix shear failure, which are typical failure mechanisms in untreated BFRPs. In the reference BFRP, the difference between PC and NPC Mode II results is marginal, whereas the CNC-grafted BFRP results show higher increases in fracture toughness of the PC tests compared to NPC tests [155]. This variation can be linked to the fundamental differences in crack initiation and propagation mechanisms of the two tests. The higher fracture toughness observed in the PC test results, particularly for the CNC-grafted BFRP, is attributed to the activation of additional energy dissipation mechanisms due to the fiber bridging effect, which are more prominent during the propagation phase of the PC test. Specifically, both Mode I and Mode II fracture toughness of the BFRP were significantly enhanced by CNC grafting, with the improvements closely correlating with the observed increases in impact strength and ILSS results.

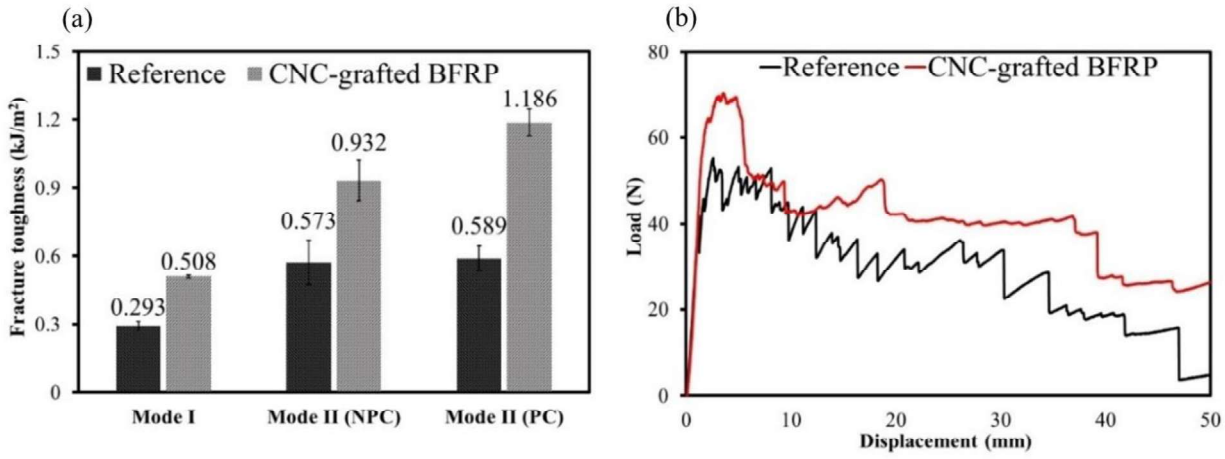

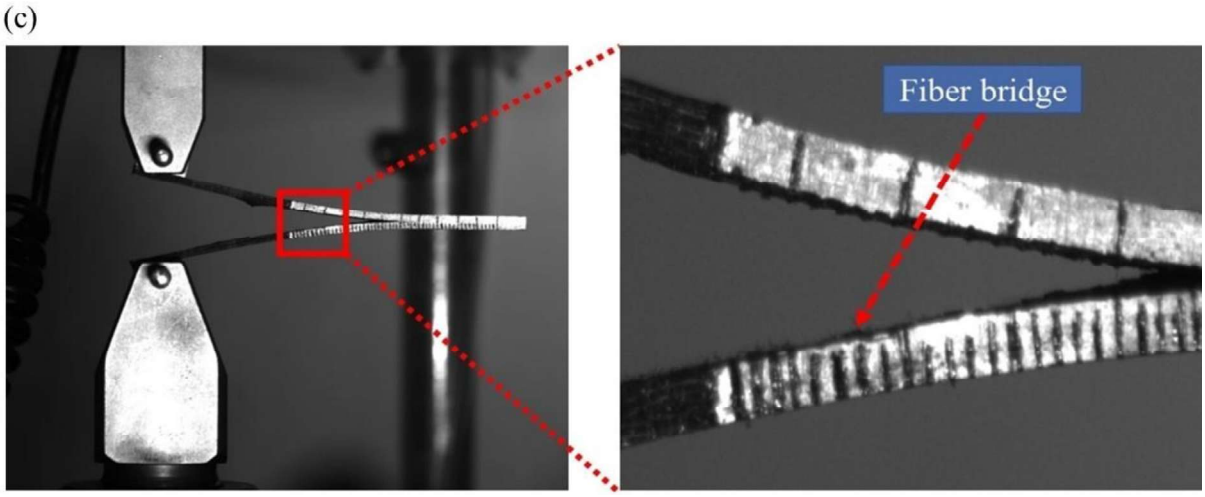

Fig. 5.15. Fracture toughness of BFRP: (a) Mode I and Mode II, (b) Force-displacement curve for Mode I testing, (c) Fiber bridging mechanism in NC-grafted BFRP

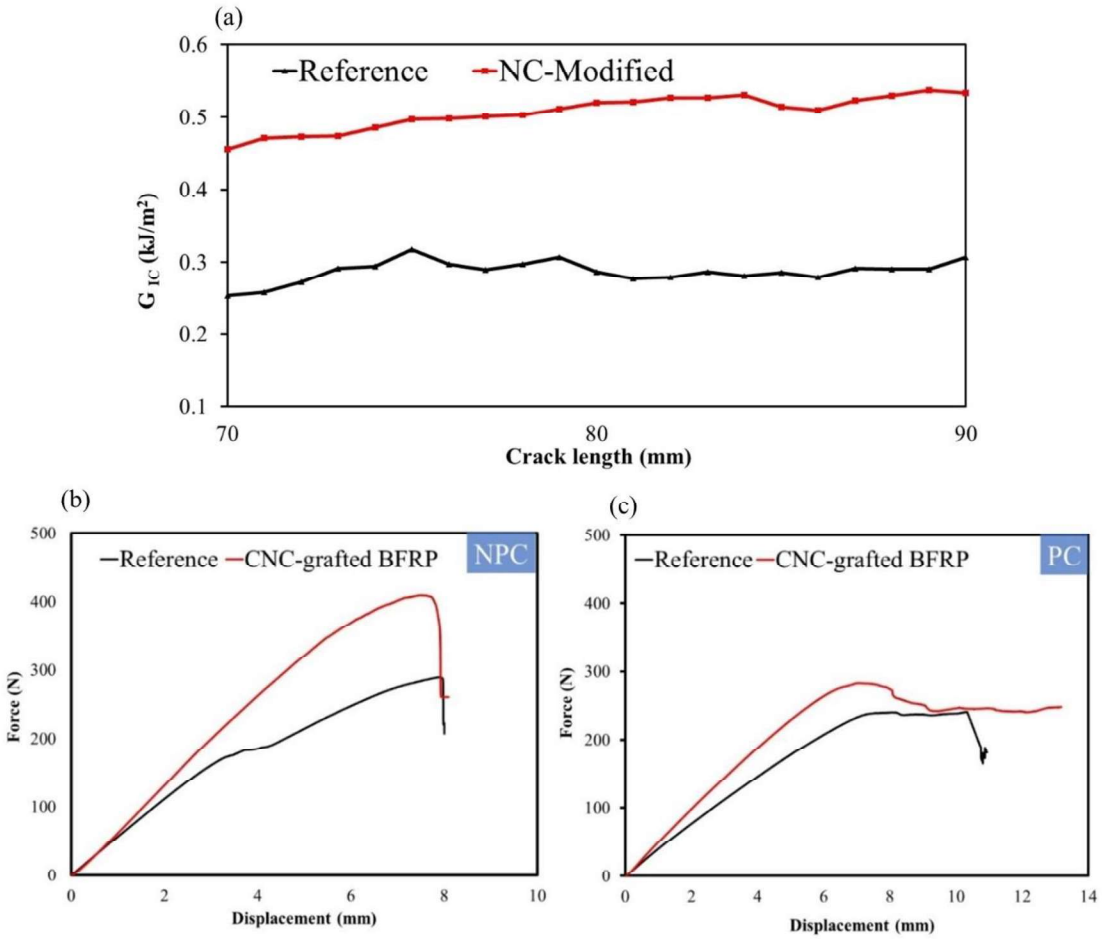

Fig. 5.16. (a) Mode I resistance curve, (b) Mode II force-displacement curves (NPC), and (c) Mode II force-displacement curves (PC)

5.4. Concluding Remark

This study highlights the effectiveness of NC grafting as a strategy to enhance the mechanical performance and durability of BFRP composites. While direct mixing of NCs into the epoxy matrix offered limited improvements due to issues such as nanoparticle agglomeration and increased resin viscosity, the grafting approach proved far more effective. By chemically grafting NCs onto the surface of basalt fibers before composite fabrication, the fiber–matrix interfacial adhesion was significantly improved. XPS confirmed successful surface functionalization, and SEM revealed increased surface roughness, both indicating stronger interfacial interactions. As a result, the NC-grafted BFRPs exhibited notable enhancements in ILSS, impact strength, and fracture toughness without compromising stiffness. In addition, compressive testing was conducted on the optimized 1.5 wt.% CNC-grafted BFRP demonstrated stable load-bearing behavior, with supporting results provided in Appendix (Fig. A1). Moreover, the modified BFRP showed improved moisture resistance and maintained mechanical integrity under humid conditions, further underlining its practical benefits. Overall, the combined mechanical, durability, and sustainability advantages position NC-grafted BFRPs as promising alternatives to conventional fiber composites for demanding structural applications in automotive, aerospace, and related industries.

CHAPTER SIX

6. FINITE ELEMENT MODELING AND EXPERIMENTAL INVESTIGATION OF THE IMPACT BEHAVIOR OF HAT-SHAPED BFRP COMPOSITES

6.1. Introduction

Lightweight structures with superior energy absorption capabilities are essential in modern engineering applications, especially in the automotive, aerospace, and defense industries [156]. Alongside these performance demands, there is a growing emphasis on environmentally sustainable materials that can achieve weight reduction without sacrificing safety or structural integrity in these critical sectors. Since transportation is one of the major contributors to greenhouse gas emissions, improving material efficiency in this sector is essential for reducing environmental impact and addressing climate change [157–160]. FRPs, especially CFRPs, are widely studied and applied in the transportation sector due to their high strength-to-weight ratio, corrosion resistance, and contribution to fuel efficiency [9,96]. In addition, the deformation behavior and energy absorption characteristics of CFRPs under various loading conditions and geometries have been extensively studied, providing valuable insights into their structural performance under complex stress conditions [97–100]. However, producing carbon fiber involves energy-intensive processes that generate substantial carbon emissions, resulting in high environmental impacts and costs. As a result, there is a growing interest in developing more environmentally friendly composite materials as alternatives to conventional FRPs in the automotive industry. Basalt fibers (BFs), derived from abundant natural basalt rock, have gained significant recognition for their excellent mechanical properties, high thermal stability, shorter processing cycles, and recyclability compared with carbon and glass fibers [161,162].

The production of BFs involves a significantly lower carbon footprint compared to conventional synthetic fibers, making them a more suitable alternative for addressing environmental challenges in the automotive sector. Beyond sustainability, BFs also offer favorable mechanical properties, positioning them as promising candidates for structural applications in vehicles[20,26]. Among these applications, vehicle crashworthiness is particularly critical. It is a key aspect of automotive design that focuses on occupant safety, aiming to manage and dissipate impact energy during a collision to minimize injury. In the event of a crash, a well-engineered vehicle structure must effectively absorb and dissipate impact energy, thereby reducing the force transmitted to occupants and enhancing passenger safety [163]. However, achieving high crashworthiness must be balanced with the broader goals of reducing vehicle weight, improving performance, and environmental sustainability. In this context, BFRPs are receiving increasing attention due to their high specific strength, low weight, and reduced environmental impact, making them promising candidates for use in lightweight and crashworthy automotive structures [164,165]. One key limitation to the broader application of BFRP composites is the relatively poor interfacial bonding between BFs and polymer resins, which has been shown to reduce interlaminar strength and adversely affect overall composite performance [26,53,166]. Although a considerable number of studies have been dedicated to enhancing the interfacial bonding of BFRP composites, mainly through fiber surface treatments and matrix modifications [53,167], their structural performance remains largely underexplored. Most existing studies emphasize material-level enhancements, such as tensile strength or interfacial shear strength, but do not extend their analysis to structural-scale behaviors relevant to engineering applications. In particular, there remains a significant gap in understanding how BFRP composites perform under dynamic impact and crash-like scenarios, especially when used

in complex geometries similar to real-world components. This gap highlights the need for further investigation to validate the suitability of BFRP composites for load-bearing and energy-absorbing applications in industry, such as the transportation sector.

In this study, the energy absorption capacity and crashworthiness of a hat-shaped BFRP composite were investigated. The study evaluates its effectiveness in mitigating impact forces during crash events. Hat-shaped geometries are widely used in vehicle body components designed for energy absorption, due to their efficient load distribution and structural stability under impact conditions [100,103,168–170]. However, they are prone to internal delamination under complex shear and bending stresses, an inherent limitation of BFRPs, which can significantly compromise their impact performance. This chapter, therefore, evaluates and compares the delamination behavior and energy absorption capabilities of unmodified and CNC surface-treated hat-shaped BFRP composites under dynamic impact loading conditions. The CZM approach was implemented in Abaqus, in parallel with experimental drop-weight impact tests to effectively capture the interlaminar damage mechanisms. The modeling approach includes detailed representations of geometry, material properties (including both NC-modified and unmodified systems), meshing strategies, contact interactions, and boundary conditions necessary for simulating dynamic impact events. Three span lengths (80 mm, 140 mm, and 200 mm) were selected to examine how span-dependent stress distributions influence failure modes, resulting in six distinct test cases. These cases are summarized in Table 6.1 and will be referenced throughout the subsequent Sections. By testing across different spans, we aimed to capture the transition in failure behavior and energy absorption characteristics, which is essential for optimizing composite design based on specific application requirements. This approach ensures a more comprehensive understanding of how the structure performs under varying

support conditions, aiding in the design of impact-resistant components tailored for different structural applications. Longer spans promoted bending-dominated failure due to greater structural flexibility, while the shorter span primarily induced shear-driven delamination, making it particularly effective for assessing and comparing the interfacial bonding strength between unmodified and CNC surface-treated BFRP composites. The intermediate span (140 mm) exhibited transitional behavior, characterized by a mixed failure mode involving both shear and bending mechanisms. Numerical simulations showed strong agreement with experimental results for both modified and unmodified composites across all span lengths, validating the modeling approach and the reliability of the findings.

Table 6.1. Test cases for both CNC-modified and unmodified BFRP at various span lengths

Study cases	**Composite type**	**Span length (mm)**
Ref-80	Unmodified	80
Ref-140	Unmodified	140
Ref-200	Unmodified	200
CNC-80	CNC-modified	80
CNC-140	CNC-modified	140
CNC-200	CNC-modified	200

6.2. Materials and Methods

6.2.1. Materials

The materials used for the fabrication of the hat-shaped BFRP composite structures included the optimized NC-grafted BFRP laminates, stainless-steel molds, and appropriate release agents. To ensure consistency in the experimental data, all material specifications remained the same as those detailed in earlier Chapters.

6.3. Finite Element Modeling

The dynamic response of FRP composites under impact loading is inherently complex, owing to their heterogeneous structure, anisotropic mechanical properties, and the critical influence of fiber–matrix interfacial interactions. These complexities become more pronounced under high strain-rate conditions, where multiple failure mechanisms such as matrix cracking, fiber breakage, interply delamination, and fiber–matrix debonding can occur simultaneously. To better understand and quantify these phenomena, a FEA model was developed in Abaqus/Explicit, incorporating experimentally derived material parameters and boundary conditions obtained from drop-weight impact testing. The simulation aimed to investigate the influence of NC surface modification of BFs on the structural response of the BFRP composites, particularly in terms of energy dissipation, delamination resistance, and progressive failure mechanisms. To accurately capture interfacial damage evolution, a CZM was integrated into the FEA framework to simulate delamination initiation and propagation between lamina interfaces. To manage the computational cost associated with the fine meshing of cohesive elements (CEs), the composite layup was divided into four sub-laminates, each 0.75 mm thick and consisting of six plies of 0.125 mm thickness. Three near-zero-thickness (0.01 mm) CEs were strategically inserted at the upper, middle, and bottom interfaces of the sub-laminates to represent potential delamination zones. The model successfully reproduced key aspects of the experimental impact behavior, including the load–displacement response and progressive crushing of the optimized hat-shaped NC-grafted BFRP structure. This numerical simulation further enabled visualization of internal damage evolution, such as delamination, interlaminar cracking, and crack propagation in real time.

6.3.1. Geometry Definition

The geometry of the hat-shaped BFRP component was modeled to reflect the actual fabricated specimen dimensions. Key features included flange width, wall height, corner radius, and overall profile length as illustrated in Fig. 6.1. The model was constructed as a 3D solid structure to capture local deformation effects under impact. Symmetry was not applied to preserve the full-field response of the structure.

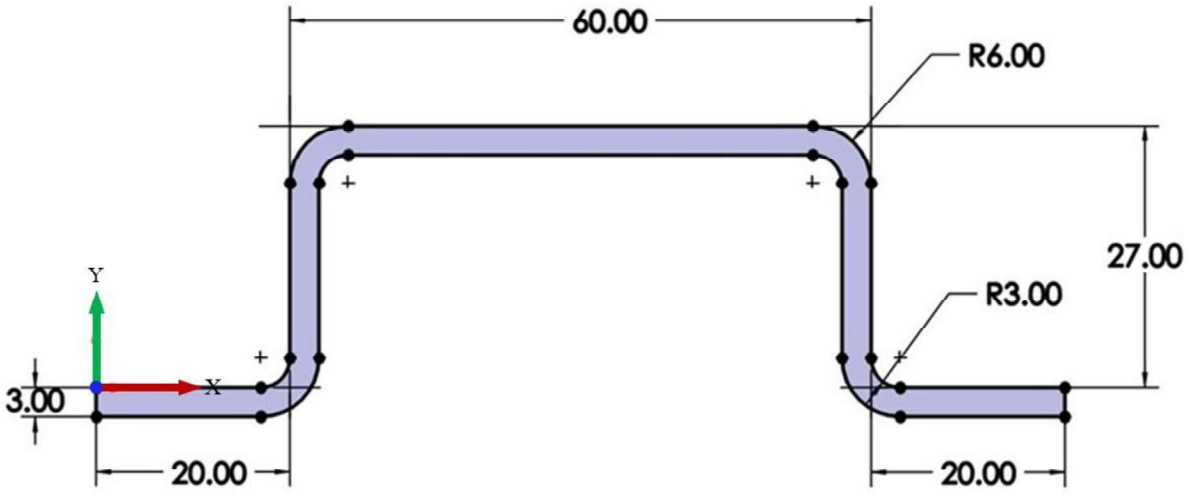

Fig. 6.1. Specimen geometry for the hat-shaped profile

6.3.2. Material Property Assignment

The mechanical properties of the BFRP composite used in the FEA model, including elastic properties, damage parameters, and CZM interfacial properties, are summarized in Table 6.2 [92]. The CZM parameters were obtained as described in Chapter Two (Section 2.11). As presented in Table 6.2, the in-plane and out-of-plane shear moduli (G_{12} and G_{13}) were adopted from the work of Zhou et al. [171], as approximate values for both unmodified and CNC-modified BFRP. Although the study primarily investigates the ballistic impact behavior of carbon–basalt hybrid composites, the elastic properties of CFRP and BFRP are reported

separately. Accordingly, the present work exclusively adopts the shear moduli corresponding to the BFRP material. The exponent η in the B–K law depends on the material system and loading conditions [113]. Accordingly, a value of η =1.5 was selected in the present work after conducting a confirmation study over the range of $1.2 \leq \eta \leq 2.0$. The value η =1.5 provided the best agreement with the experimental load–displacement response and damage evolution, while yielding an appropriate mixed-mode fracture response. Hashin failure criteria were incorporated to simulate the onset of damage and progressive degradation under impact. This material definition approach allowed for an accurate representation of the mechanical behavior of both composite systems under impact loading, thereby enabling a comparative evaluation of the effect of NC modification on the structural performance and energy dissipation mechanisms of the hat-shaped BFRP components.

The observed similarity in mechanical properties along the longitudinal and transverse directions can be attributed to the symmetric architecture of the twill weave, in which fibers are oriented equivalently in both the warp and weft directions [114]. This balanced fiber distribution enables the composite to exhibit nearly isotropic in-plane behavior, minimizing directional dependency and promoting uniform stress distribution under loading. This property was strategically utilized in defining the composite stacking sequence, as illustrated in Fig. 6.2, which presents the layup configuration and fiber orientation visualization for the hat-shaped BFRP component modeled using twill-woven basalt fabric. The left panel shows the layup applied to continuum shell elements, selected for their ability to capture through-thickness effects while maintaining computational efficiency. Given the nature of the twill-woven fabric, all plies were assigned a uniform fiber orientation angle of 0°, eliminating the need for alternating ply angles as required in unidirectional laminates. The layup orientation was defined using surface as the

normal axis and edge as the primary axis, ensuring consistent ply alignment along the curved geometry. Additionally, three integration points were specified through the thickness to accurately resolve stress gradients and potential interlaminar effects such as delamination. The right-hand panel in Fig. 6.2 shows the uniform fiber alignment throughout the structure. White arrows indicate the fiber directions, while colored vectors represent the stacking direction. Notably, this uniform orientation is preserved even in the curved sections, demonstrating the geometric adaptability of twill-woven fabrics without requiring ply rotation or angle adjustment.

Table 6.2. Input material properties for the FE model

Category	Properties	Unmodified	NC-modified
Elastic property	Density (g/cm^3), ρ	2	2.15
	Young's moduli (GPa), $E_1 = E_2$	25	26
	In-plane shear modulus (GPa), G_{12}	2.2*	2.2*
	Out-of-plane shear modulus (GPa), $G_{13} = G_{23}$	2*	2*
	Poisson's ratio in plane 1-2, ν_{12}	0.19	0.22
Damage property	Ultimate tensile strength (MPa), $\sigma_L = \sigma_T$	395	480
	Ultimate compressive strength (MPa), $\sigma_{CL} = \sigma_{CT}$	200	250
	Shear strength, τ	26	50
	Tensile fracture energy (N/mm), $G_{XT} = G_{YT}$	22	40
	Compressive fracture energy $G_{XC} = G_{YC}$	20	35
Interfacial property (CZM)	Nominal stresses (MPa), $t_{nn} = t_{ss} = t_{tt}$	26	50
	Fracture toughness in mode I, G_{IC} (kJ/m^2)	0.293	0.508
	Fracture toughness in mode II, G_{IIC} (kJ/m^2)	0.589	1.186
	Penalty stiffness Knn = Kss = Ktt	3e5	5e5
	Benzeggagh–Kenane (B–K) (η)	1.5	1.5

Note: (*) [171]

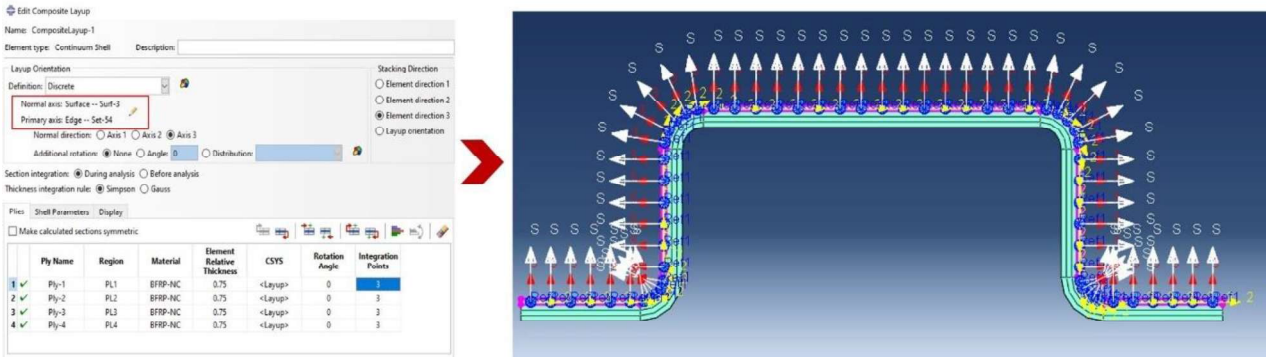

Fig. 6.2. Composite layup definition and fiber orientation for twill-woven BFRP hat-shaped component

6.3.3. Meshing

A structured meshing approach was adopted to ensure mesh consistency and better capture the geometry and stress distribution. The hat-shaped BFRP component was modeled using continuum shell elements to effectively represent the through-thickness stress variations and bending behavior of the composite structure. This approach combines the geometric advantages of shell modeling with the three-dimensional stress resolution of solid elements, making it particularly suitable for thin-walled composite structures under dynamic loading conditions. A matched mesh was maintained between the cohesive and composite elements, enabling node-to-node connectivity at their interfaces, as illustrated in Fig. 6.3. A mesh convergence study was conducted using three global mesh densities (coarse: 4 mm, medium: 3 mm, and fine: 2 mm) for the shortest span length (80 mm), which exhibits the highest stress gradients and therefore serves as the critical case for the numerical models considered in this study. Mesh convergence was quantitatively assessed based on the peak impact force and total energy dissipation. As presented in Table A2 of the appendix, the predicted peak force for the medium and fine meshes differed by less than 2%, while the variation in total energy absorption was less than 1% for both the reference and CNC-modified BFRP models. In contrast, the coarse mesh overpredicted the peak

force by approximately 3% relative to the fine mesh due to increased numerical stiffness and insufficient resolution of local deformation and damage evolution. Since the improvement from the medium to the fine mesh was marginal, while the computational cost of the fine mesh increased significantly (approximately doubling the simulation time), the medium mesh was selected for all subsequent simulations, as it provides an optimal balance between computational efficiency and numerical accuracy. A more refined mesh was applied to curvature regions of the hat-section to accurately capture the complex stress distributions and localized damage initiation, as illustrated in Fig. 6.4. The final models, with lengths of 120 mm, 180 mm, and 240 mm, consisted of approximately 16,800, 25,200, and 33,600 elements, respectively, for the adopted mesh size. An average element size of 1.5 mm was used in those critical regions, while a coarser mesh was applied in less sensitive areas to reduce computational time and cost. Hexahedral elements with reduced integration (SC8R) were employed for the composite laminates due to their effectiveness in representing through-thickness behavior, while cohesive elements (COH3D8) were implemented at the ply interfaces to capture the interlaminar delamination.

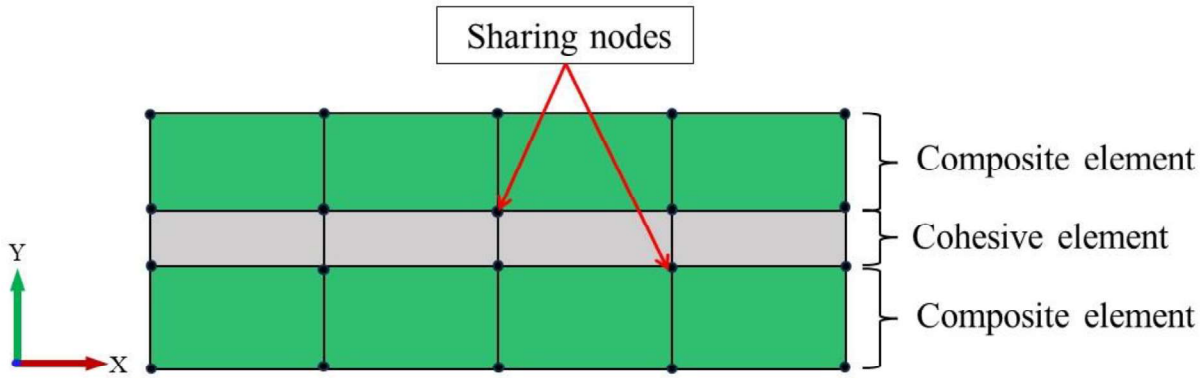

Fig. 6.3. Meshing style between the composite and cohesive element

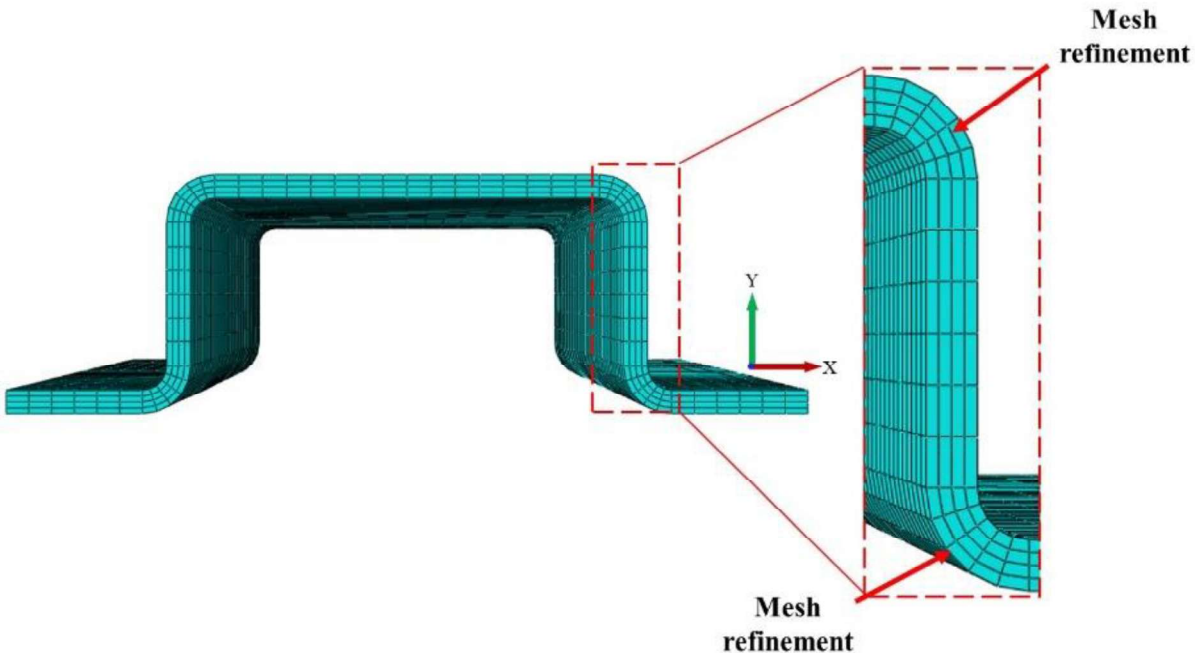

Fig. 6.4. Mesh refinement at the curvature

6.3.4. Contact Interaction

A general contact algorithm was employed to simulate the interactions between the impactor, the BFRP specimen, and the supporting fixtures during the impact event. The contact behavior was governed by a penalty-based formulation, with a friction coefficient of 0.2, which represents tangential resistance. In the normal direction, a hard contact condition was applied to prevent penetration and ensure realistic impact force transmission. This contact setup allowed accurate simulation of contact force development and sliding behavior during the impact event. Self-contact within the composite was disabled to reduce computational cost and time, as significant folding or wrinkling was not expected.

6.3.5. Boundary Conditions

To replicate the experimental conditions of the simply supported drop-weight impact test, the FE model was configured to match the physical setup as closely as possible. Two supports were positioned 20 mm from each edge of the composite specimen and fully constrained to

simulate simple supports, allowing vertical reaction forces while preventing rigid body motion (see Fig. 6.5). The specimen was secured using a C-clamp, which was modeled as a rigid body in the simulation with a radius corresponding to the actual experimental clamp. A uniform surface pressure was applied to the clamp region to accurately replicate the load transfer and restraint conditions during impact. The impactor was modeled as a rigid cylindrical body with a diameter of 25 mm, matching the experimental configuration. It was assigned an inertial mass of 24 kg and an initial velocity of 5425 mm/s, consistent with the energy input derived from the experimental drop height. These parameters were applied via a reference point rigidly coupled to the impactor, ensuring accurate control of motion and force transmission. The movement of the impactor was constrained strictly along the Y-axis, eliminating displacement or rotation in other directions to maintain realistic impact behavior, as illustrated in Fig. 6.5.

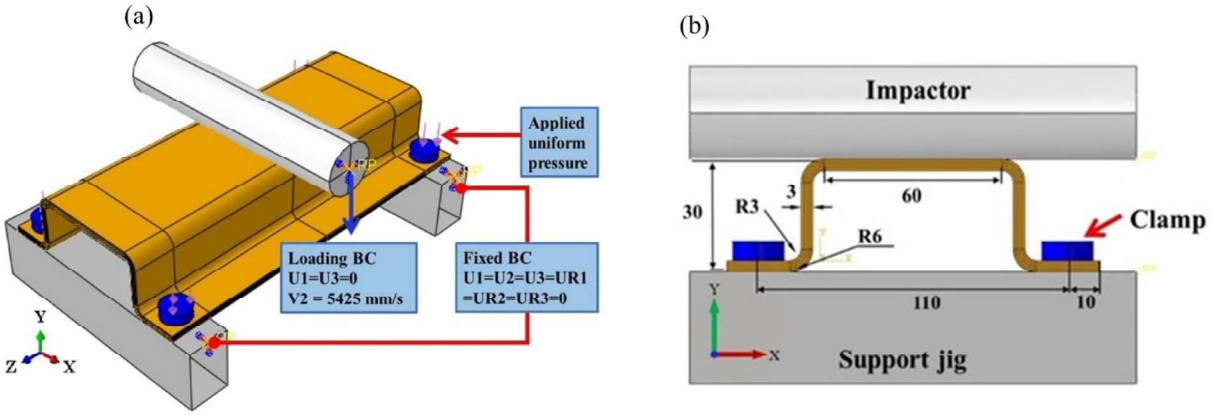

Fig. 6.5. FEA Model: (a) Loading condition, (b) Specimen geometry

6.4. Experimental Investigation

6.4.1. Fabrication of Hat-Shaped BFRP

The composites were fabricated using the hand lay-up method. The BF fabrics were manually impregnated with the epoxy-hardener mixture layer by layer, using a roller to ensure

full wetting and eliminate entrapped air. A total of 24 layers of twill-woven BF fabrics were stacked into custom-designed steel molds to fabricate the hat-shaped BFRP composite, resulting in an average thickness of approximately 3 mm and a fiber volume fraction of around 60%. The complete fabrication sequence of the specimen is illustrated in Fig. 6.6, while additional details of the mold design used for shaping the hat-shaped BFRP composite are provided in the Appendix (Fig. A2). The steel mold, made from SS304 stainless steel, was specifically designed and manufactured to match the geometry and cross-sectional profile of the composite component for accurate shaping during the curing process. After lay-up, the stacked laminate was covered with a peel ply, breather fabric, and vacuum bagging film. This was followed by autoclave curing under a controlled pressure of 7 bar and a temperature profile reaching 125 °C for 3 h, while maintaining the initial vacuum of 760 mm/Hg, to ensure a complete curing process. The cured composites were demolded and cut to the required specimen dimensions, using a water jet cutting machine (T500-3015, Tops Co. Ltd., Republic of Korea) at a speed of 650 mm/min.

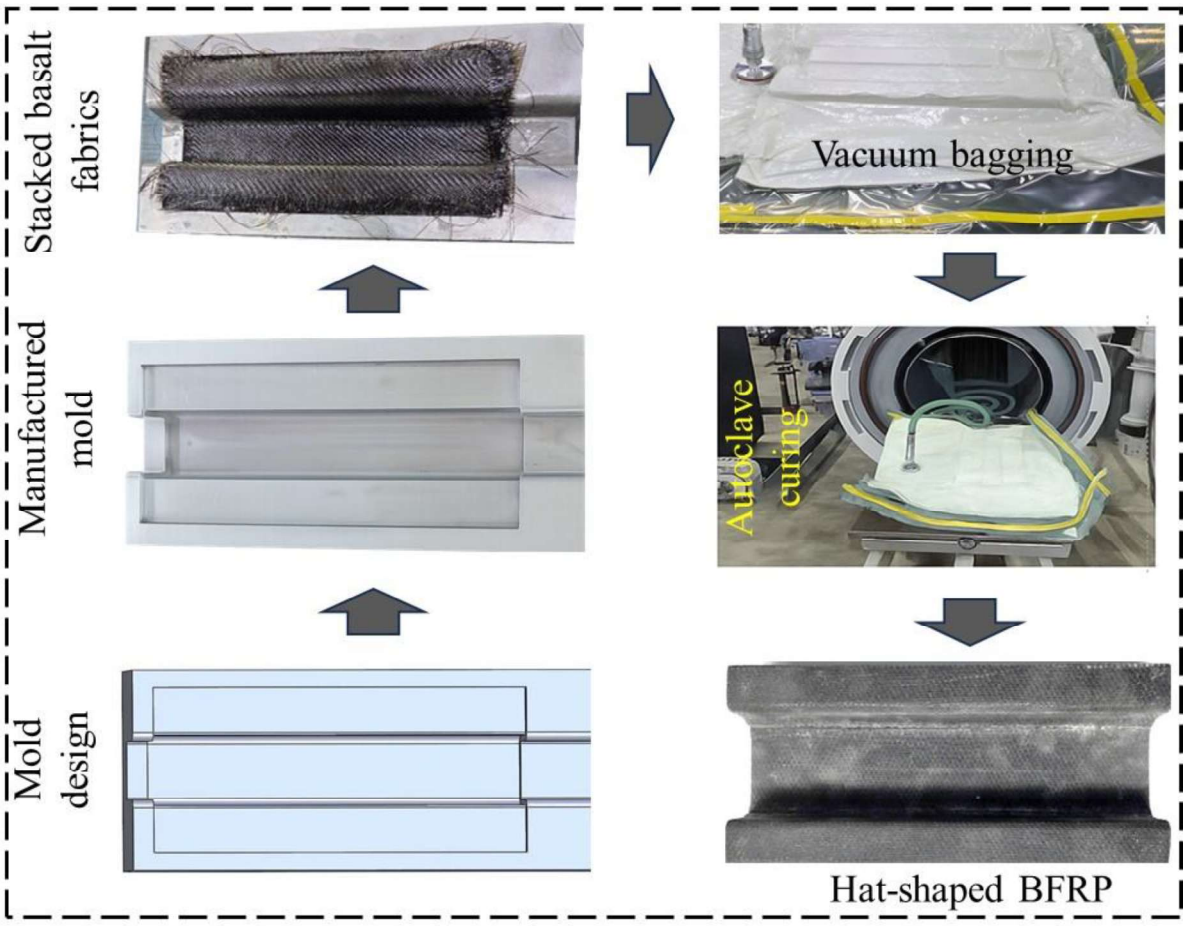

Fig. 6.6. Fabrication process of hat-shaped BFRP composite

6.4.2. Dynamic Impact Test

The dynamic impact test was conducted on the hat-shaped BFRP specimens using a drop tower testing machine, as shown in Fig. 6.7. Additional details of the impact testing setup and specimen dimensions are provided in Appendix (Fig. A3). To ensure proper boundary conditions and test repeatability, the four corners of each specimen were securely fixed to a custom-designed three-point bending jig. This setup effectively restricted lateral displacement and rotation during impact, allowing for controlled deformation and accurate assessment of structural response. A 24 kg impactor, equipped with a 25 mm diameter cylindrical bar, was dropped from a specified height to achieve the desired impact energy. The crushing force was measured

directly by the load sensor integrated into the impact machine. This sensor enabled real-time measurement of the dynamic force transmitted through the specimen. Additionally, the vertical displacement of the impactor was recorded using a laser-based displacement sensor, which offered high spatial and temporal resolution. This sensor was interfaced with a high-sensitivity digital oscilloscope as shown in Fig. 6.7, which provided synchronized, real-time data acquisition of the displacement signals with millisecond-level sampling accuracy.

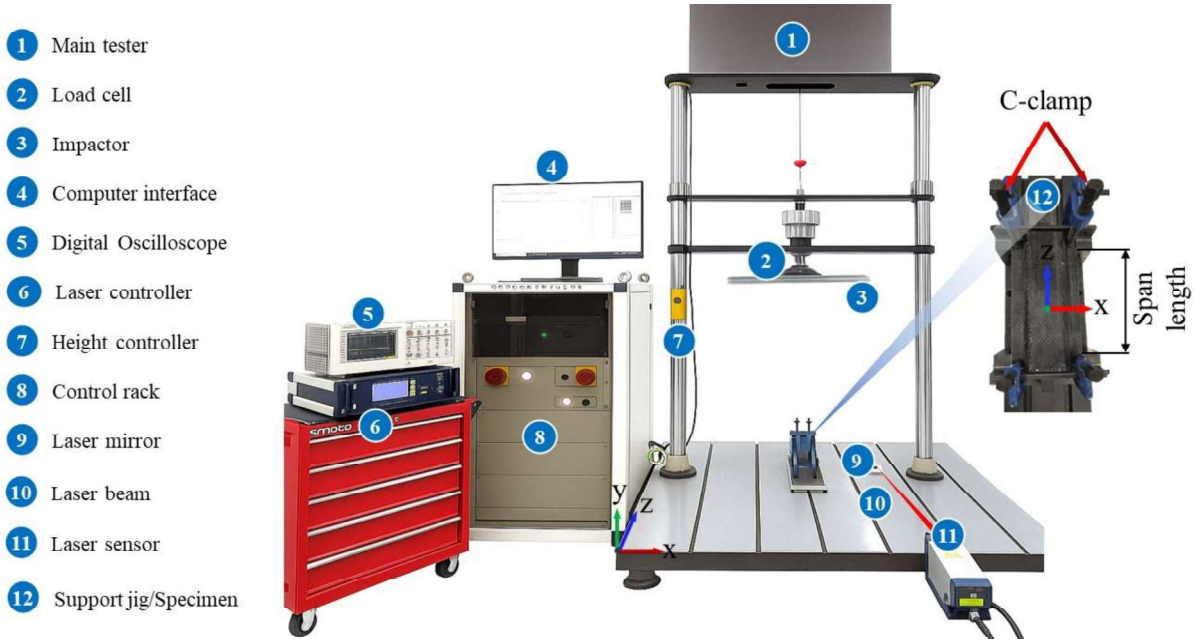

Fig. 6.7. Schematic arrangement of the experimental setup for dynamic impact testing of hat-shaped BFRP composite

Key performance indicators, including the force–displacement responses, energy absorption (EA), peak force (PF), and specific energy absorption (SEA), were evaluated for both CNC-modified and unmodified specimens across three span lengths. The EA and SEA values were calculated from the force–displacement curves using Equations. (6.1) and (6.2), respectively. For each test condition, three experimental trials were conducted, and the average

values were compared with the corresponding numerical simulation results to validate model accuracy and assess the influence of surface modification.

$$EA = \int_0^d F.\ d(x) \tag{6.1}$$

$$SEA = \frac{EA}{m} \tag{6.2}$$

Where EA is the total energy absorbed by the structure during the crushing process, F is the loading force, d is the maximum crushing deflection, and m is the mass of the specimen. SEA represents the specific energy absorption, a performance indicator used to evaluate the energy absorption efficiency of a structure relative to its weight [172,173].

6.5. Results and Discussion

This section presents key observations from both experimental and numerical analyses of the hat-shaped BFRP specimens. The results include force–displacement responses, EA, PF, and SEA for three different span lengths, evaluated for both the reference and NC-modified BFRP.

6.5.1. Surface Morphology

To investigate the surface morphology and its impact on the composite performance, scanning electron microscopy (SEM) was conducted on pristine BF, as well as those subjected to flame treatment, silane coating, and CNC grafting. This sequential surface modification approach was characterized to assess the morphological transformations at the fiber level and validate the effectiveness of each treatment stage. As shown in Fig. 6.8(a), the untreated BF exhibits a smooth surface with minor surface contaminants, indicating low surface energy and poor affinity with the resin. This results in weak fiber–matrix interfacial bonding, making the composite vulnerable to interfacial delamination, particularly under dynamic or shear-dominant loading conditions. After flame treatment, Fig. 6.8(b) reveals that the fiber surfaces remain largely

smooth but exhibit variation in the surface texture, likely due to localized oxidation and thermal etching. In addition, surface contaminants present in the untreated fibers are completely removed, enhancing the surface reactivity and providing a suitable foundation for subsequent functionalization. Fig. 6.8(c) shows the silane-coated BF with visible thin film-like deposits, likely attributed to silane condensation and the formation of siloxane (–Si–O–Si–) networks. These contribute to improved chemical bonding sites. Most significantly, Fig. 6.8(d) demonstrates that CNC-grafted fibers exhibit a rougher and more uniform surface morphology.

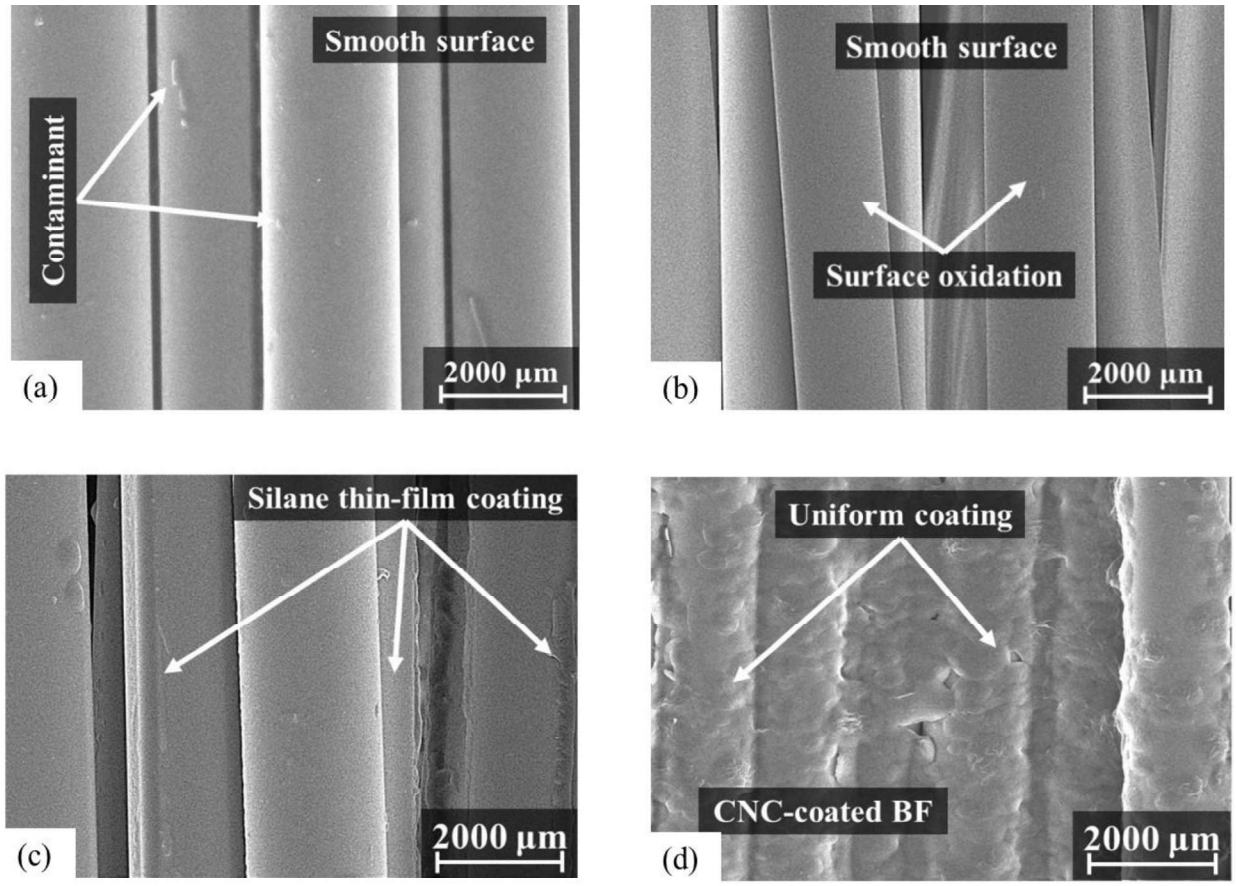

Fig. 6.8. SEM images of CNC grafting process: (a) Pristine BF, (b) Flame-treated BF, (c) Silane-coated BF, (d) CNC-coated BF

The CNC layer is well-adhered to the BF, assisted by the intermediate silane coupling agent, providing both nanoscale surface roughness and chemical compatibility. This enhanced

interfacial architecture in the CNC-grafted BF offers a microstructural explanation for the improved mechanical performance, particularly the increased resistance to shear-induced delamination observed in CNC-modified BFRP specimens under dynamic loading.

6.5.2. Influence of Surface Treatment on Impact Performance

The force-displacement curves for the dynamic impact response of both CNC-modified and unmodified hat-shaped BFRP composites under three span lengths of 80 mm, 140 mm, and 200 are presented in Fig. 6.9(a–c), respectively. The unmodified composites exhibited lower peak forces followed by abrupt load drops, indicating limited energy dissipation. In contrast, the CNC-modified specimens consistently demonstrated higher peak forces across all tested span lengths, accompanied by more gradual force reductions and slightly greater displacements before failure. This suggests improved load-bearing capacity and enhanced energy absorption due to better fiber–matrix interaction. Furthermore, the modified composites exhibited a more stable and progressive post-damage response, particularly at shorter spans. This indicates that the CNC surface treatment not only enhances interfacial adhesion but also promotes more controlled damage evolution under dynamic loading. These observations suggest an enhanced fiber/matrix interfacial bonding and improved energy dissipation capacity in the modified composites. The peak impact force was found to increase for both modified and unmodified composites as the span length decreased, which can be attributed to increased structural stiffness and reduced deformation freedom at shorter spans, as clearly observed in both the force-displacement and energy-displacement curves shown in Fig. 6.9 and Fig. 6.10, respectively. Specifically, at the shortest span of 80 mm, the CNC-modified composite achieved an average peak load of 17.95 kN, significantly higher than the 12.33 kN recorded for its unmodified counterpart. The reduction in peak forces at a span length of 200 mm reflects a transition towards bending-

dominated failure modes at larger spans. Moreover, the CNC-modified composites consistently outperformed the unmodified ones across all span lengths, exhibiting increases in peak forces. These improvements further confirm the beneficial role of CNC in enhancing load transfer efficiency at the fiber-matrix interface with more progressive damage evolution under the varying span conditions. The force-displacement and energy-displacement curves obtained in this study exhibited similar trends to those reported by [168–170], demonstrating strong consistency in the dynamic response characteristics of hat-shaped FRP composites.

At the 80 mm span, the composite exhibits higher global stiffness and peak contact forces, resulting in lower displacement under impact. However, the concentration of shear forces near the supports significantly increases, leading to elevated interlaminar shear stresses. These stresses promote internal damage mechanisms, primarily delamination between the fiber and matrix layers. As delamination progresses, the structure loses its ability to engage in fiber-dominated or plastic deformation, ultimately resulting in brittle-like failure. This behavior is characteristic of composite laminates subjected to high shear gradients, where shear-induced delamination dominates over tensile or compressive fiber failure.

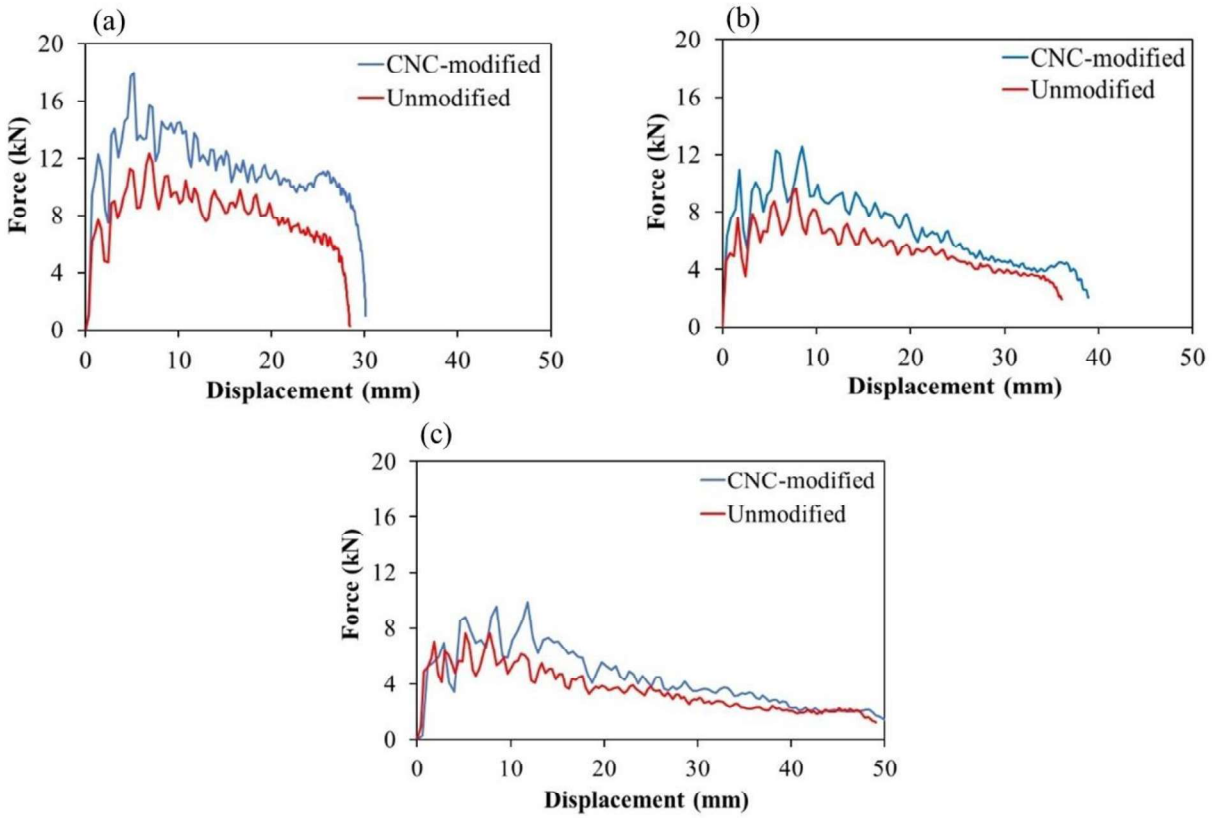

Fig. 6.9. Force-displacement curves for both CNC-modified and unmodified BFRP at varying span lengths: (a) 80 mm, (b) 140 mm, (c) 200 mm

As shown in Fig. 6.10(a–c) and summarized in Table 6.3, the absorbed energies were significantly higher in the CNC-modified BFRP composites compared with the unmodified ones across all the tested span lengths. Specifically, the CNC-modified specimens exhibited energy absorption increases of approximately 50%, 36%, and 27% at the 80 mm, 140 mm, and 200 mm spans, respectively. This improvement is primarily attributed to the enhanced interfacial bonding between the BF and epoxy matrix due to the incorporation of CNC. The CNC likely contributes to mechanisms such as crack deflection, crack bridging, and increased matrix ductility, which together promote more effective energy dissipation under dynamic loading conditions. Statistical analysis using two-sample t-tests, as presented in Table 6.3, revealed that the improvements in energy absorption achieved through CNC modification are statistically significant ($p < 0.05$) for

all three span lengths. This indicates that the observed enhancement is consistent and not limited to a specific geometric configuration. The magnitude of the improvement exceeds the experimental variability, as reflected by the corresponding standard deviations (Table 6.4), highlighting the effectiveness of the CNC modification. These results provide strong experimental support for the enhanced material properties adopted in the numerical modeling. In addition, to evaluate the structural efficiency of the modified composites, the SEA was calculated by normalizing the absorbed energy with respect to the mass of each sample and compared to that of the unmodified BFRP, as shown in Table 6.4 and Appendix (Fig. A4).

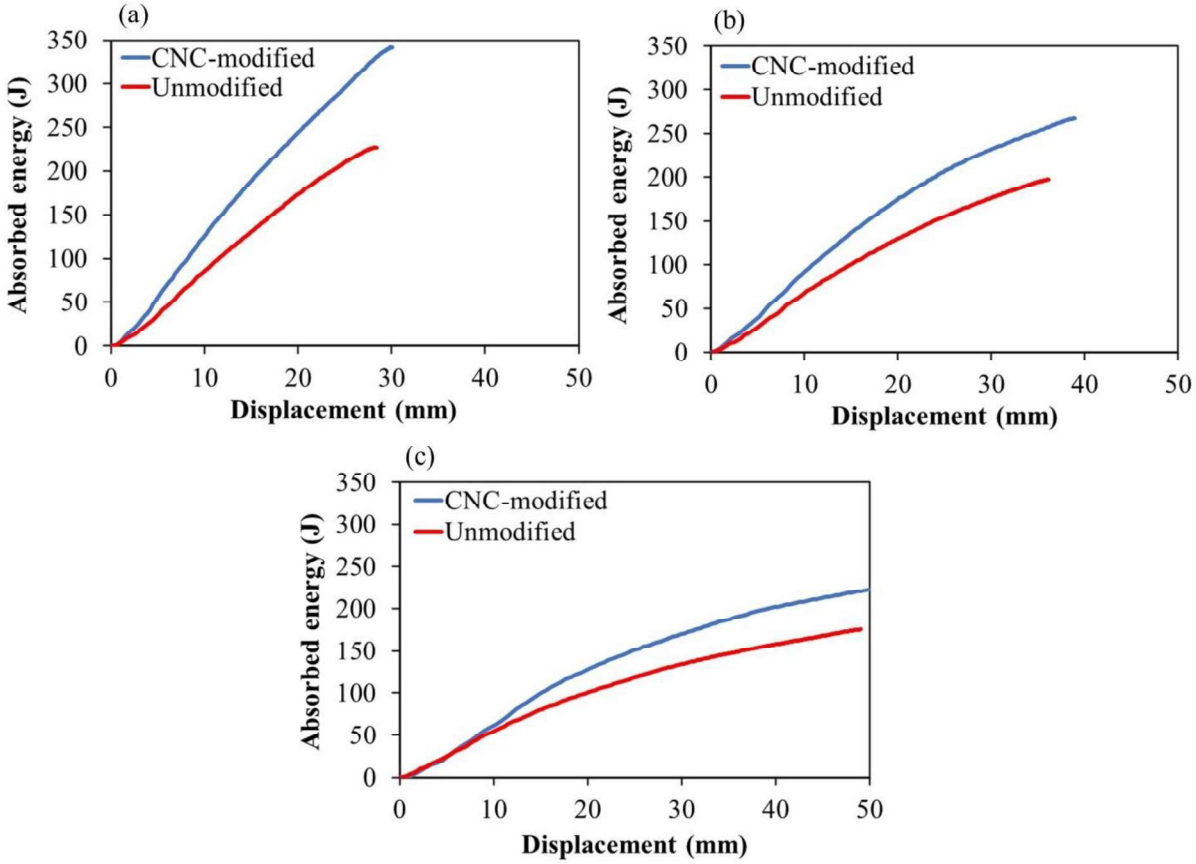

Fig. 6.9. Energy-displacement curves for both CNC-modified and unmodified BFRP at varying span lengths: (a) 80 mm, (b) 140 mm, (c) 200 mm

Table 6.3. Statistical significance results from two-sample t-tests (assuming unequal variances) for three span lengths

Span = 80 mm

	Reference	**CNC-Modified**
Mean	227.18	341.56
Variance	191.3788	9.9631
Observations	3	3
Hypothesized Mean Difference	0	
df	2	
t Stat	-13.96187155	
P(T<=t) one-tail	0.002545403	
t Critical one-tail	2.91998558	
P(T<=t) two-tail	**0.005090805**	
t Critical two-tail	4.30265273	

Span = 140 mm

	Reference	**CNC-Modified**
Mean	197.13	267.52
Variance	215.7987	50.0527
Observations	3	3
Hypothesized Mean Difference	0	
df	3	
t Stat	-7.477425879	
P(T<=t) one-tail	0.002476881	
t Critical one-tail	2.353363435	
P(T<=t) two-tail	**0.004953762**	
t Critical two-tail	3.182446305	

Span = 200 mm

	Reference	**CNC-Modified**
Mean	175.35	222.24
Variance	31.0807	168.2479
Observations	3	3
Hypothesized Mean Difference	0	
df	3	
t Stat	-5.752492377	
P(T<=t) one-tail	0.005218355	
t Critical one-tail	2.353363435	
P(T<=t) two-tail	**0.010436711**	
t Critical two-tail	3.182446305	

Table 6.4. Experimental and numerical results of the dynamic impact analysis

Specimen/ test type	**Peak force (kN)**	**Displacement (mm)**	**Mass (g)**	**EA (J)**	**SEA (J/g)**
Ref-1-1	13.32	28.38	102.70	230.40	2.24
Ref-1-2	11.05	27.20	103.38	239.12	2.31
Ref-1-3	12.63	33.78	92.22	212.02	2.30
Mean ± SD	12.33 ± 0.95	29.79	99.43	227.18 ± 11.3	2.28 ± 0.03
Simulation	*11.24*	*29.93*	—	*238.91*	—
Ref-2-1	9.57	35.17	157.42	209.42	1.33
Ref-2-2	8.91	40.13	154.49	180.86	1.17
Ref-2-3	10.44	36.10	166.51	201.11	1.21
Mean ± SD	9.64 ± 0.63	37.13	159.47	197.13 ± 12.0	1.24 ± 0.07
Simulation	*8.61*	*38.22*	—	*192.35*	—
Ref-3-1	8.26	48.68	204.12	179.34	0.87
Ref-3-2	7.89	49.03	211.68	177.73	0.84
Ref-3-3	6.74	52.06	210.40	168.98	0.80
Mean ± SD	7.63 ± 0.65	49.92	208.73	175.26 ± 4.6	0.84 ± 0.03
Simulation	*7.95*	*47.96*	—	*170.24*	—
CNC-1-1	19.02	28.13	104.40	345.15	3.31
CNC-1-2	17.28	32.28	105.11	339.22	3.23
CNC-1-3	17.55	29.89	98.29	340.31	3.46
Mean ± SD	17.95 ± 0.77	30.10	102.60	341.56 ± 2.6	3.33 ± 0.1
Simulation	*16.47*	*29.20*	—	*330.49*	—
CNC-2-1	12.27	40.01	160.41	261.54	1.63
CNC-2-2	13.15	35.49	158.99	275.33	1.73
CNC-2-3	12.28	41.23	158.8	265.69	1.67
Mean ± SD	12.57 ± 0.41	38.91	159.40	267.52 ± 5.8	1.68 ± 0.04
Simulation	*12.83*	*34.65*	—	*271.29*	—
CNC-3-1	10.40	48.89	209.90	230.14	1.10
CNC-3-2	9.91	49.08	215.01	229.31	1.07
CNC-3-3	9.27	52.30	212.57	207.27	0.98
Mean ± SD	9.86 ± 0.46	50.09	212.49	222.24 ± 10.6	1.05 ± 0.05
Simulation	*9.93*	*46.81*	—	*239.59*	—

6.5.3. Post-Impact Failure Mode Analysis

Post-impact examination of the hat-shaped BFRP specimens revealed distinct differences in failure modes between the CNC-modified and unmodified composites across the three

different spans. Although both materials exhibited comparable overall failure patterns, particularly at longer spans where tensile failure dominates, a clear distinction can be seen upon closer observation. In the unmodified composites, shear-induced delamination was more prevalent, with damage initiating and propagating primarily through interlaminar shear planes. This behavior was especially noticeable at shorter spans, where the combination of high shear forces and limited structural flexibility intensified interfacial separation and delamination propagation. In contrast, the CNC-modified specimens showed a tendency for tensile failure to occur earlier in the damage sequence, especially in the outer fiber layers, due to more resistance to delamination. This behavior suggests that the enhanced interfacial bonding enabled by CNC surface treatment improved the load transfer between the fibers and matrix, thereby preventing premature shear failure. As a result, the modified composites were able to accommodate more tensile stress before shear-driven delamination is initiated, as clearly observed across the three span lengths shown in Fig. 6.10. While the global failure modes were not drastically different at longer spans, where bending-induced tensile failure naturally dominates, the CNC-modified composites consistently demonstrated a more progressive and less brittle failure process. This proved the role of CNC surface treatment in strengthening the fiber–matrix interface, which in turn shifts the failure mechanism from early shear delamination to more controlled tensile rupture. These observations confirm the mechanical performance trends discussed earlier and validate the beneficial effect of CNC modification in enhancing both the strength and failure resistance of BFRP composites under dynamic impact conditions.

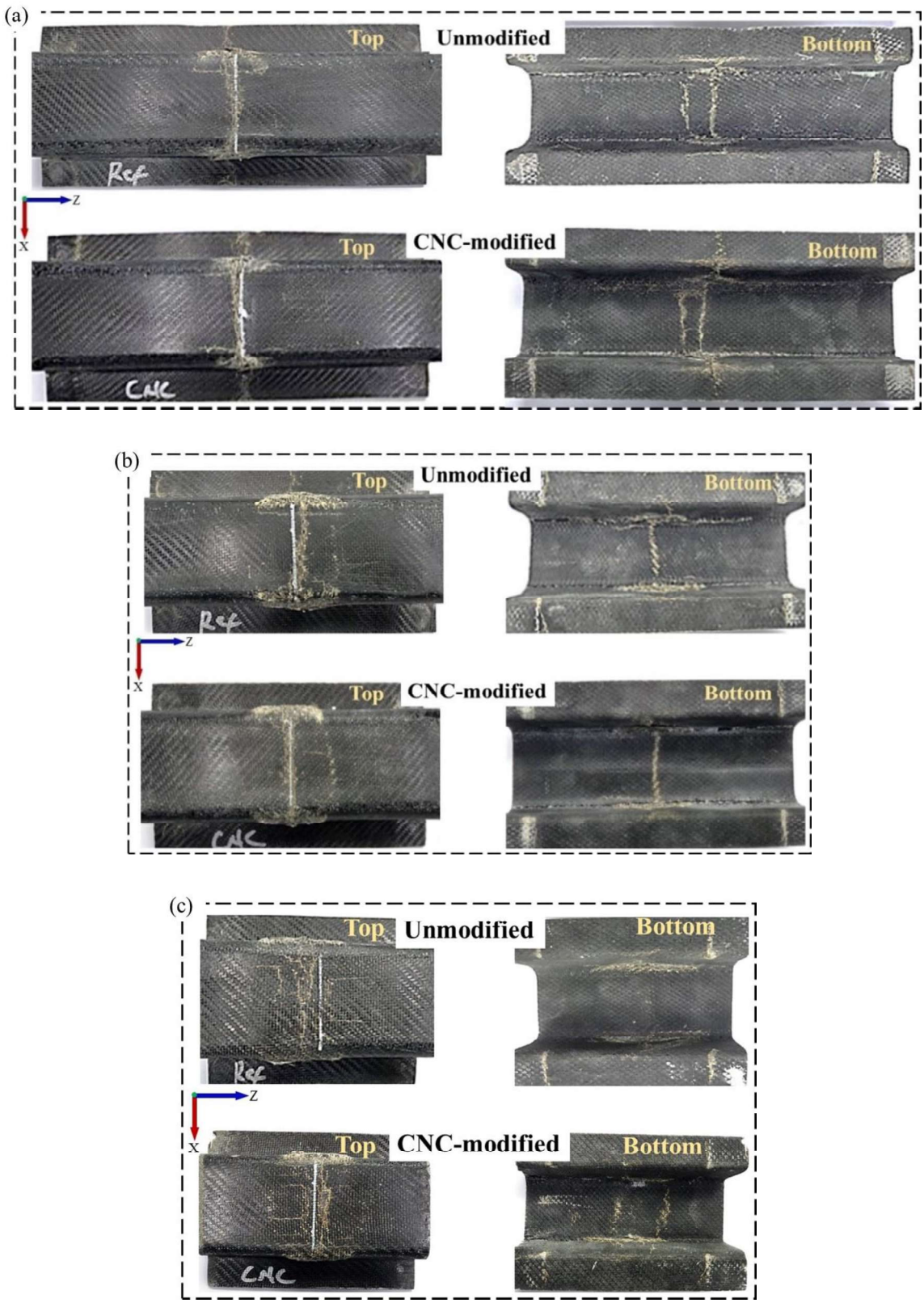

Fig. 6.10. Experimental failure patterns in both CNC-modified and unmodified BFRP at different span lengths: (a) 200 mm, (b) 140 mm, (c) 80 mm

6.5.4. Experimental vs numerical analysis

The force–displacement responses obtained from both experimental tests and FE simulations for unmodified and CNC-modified hat-shaped BFRP composites are presented and compared to assess the accuracy and predictive capability of the numerical model. As illustrated in Fig. 6.11, there is a strong correlation between the experimental and simulated curves across all six test cases. In particular, the initial stiffness shows good agreement with the experimentally measured values for all cases, as evidenced by the force-displacement comparisons. This observation is consistent with the findings reported by [168] for hat-shaped CFRP composites under similar testing conditions. This consistency between numerical and experimental results validates the accuracy of the simulation approach in capturing the initial elastic response of the structures under dynamic loading. For the unmodified composite, the simulation accurately captured the limited peak force behavior observed in the experimental results, effectively representing the material's relatively weaker impact response and the moderately sharp load drop following initial failure. In the case of CNC-modified BFRP, the simulation closely replicated the more gradual force decline as observed experimentally. The model successfully predicted the higher peak forces and improved energy absorption associated with enhanced interfacial bonding due to CNC surface treatment. The more progressive damage evolution in the modified composite was well represented in the simulation results, indicating that the constitutive model and interface definitions effectively captured the toughening effects introduced by CNCs. The slight differences in the post-peak curves' behavior between experimental and simulation are attributed to the idealized material assumptions and limitations in modeling the progressive delamination and fiber breakage mechanisms.

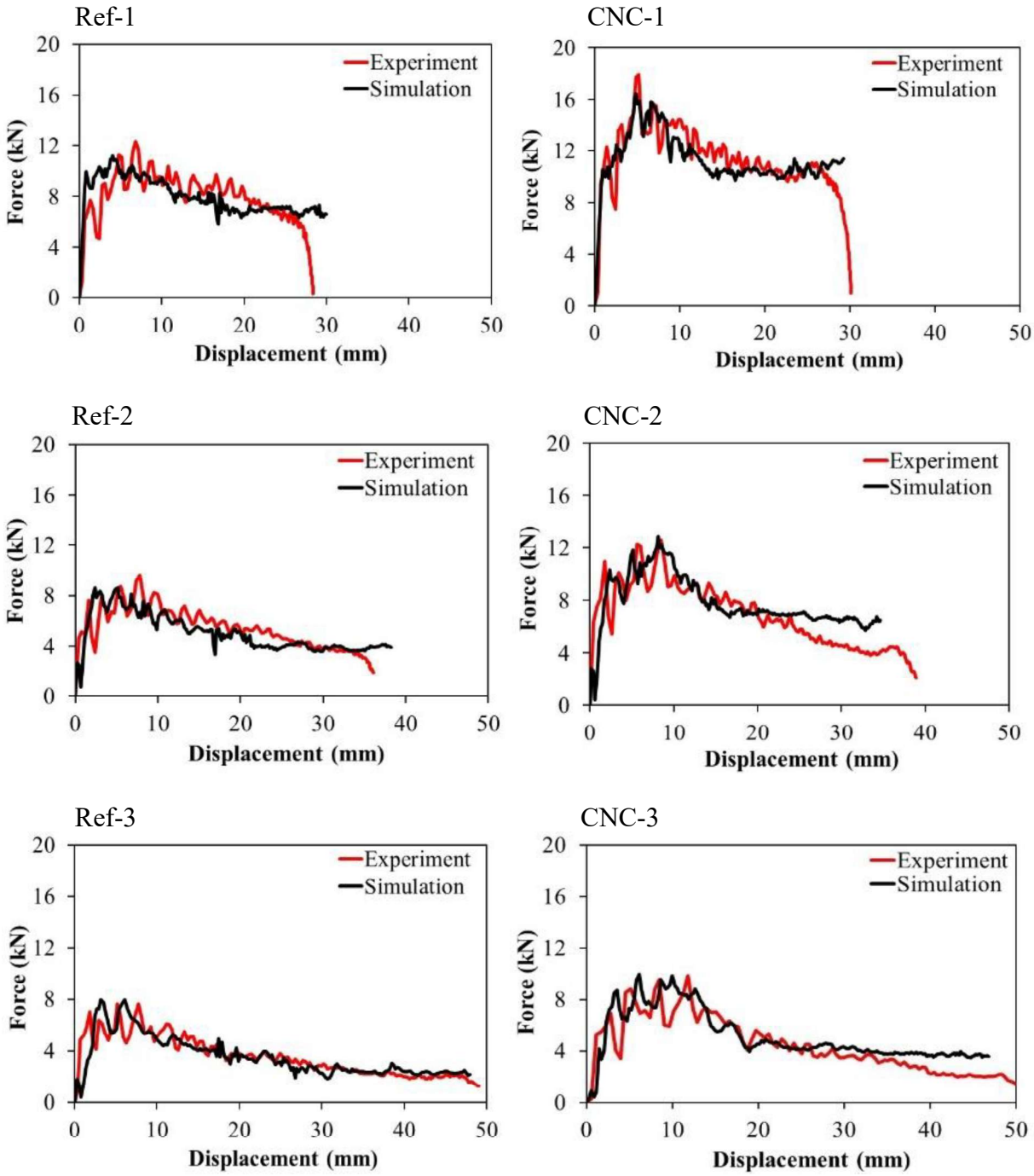

Fig. 6.11. Comparison of experimental and simulated force–displacement responses for the six test cases

Fig. 6.12 illustrates the span-dependent variations in EA and peak force for CNC-modified and unmodified BFRP specimens, along with their corresponding numerical predictions. As shown in Fig. 6.12(a) and (b), the CNC-modified composites consistently exhibit superior

performance in both peak force and EA across all tested spans, following the same trends observed in the experimental results. This improvement is attributed to enhanced interfacial bonding provided by CNC surface treatment, which likely delays delamination onset and promotes more stable energy dissipation mechanisms during impact. The most significant improvement is observed at the shortest span length (80 mm), where the modified specimen achieves an average EA of 341.56 J, closely matched with the simulation result of 330.49 J, as summarized in

Table 6.5. In addition, the CNC-modified specimens exhibit comparable and lower standard deviation (SD) variability than the reference specimens, particularly for CNC-1 and CNC-2, indicating a more stable and consistent energy absorption response after modification. The slightly higher SD observed in some cases reflects normal experimental variability associated with progressive crushing behavior. The numerical predictions were generally within an acceptable deviation from experimental measurements, demonstrating the reliability and accuracy of the FE model. The implementation of CZM is particularly critical in accurately capturing complex failure mechanisms, including matrix cracking, interfacial separation, and progressive delamination under dynamic loading.

The FE model successfully replicates both peak force and EA responses across all span lengths for both modified and unmodified specimens. Quantitatively, the deviation between simulated and experimental EA values remained below 8% across all test cases (see

Table 6.5), further validating the robustness of the simulation results. This agreement between simulation and experiment not only validates the modeling methodology but also emphasizes the potential of using CZM-based FEA as a predictive tool for optimizing composite

structures under varying boundary conditions. It also reinforces the critical role of span length in determining failure modes and energy dissipation mechanisms in composite structures.

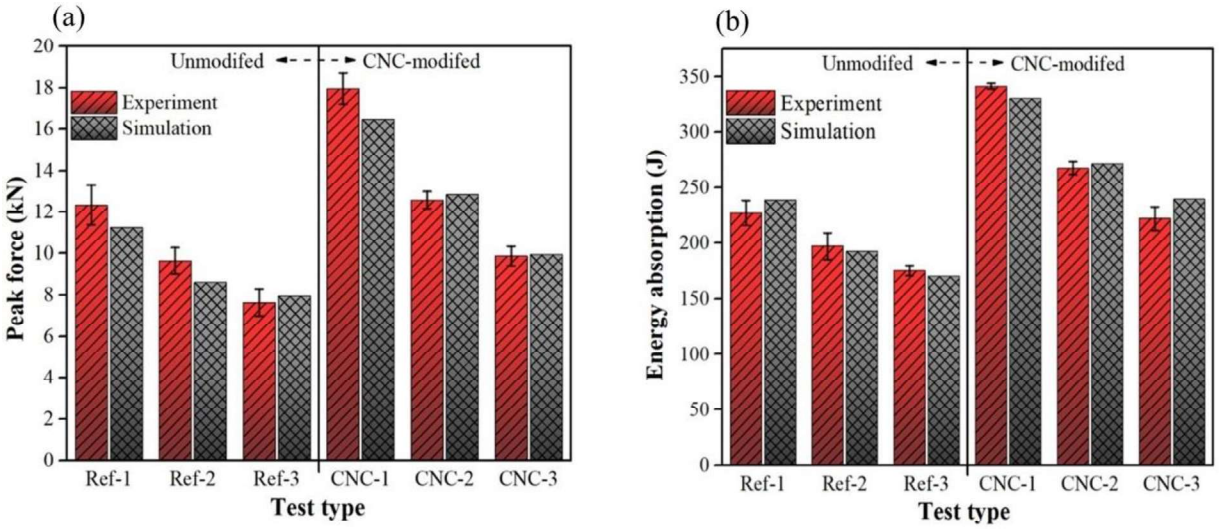

Fig. 6.12. Experimental and numerical results for CNC-modified and unmodified BFRP composites: (a) Peak force, (b) Energy absorption

Table 6.5. Experimental validation of numerical EA prediction in modified and unmodified BFRP Composites at varying span lengths

Test type	Experimental EA (J) mean ± SD	Numerical EA (J)	Difference (%)
Ref-1	227.18 ± 11.3	238.91	4.9
Ref-2	197.13 ± 12.0	192.35	2.5
Ref-3	175.26 ± 4.6	170.24	3.0
CNC-1	341.56 ± 2.6	330.49	3.4
CNC-2	267.52 ± 5.8	271.29	1.4
CNC-3	222.24 ± 10.6	239.59	7.2

6.5.5. Failure modes analysis

The dynamic impact behavior of the hat-shaped BFRP composites tested at span lengths of 80 mm, 140 mm, and 200 mm reveals distinct span-dependent failure characteristics. The structural response and resulting failure modes are governed by the interplay between bending

stiffness, shear forces, and energy dissipation mechanisms. As illustrated in Fig. 6.13, the shorter-span specimens (80 mm) predominantly fail due to shear-induced damage, particularly delamination, whereas the longer-span specimens (200 mm) are characterized by tensile and bending-dominated failures, such as fiber pull-out and matrix cracking. These experimental observations correlate well with the simulation results, confirming the predicted stress distributions and failure patterns across the different span lengths. The intermediate span length (140 mm) exhibits a transitional failure behavior, showing a combination of shear and tensile failure modes, indicating a shift in the dominant stress distribution from shear toward bending with increasing span length.

The accurate prediction of deformation and failure modes confirms that the numerical model can reliably simulate the structural response of both untreated and surface-treated hat-shaped BFRP composites under dynamic impact conditions. As shown in Fig. 6.14, the experimentally observed deformation mode after impact closely matched those predicted by the numerical simulation. This strong visual correlation between the physical and simulated specimens further validates the model's capability to capture realistic failure mechanisms and energy absorption behavior. Additional confirmation is provided by the well-matched force–displacement curves presented in Fig. 6.11, which demonstrate the consistency between experimental and numerical results. This consistency affirms the effectiveness of the developed FE model as a reliable tool for analyzing and optimizing crashworthy composite structures under dynamic loading. Furthermore, the simulation accurately reproduced the boundary conditions and dynamic impact response observed during the experimental setup, reinforcing the reliability and applicability of the developed FE model.

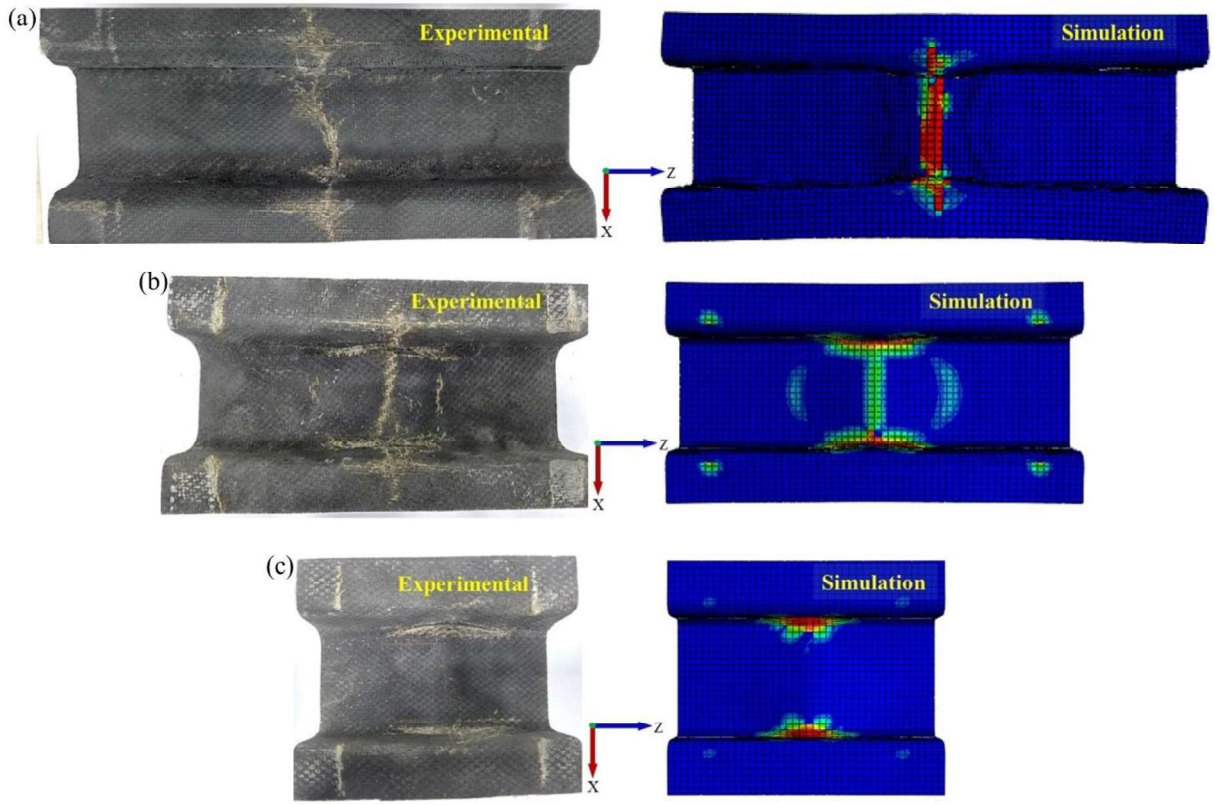

Fig. 6.13. Correlation of experimental and numerical failure patterns in BFRP Structures at different span lengths: (a) 200 mm, (b) 140 mm, (c) 80 mm

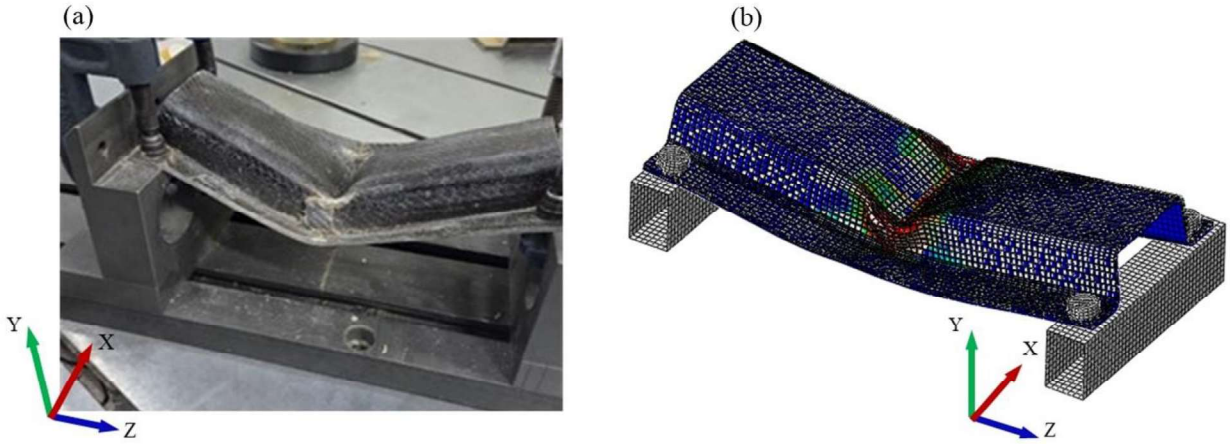

Fig. 6.14. Deformation pattern of BFRP under dynamic impact: (a) Experimental, (b) Simulation

The post-impact response of the hat-shaped BFRP composites with varying span lengths (80 mm, 140 mm, and 200 mm) revealed a clear span-dependent deformation behavior. As shown in Fig. 6.15(a) for the shortest span, the unmodified BFRP specimens exhibited

distinct delamination along the mid-thickness plane, where shear forces are typically highest. This delamination was evident in both the experimental and FE simulations. By contrast, the CNC-modified composites showed no visible delamination in either experimental or simulated results, indicating improved interlaminar bonding strength that effectively suppressed delamination initiation. Importantly, such delamination behavior was only observed at the 80 mm span. At a longer span (200 mm), the dominant failure mode transitioned to global bending and progressive tensile fracture as shown in Fig. 6.13(a), which dissipates the impact energy over a broader region and reduces localized interlaminar stresses. The strong correlation between the physical damage and the simulated deformation, as well as failure patterns, highlights the accuracy of the numerical model in replicating real-world structural behavior. The scalar stiffness degradation (SDEG) contours further support this observation, with the unmodified BFRP showing a narrow range of high damage values near 1.0, indicating early and extensive stiffness degradation. Conversely, the CNC-modified BFRP exhibited a broader distribution of SDEG values, ranging from approximately 0.51 to 1.0, reflecting delayed damage initiation and greater overall damage tolerance.

This improved interfacial bonding performance, enabled by CNC surface treatment, strengthens delamination resistance and facilitates more gradual energy dissipation during impact. This is consistent with the improved EA and SEA values summarized in Table 3, supporting the conclusion that CNC surface modification significantly enhances the crashworthiness and structural reliability of BFRP composite under dynamic loading.

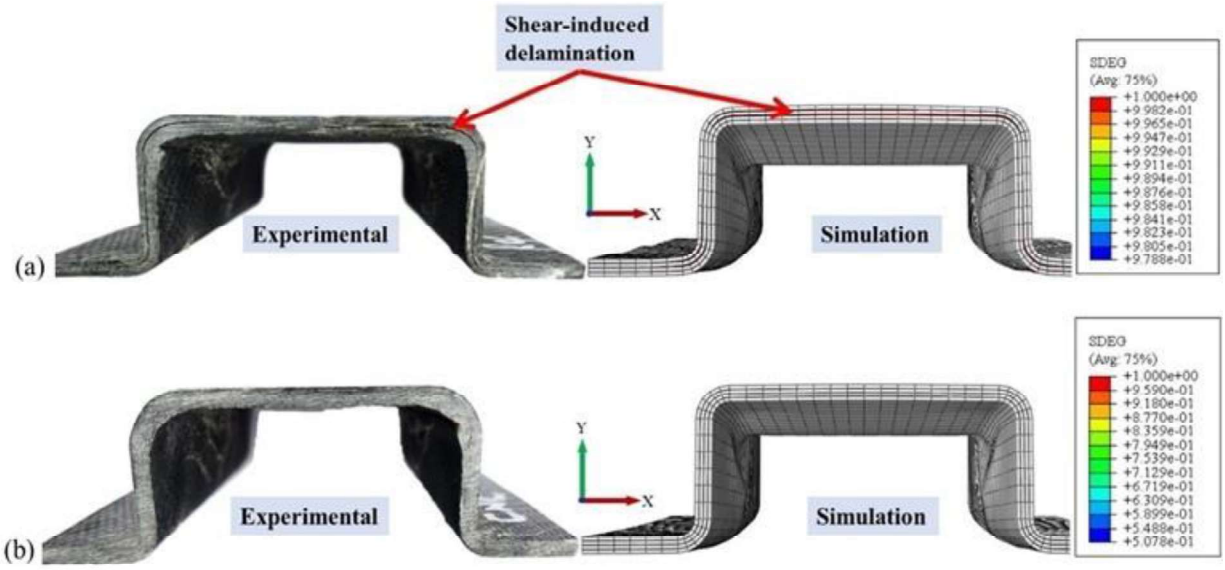

Fig. 6.15. Comparative post-impact deformation patterns of hat-shaped BFRP composites (80 mm span) from experiment and simulation: (a) Unmodified specimen, (b) CNC-modified specimen

6.6. Concluding Remark

This chapter presented a combined experimental and numerical investigation on the dynamic impact response and crashworthiness of hat-shaped BFRP composite structures. The effects of CNC surface modification and span-dependent failure mode transitions were thoroughly examined. The results highlight the promising potential of BFRP composites as sustainable and high-performance materials for dynamic and load-bearing applications. CNC treatment significantly enhanced the energy absorption capacity and delamination resistance, effectively addressing the limitations associated with unmodified BFRP composites. A distinct transition in failure mechanisms from shear-induced failure at shorter spans to tensile failure at longer spans was observed, offering a valuable perspective for optimizing structural design under impact conditions. Numerical simulations closely matched the experimental results, providing high validation and deeper insight into the deformation and failure mechanisms of the hat-shaped

BFRP components under dynamic loading. This strong agreement demonstrates the predictive power of FEA, enabling efficient studies and rapid optimization of composite structures for crashworthiness. Although the CNC grafting approach requires additional fiber surface modification steps before composite fabrication, the associated gains in energy absorption are highly relevant for impact-sensitive automotive structures, where improved crash energy dissipation can offset the increased processing effort. In addition, the demonstrated compatibility of this surface functionalization with well-established and scalable composite manufacturing techniques, including prepreg processing and resin transfer molding (RTM), highlights its potential for industrial-scale application.

CHAPTER SEVEN

7. CONCLUSION, CONTRIBUTIONS, AND RECOMMENDATIONS

7.1. Conclusions

This study successfully developed and validated a bio-based BFRP composite system with improved performance. The key conclusions arising from this study are summarized as follows:

i. A successful grafting strategy was developed for anchoring NCs onto silane-functionalized BF surfaces, improving fiber–matrix compatibility and load transfer while minimizing agglomeration compared with the conventional direct-mixing approach.
ii. The effect of NC type on interfacial bonding was established, with CNC improving interlaminar shear strength and impact energy absorption, while CNF provided superior tensile reinforcement, confirming the critical role of NC morphology in interfacial load transfer.
iii. The developed composites exhibited enhanced tensile strength, impact resistance, and interlaminar shear strength compared with unmodified BFRP composites, confirming the reinforcing effect of NC modification.
iv. Microstructural analysis confirmed improved interfacial adhesion, reduced fiber pull-out, and suppressed crack propagation due to effective NC grafting at the fiber–matrix interface.
v. The modified composites demonstrated improved durability, with lower moisture-induced degradation and better retention of mechanical properties after conditioning.
vi. Experimental and numerical analyses confirmed that the optimized composites possess the structural integrity and dynamic performance required for structural and automotive applications.

vii. FE simulations accurately predicted the mechanical response and interfacial damage behavior of the developed composites, validating the reliability of the computational models for BFRP performance assessment.

7.2. Contributions of the study

Key contributions of this study to the advancement of sustainable composite materials are highlighted as follows:

Scientific Contributions

i. This work provides a comprehensive analysis of existing research on bio-based fibers and nanomaterial-reinforced polymer composites, presented in two peer-reviewed articles, which identify key interfacial and processing limitations in BFRP systems that define the research gap addressed in this study.

ii. The integration of biodegradable NC into the BF surface contributes new scientific knowledge toward overcoming the mechanical limitations of BFRP composites, thereby positioning them as sustainable alternatives to conventional fiber-reinforced polymers for structural applications.

Methodological Contributions

iii. This study successfully developed a novel water-based grafting method for incorporating NCs onto silane-treated BF. This approach addresses the challenge of NC dispersion in hydrophobic matrices and significantly improves the interfacial bonding between BF and the epoxy resin.

Practical/Industrial Contributions

iv. A new hat-shaped structural component was designed and fabricated using NC-modified BFRP composites.

v. The strong correlation between simulation and experimental results confirms the practical viability of the developed composite as an impact-resistant, energy-absorbing structural component with significant potential for automotive applications.

7.3. Limitations and Challenges

i. The sequential grafting process involves multiple treatment steps, making it time-consuming and may create some challenges to scale for industrial production.

ii. Achieving uniform NCs deposition along the fibers remains challenging, and variations in grafting density may affect composite performance.

iii. Although the hat-shaped BFRP component demonstrated enhanced impact performance, only a limited range of impact energies and boundary conditions was examined due to the capabilities of the available impact testing equipment, representing a potential limitation of the study.

7.4. Recommendations for Future Work

i. Future studies should explore advanced characterization techniques such as cross-sectional TEM or AFM to directly measure the thickness of the grafted NC layer.

ii. Investigate the compatibility of NC-grafted BFs with different polymer matrices (e.g., bio-based resins or thermoplastics) could expand the application scope of this approach.

iii. To fully establish the sustainability and economic viability of this modification route, a detailed life cycle assessment (LCA) and cost-benefit analysis can be considered.

iv. Future work should examine the industrial scalability of the NC grafting process, with particular emphasis on large-scale manufacturing feasibility, process optimization, and reproducibility under commercial production conditions.

v. Future work should explore the use of AI and machine learning to automate microstructural analysis, predict composite performance, and optimize NC grafting and FE simulation parameters, thereby improving the speed and accuracy of the composite design.

APPENDICES (Supplementary data)

Table A1. Calculated compliance and compliance coefficient values for the tested NC-modified and unmodified BFRP specimens

Specimen (NC)	**Compliance C (mm/N)**			**Compliance coefficient (CC)**	
	a_0 = 20 mm	a_0 = 30 mm	a_0 = 40 mm	m	A
NPC- 6	0.0177	0.01777	0.01911	3.622E-08	0.0173
NPC- 2	0.01356	0.01508	0.01637	4.808E-08	0.0134
NPC- 3	0.01057	0.01214	0.01605	9.893E-08	0.0097
NPC- 4	0.01045	0.01238	0.01644	1.073E-07	0.0095
NPC- 5	0.01037	0.01173	0.01559	9.474E-08	0.0094
Average				7.71E-08	0.0119
Standard deviation				2.903E-08	0.00311
Specimen (NC)	**Compliance C (mm/N)**			**Compliance coefficient (CC)**	
	a_0 = 20 mm	a_0 = 30 mm	a_0 = 40 mm	m	A
PC- 6	0.01921	0.02072	0.02638	1.315E-07	0.0178
PC- 2	0.01569	0.0198	0.02802	2.205E-07	0.0139
PC- 3	0.01366	0.01835	0.02618	2.219E-07	0.0121
PC- 4	0.01235	0.01629	0.02448	2.173E-07	0.0105
PC- 5	0.0147	0.021	0.02968	2.630E-07	0.0131
Average				2.11E-07	0.0135
Standard deviation				4.307E-08	0.00244
Specimen (Ref)	**Compliance C (mm/N)**			**Compliance coefficient (CC)**	
	a_0 = 20 mm	a_0 = 30 mm	a_0 = 40 mm	m	A
NPC- 1	0.01465	0.0175	0.02595	2.054E-07	0.0126
NPC- 2	0.01491	0.01525	0.01795	5.684E-08	0.0142
NPC- 3	0.01416	0.01561	0.01899	8.695E-08	0.0134
NPC- 4	0.01470	0.01783	0.02418	1.697E-07	0.0133
NPC- 5	0.01429	0.01549	0.01945	9.418E-08	0.0133
Average				1.23E-07	0.0134
Standard deviation				5.567E-08	0.000508
Specimen (Ref)	**Compliance C (mm/N)**			**Compliance coefficient (CC)**	
	a_0 = 20 mm	a_0 = 30 mm	a_0 = 40 mm	m	A
PC- 1	0.01941	0.02722	0.04005	3.657E-07	0.0168
PC- 2	0.01905	0.02585	0.03848	3.462E-07	0.0164
PC- 3	0.01821	0.0251	0.03704	3.344E-07	0.0157
PC- 4	0.01987	0.02808	0.04126	3.784E-07	0.0172
PC- 5	0.01901	0.02586	0.03843	3.458E-07	0.0164
Average				3.54E-07	0.0165
Standard deviation				1.578E-08	0.000498

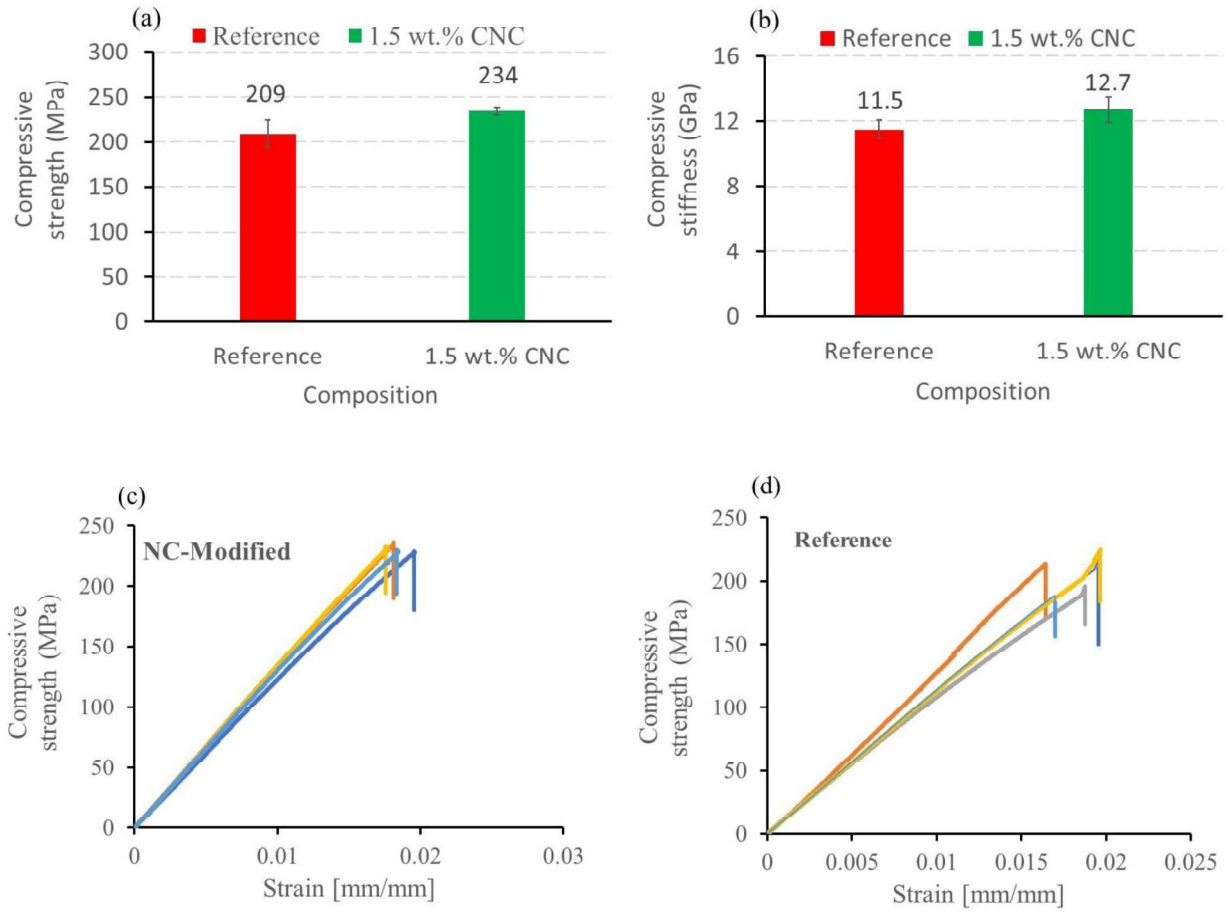

Fig. A1. Compressive test result of the optimized CNC-modified and unmodified BFRP: (a) Compressive strength, (b) Compressive stiffness, (c) Stress-strain curves (modified BFRP), and (d) Stress-strain curves (unmodified BFRP)

Table A2. Mesh convergence analysis of the FEA model for the representative case (80 mm span length)

Mesh level	element size (mm)	Number of elements	Peak force (kN) reference	Peak force (kN) NC-modified	EA (J) reference	EA (J) NC-modified	Difference in peak force (%) reference	Difference in peak force (%) NC-modified
Coarse mesh	4	10500	11.76	17.15	257.23	337.12	2.80	5.41
Medium mesh	3	16800	11.24	16.47	238.91	330.49	1.75	1.23
Fine mesh	2	33600	11.44	16.27	244.76	331.73	—	—

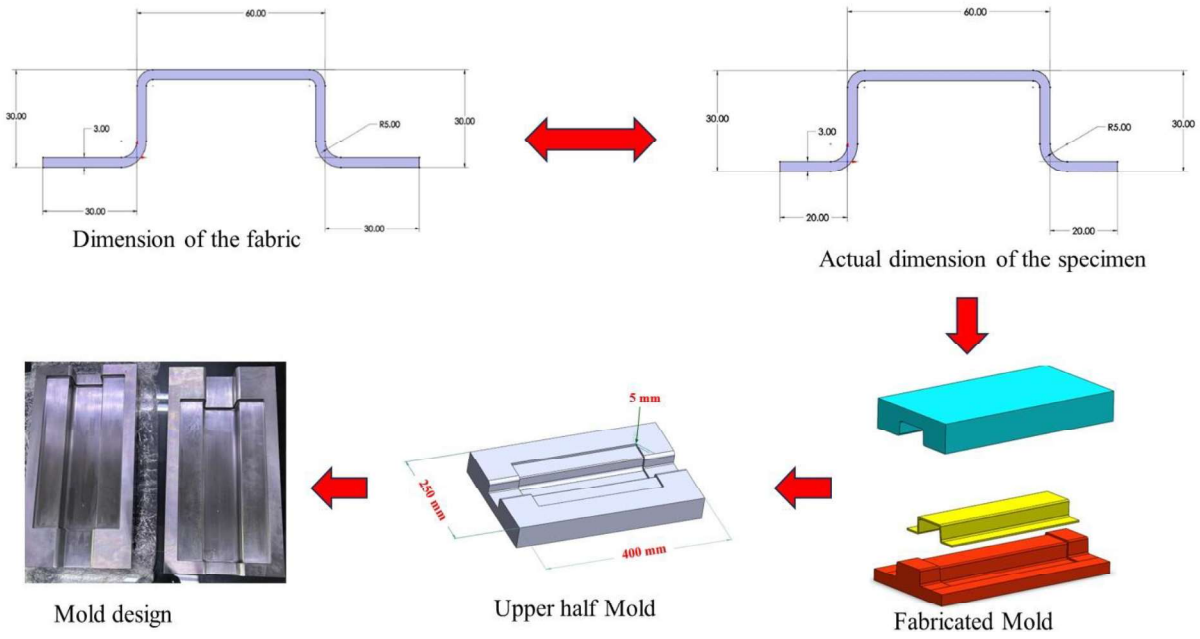

Fig. A2. Mold design for the fabrication of the hat-shaped BFRP composite

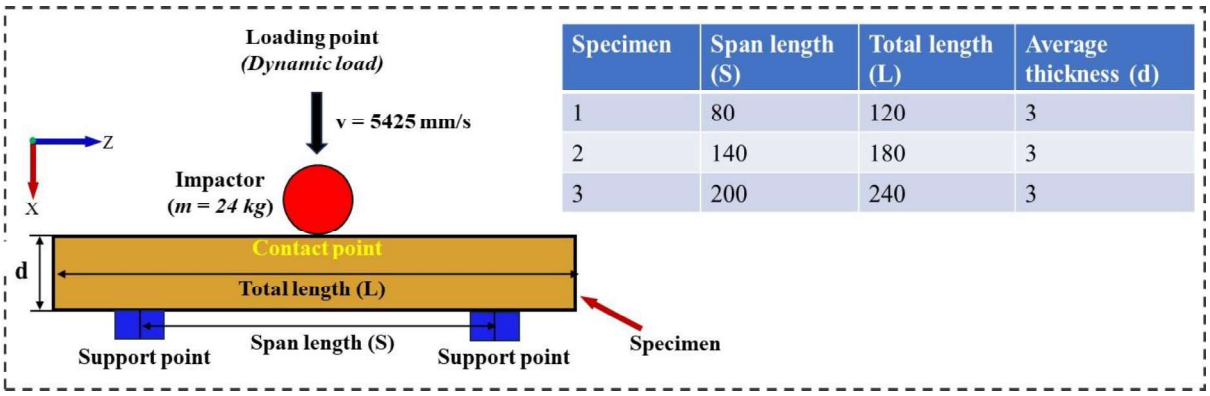

Specimen	Span length (S)	Total length (L)	Average thickness (d)
1	80	120	3
2	140	180	3
3	200	240	3

Fig. A3. Schematic side view of the dynamic impact testing configuration and specimen dimension.

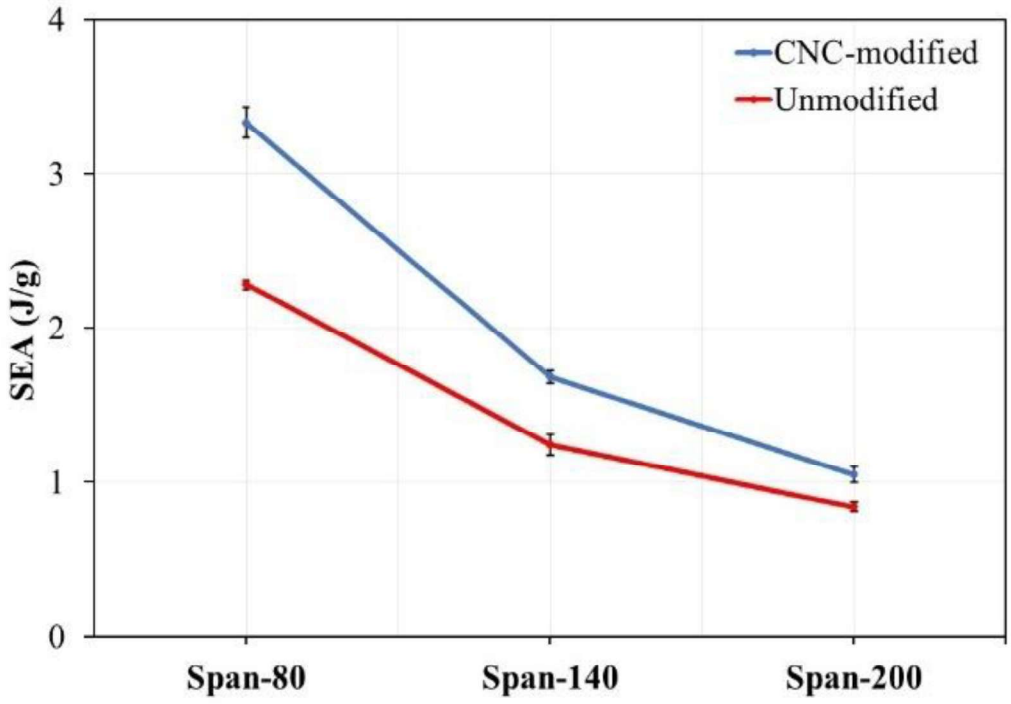

Fig. A4. Crushing efficiency comparison between CNC-modified and unmodified BFRP at varying span lengths

REFERENCES

[1] Dhand V, Mittal G, Rhee KY, Park SJ, Hui D. A short review on basalt fiber reinforced polymer composites. Compos Part B Eng 2015;73:166–80.

[2] Adesina A. Performance of cementitious composites reinforced with chopped basalt fibres – An overview. Constr Build Mater 2021;266:120970.

[3] Li J, Lan L, Zhang Y, Pan B, Shi W, Gu Z, et al. Advancements in Basalt Fiber-Reinforced Composites: A Critical Review. Coatings 2025;15.

[4] Sarr MM, Inoue H, Kosaka T. Study on the improvement of interfacial strength between glass fiber and matrix resin by grafting cellulose nanofibers. Compos Sci Technol 2021;211:108853.

[5] Parveen S, Pichandi S, Goswami P, Rana S. Novel glass fibre reinforced hierarchical composites with improved interfacial, mechanical and dynamic mechanical properties developed using cellulose microcrystals. Mater Des 2020;188:108448.

[6] Zhang W, Xu J. Advanced lightweight materials for Automobiles: A review. Mater Des 2022;221.

[7] Trzepieciński T, Najm SM. Current Trends in Metallic Materials for Body Panels and Structural Members Used in the Automotive Industry. Materials (Basel) 2024;17.

[8] Kim DH, Choi DH, Kim HS. Design optimization of a carbon fiber reinforced composite automotive lower arm. Compos Part B Eng 2014;58.

[9] Zhang J, Lin G, Vaidya U, Wang H. Past, present and future prospective of global carbon fibre composite developments and applications. Compos Part B Eng 2023;250.

[10] Zahoor A, Zhang J, Wu D, Lin Chen J, Nihed B, Sen T, et al. A systematic study involving patent analysis and theoretical modeling of eco-friendly technologies for electric vehicles and power batteries to ease carbon emission from the transportation industry. Energy Convers Manag 2024;321.

[11] Moustafa H, Youssef AM, Darwish NA, Abou-Kandil AI. Eco-friendly polymer composites for green packaging: Future vision and challenges. Compos Part B Eng 2019;172.

[12] Manalu J, Numberi JJ, Safanpo A, Fitriyana DF, Wijaya TL, Siregar JP, et al. Characterization of eco-friendly composites for automotive applications prepared by the compression molding method. Polym Compos 2024;45.

[13] Rame R, Purwanto P, Sudarno S. Industry 5.0 and sustainability: An overview of emerging trends and challenges for a green future. Innov Green Dev 2024;3.

[14] mahboubizadeh S, Sadeq A, Arzaqi Z, Ashkani O, Samadoghli M. Advancements in fiber-reinforced polymer (FRP) composites: an extensive review. Discov Mater 2024;4.

[15] Selvaraj VK, Subramanian J, Suyambulingam I, Viswanath S, Jayamani E, Siengchin S. Influence of bio-based kenaf polymer composites on mechanical and acoustic properties

for futuristic applications: An initiative towards net-zero carbon emissions. Polym Test 2024;134.

[16] Yaumi AL, Bakar MZA, Hameed BH. Recent advances in functionalized composite solid materials for carbon dioxide capture. Energy 2017;124.

[17] Romero CA, Correa P, Ariza Echeverri EA, Vergara D. Strategies for Reducing Automobile Fuel Consumption. Appl Sci 2024;14.

[18] Das S. Life cycle assessment of carbon fiber-reinforced polymer composites. Int J Life Cycle Assess 2011;16.

[19] Witik RA, Teuscher R, Michaud V, Ludwig C, Månson JAE. Carbon fibre reinforced composite waste: An environmental assessment of recycling, energy recovery and landfilling. Compos Part A Appl Sci Manuf 2013;49.

[20] Balaji KV, Shirvanimoghaddam K, Rajan GS, Ellis A V., Naebe M. Surface treatment of Basalt fiber for use in automotive composites. Mater Today Chem 2020;17:100334.

[21] Peng Z, Wang X, Liu X, Ding L, Tang B, Wu Z. Carbon emission assessment of basalt fiber and basalt fiber-reinforced polymer (BFRP) reinforced/strengthened concrete structures. Structures 2026;85.

[22] https://basaltfiberchina.com/properties/environmental-friendliness/ 2025.

[23] Jagadeesh P, Rangappa SM, Fiore V, Nath Dhakal H, Siengchin S. Basalt powder based thermoset and thermoplastic composites for lightweight applications. J Polym Res 2024;31.

[24] Bhat AR, Kumar R, Mural PKS. Natural fiber reinforced polymer composites: A comprehensive review of Tribo-Mechanical properties. Tribol Int 2023;189.

[25] Gauvin F, Cousin P, Robert M. Improvement of the interphase between basalt fibers and vinylester by nano-reinforced post-sizing. Fibers Polym 2015;16.

[26] Balaji KV, Shirvanimoghaddam K, Naebe M. Multifunctional basalt fiber polymer composites enabled by carbon nanotubes and graphene. Compos Part B Eng 2024;268:111070.

[27] Antony Jose S, Cowan N, Davidson M, Godina G, Smith I, Xin J, et al. A Comprehensive Review on Cellulose Nanofibers, Nanomaterials, and Composites: Manufacturing, Properties, and Applications. Nanomaterials 2025;15.

[28] Zhu X, Li Y, Yu T, Zhang Z. Enhancement of the interlaminar fracture toughness and damping properties of carbon fiber reinforced composites using cellulose nanofiber interleaves. Compos Commun 2021;28:100940.

[29] Katagiri K, Kishimoto N, Okumura T, Kawakita S, Honda S, Sasaki K. Effects of cellulose nanofiber content on impact properties of carbon fiber reinforced epoxy composites with the cellulose nanofiber dispersion layer. Mech Adv Mater Struct 2022;29:6087–95.

[30] Shao Y, Yashiro T, Okubo K, Fujii T. Effect of cellulose nano fiber (CNF) on fatigue

performance of carbon fiber fabric composites. Compos Part A Appl Sci Manuf 2015;76:244–54.

[31] Ilyas RA, Asyraf MRM, Rajeshkumar L, Awais H, Siddique A, Shaker K, et al. A review of bio-based nanocellulose epoxy composites. J Environ Chem Eng 2024;12.

[32] Habib A, Firdaus AHM, Sapuan SM, Abral H, Azka MA, Zainudin ES, et al. Recent advancements in nanocellulose reinforced biopolymer hybrid composites: A review. J Clean Prod 2025;496.

[33] Czerwinski F. Current trends in automotive lightweighting strategies and materials. Materials (Basel) 2021;14.

[34] Mallick PK. Fiber-reinforced composites: Materials, manufacturing, and design, third edition. 2007.

[35] William D. Callister, Jr. DGR. An introduction to materials science and engineering, 8th ed. John Wiley & Sons, Inc. vol. 1. 2010.

[36] Egbo MK. A fundamental review on composite materials and some of their applications in biomedical engineering. J King Saud Univ - Eng Sci 2021;33.

[37] Fan Q, Duan H, Xing X. A review of composite materials for enhancing support, flexibility and strength in exercise. Alex Eng J 2024;94.

[38] Gibson RF. A review of recent research on mechanics of multifunctional composite materials and structures. Compos Struct 2010;92.

[39] Rajak DK, Pagar DD, Menezes PL, Linul E. Fiber-reinforced polymer composites: Manufacturing, properties, and applications. Polymers (Basel) 2019;11.

[40] Elmasry A, Azoti W, Ghoniem E, Elmarakbi A. Modelling of hybrid biocomposites for automotive structural applications. Compos Sci Technol 2024;251.

[41] Shah KJ, Pan SY, Lee I, Kim H, You Z, Zheng JM, et al. Green transportation for sustainability: Review of current barriers, strategies, and innovative technologies. J Clean Prod 2021;326.

[42] Musa AA, Onwualu AP. Potential of lignocellulosic fiber reinforced polymer composites for automobile parts production: Current knowledge, research needs, and future direction. Heliyon 2024;10:e24683.

[43] Jagadeesh P, Rangappa SM, Siengchin S. Basalt fibers: An environmentally acceptable and sustainable green material for polymer composites. Constr Build Mater 2024;436.

[44] Kamarudin SH, Mohd Basri MS, Rayung M, Abu F, Ahmad S, Norizan MN, et al. A Review on Natural Fiber Reinforced Polymer Composites (NFRPC) for Sustainable Industrial Applications. Polymers (Basel) 2022;14.

[45] Fiore V, Scalici T, Di Bella G, Valenza A. A review on basalt fibre and its composites. Compos Part B Eng 2015;74.

[46] Jamshaid H, Mishra R. A green material from rock: basalt fiber – a review. J Text Inst

2016;107.

[47] https://volcanoes.usgs.gov/vsc/glossary/basalt.html n.d.

[48] MECHANICAL PROPERTIES OF WOVEN FABRIC BASALT / JUTE FIBRE REINFORCED POLYMER HYBRID COMPOSITES 2013;2.

[49] Kogan FM, Nikitina O V. Solubility of Chrysotile Asbestos and Basalt Fibers in Relation to Their Fibrogenic and Carcinogenic Action. Environ Health Perspect 1994;102.

[50] Mcconnell EE, Kamstrup O, Musselman R, Hesterberg TW, Chevalier J, Miiller WC, et al. Chronic inhalation study of size-separated rock and slag wool insulation fibers in fischer 344/n rats. Inhal Toxicol 1994;6.

[51] Banibayat P, Patnaik A. Variability of mechanical properties of basalt fiber reinforced polymer bars manufactured by wet-layup method. Mater Des 2014;56.

[52] Afroz M, Patnaikuni I, Venkatesan S. Chemical durability and performance of modified basalt fiber in concrete medium. Constr Build Mater 2017;154.

[53] Khandelwal S, Rhee KY. Recent advances in basalt-fiber-reinforced composites: Tailoring the fiber-matrix interface. Compos Part B Eng 2020;192:108011.

[54] Chowdhury IR, Pemberton R, Summerscales J. Developments and Industrial Applications of Basalt Fibre Reinforced Composite Materials. J Compos Sci 2022;6.

[55] Liu H, Yu Y, Liu Y, Zhang M, Li L, Ma L, et al. A Review on Basalt Fiber Composites and Their Applications in Clean Energy Sector and Power Grids. Polymers (Basel) 2022;14:2376.

[56] Ding B, Zhang L, Liu J. Study on Shielding and Radiation Resistance of Basalt Fiber to Gamma Ray. Materials (Basel) 2022;15.

[57] https://basalt.guru/basalt-rebar-high-tensile-strength/ n.d.

[58] Bhat T, Chevali V, Liu X, Feih S, Mouritz AP. Fire structural resistance of basalt fibre composite. Compos Part A Appl Sci Manuf 2015;71.

[59] Chen C, Ding Y, Wang X, Bao L. Recent advances to engineer tough basalt fiber reinforced composites: A review. Polym Compos 2024:12559–74.

[60] Kim SH, Lee JH, Kim JW, Lee SY, Park SJ. Interfacial Behaviors of Basalt Fiber-Reinforced Polymeric Composites: A Short Review. Adv Fiber Mater 2022;4.

[61] Monaldo E, Nerilli F, Vairo G. Basalt-based fiber-reinforced materials and structural applications in civil engineering. Compos Struct 2019;214.

[62] Lee SO, Rhee KY, Park SJ. Influence of chemical surface treatment of basalt fibers on interlaminar shear strength and fracture toughness of epoxy-based composites. J Ind Eng Chem 2015;32.

[63] Kim MT, Kim MH, Rhee KY, Park SJ. Study on an oxygen plasma treatment of a basalt fiber and its effect on the interlaminar fracture property of basalt/epoxy woven composites. Compos Part B Eng 2011;42.

[64] Farsani RE, Daghigh V, Derakhshani K. Tensile and flexural properties of basalt fibers/nano-alumina powder-reinforced multi-scale composites. Surfaces and Interfaces 2024;46.

[65] Rong Y, Zhao P, Shen T, Gao J, Zhou S, Huang J, et al. Mechanical and tribological properties of basalt fiber fabric reinforced polyamide 6 composite laminates with interfacial enhancement by electrostatic self-assembly of graphene oxide. J Mater Res Technol 2023;27:7795–806.

[66] Wang F, Wang J, Fang D, Zhou S, Huang J, Zhao G, et al. Surface sizing introducing carbon nanotubes for interfacial bond strengthening of basalt fiber–reinforced polymer composites. Adv Compos Hybrid Mater 2023;6.

[67] Xiang D, Shui T, Qiao H, Tan W, Harkin-Jones E, Zhang J, et al. Enhanced interfacial interaction, mechanical properties and thermal stability of basalt fiber/epoxy composites with multi-scale reinforcements. Compos Interfaces 2023;30:1387–409.

[68] Kasraie M, Krieg AS, Abbott AC, Gawde A, Eisele TC, King JA, et al. Carbon nanotube as a conductive rheological modifier for carbon fiber-reinforced epoxy 3D printing inks. Compos Part B Eng 2024;282:111583.

[69] Gudonis E, Timinskas E, Gribniak V, Kaklauskas G, Arnautov AK, Tamulėnas V. FRP REINFORCEMENT FOR CONCRETE STRUCTURES: STATE-OF-THE-ART REVIEW OF APPLICATION AND DESIGN. Eng Struct Technol 2014;5.

[70] Tuswan T, Zubaydi A, Piscesa B, Sari EN, Ismail A. Core sandwich material development based on vinyl ester bioresin for ship structure application. IOP Conf Ser Mater Sci Eng 2021;1034.

[71] Sreekumar PA, Selvin Thomas P, Saiter JM, Unnikrishnan G, Thomas S. Viscoelastic and thermal properties of eco-friendly composites fabricated by resin transfer molding. J Reinf Plast Compos 2011;30.

[72] Saw SK, Purwar R, Nandy S, Ghose J, Sarkhel G. Fabrication, characterization, and evaluation of Luffa cylindrica fiber reinforced epoxy composites. BioResources 2013;8.

[73] Refiadi G, Aisyah IS, Siregar JP. Trends in lightweight automotive materials for improving fuel efficiency and reducing carbon emissions. Automot Exp 2019;2.

[74] Serrenho AC, Norman JB, Allwood JM. The impact of reducing car weight on global emissions: The future fleet in Great Britain. Philos Trans R Soc A Math Phys Eng Sci 2017;375.

[75] Diniță A, Ripeanu RG, Ilincă CN, Cursaru D, Matei D, Naim RI, et al. Advancements in Fiber-Reinforced Polymer Composites: A Comprehensive Analysis. Polymers (Basel) 2024;16.

[76] Li S, Dengfeng W, Chaohui Z. Multi-level structural optimization of thin-walled sections in steel/aluminum vehicle body skeletons. Appl Math Model 2024;132:187–210.

[77] Ansari MS, Zafar S, Pathak H. A comprehensive review of surface modification techniques for carbon fibers for enhanced performance of resulting composites. Results in

Surfaces and Interfaces 2023;12.

[78] Wei B, Cao H, Song S. Tensile behavior contrast of basalt and glass fibers after chemical treatment. Mater Des 2010;31:4244–50.

[79] Alshgari RA, Prasad MSC, Srivastava BK, Al Ansari MS, Gupta P, Sivakumar A, et al. Mechanical Evaluation on Carbon/Basalt Fiber-Reinforced Hybrid Polymer Matrix Composite. Adv Polym Technol 2022;2022.

[80] Sun G, Tong S, Chen D, Gong Z, Li Q. Mechanical properties of hybrid composites reinforced by carbon and basalt fibers. Int J Mech Sci 2018;148.

[81] Natarajan E, Mozhuguan Sekar S, Markandan K, Ang CK, Franz G. Tailoring Basalt Fibers and E-Glass Fibers as Reinforcements for Increased Impact Resistance. J Compos Sci 2024;8.

[82] Sukur EF, Elimsa S, Eskizeybek V, Avci A. Damage tolerance of basalt fiber reinforced multiscale composites: Effect of nanoparticle morphology and hygrothermal aging. Compos Part B Eng 2024;273:111234.

[83] Deng T, Peng Z, Gao Y, Zhao H, Xu B, Zhang L, et al. Tadpole-like bottlebrush polymer-modified multiwalled carbon nanotubes: A strategy for interface-strengthened polymer nanocomposites with exceptional performance. Compos Part B Eng 2024;274:111275.

[84] Wang S, Wang T, Zhang S, Dong Z, Chevali VS, Yang Y, et al. Enhancing fiber-matrix interface in carbon fiber/poly ether ether ketone (CF/PEEK) composites by carbon nanotube reinforcement of crystalline PEEK sizing. Compos Part B Eng 2023;251:110470.

[85] Bulut M, Bozkurt ÖY, Erkliğ A, Yaykaşlı H, Özbek Ö. Mechanical and Dynamic Properties of Basalt Fiber-Reinforced Composites with Nanoclay Particles. Arab J Sci Eng 2020;45:1017–33.

[86] Ary Subagia IDG, Tijing LD, Kim Y, Kim CS, Vista Iv FP, Shon HK. Mechanical performance of multiscale basalt fiber-epoxy laminates containing tourmaline micro/nano particles. Compos Part B Eng 2014;58:611–7.

[87] He H, Yang P, Duan Z, Wang Z, Liu Y. Reinforcing effect of hybrid nano-coating on mechanical properties of basalt fiber/poly(lactic acid) environmental composites. Compos Sci Technol 2020;199:108372.

[88] Zhang S, Zhong T, Xu Q, Su Z, Jiang M, Liu P. The effects of chemical grafting 1,6-hexanediol diglycidyl ether on the interfacial adhesion between continuous basalt fibers and epoxy resin as well as the tensile strength of composites. Constr Build Mater 2022;323.

[89] Mittal G, Rhee KY. Electrophoretic deposition of graphene on basalt fiber for composite applications. Nanotechnol Rev 2021;10:158–65.

[90] Tian H, Fan W, Ge S, Xia C, Liu Y, Wang H, et al. Nanofiber–sheathed structure for enhancing interfacial properties of basalt fiber-reinforced composites. Compos Commun 2021;23:100589.

[91] McMullen RL, Ozkan S, Gillece T. Physicochemical Properties of Cellulose Ethers. Cosmetics 2022;9.

[92] Musa AA, Park J, Hong G, Yoon SH, Onwualu AP, Kim M. Development of high-performance basalt fiber-reinforced polymer composite using a nanocellulose-based surface modification strategy. Compos Part A 2025;199:109191.

[93] Bhaganagar S, Biswas PK, Agarwal M, Dalir H. Cellulose Nanofiber Coated Carbon Fiber/Epoxy Composite with Higher Mechanical Strength. AIAA SciTech Forum Expo 2023, 2023.

[94] Kurita H, Xie Y, Katabira K, Honda R, Narita F. The insert effect of cellulose nanofiber layer on glass fiber-reinforced plastic laminates and their flexural properties. Mater Des Process Commun 2019;1.

[95] Azhary T, Kusmono, Wildan MW, Herianto. Mechanical, morphological, and thermal characteristics of epoxy/glass fiber/cellulose nanofiber hybrid composites. Polym Test 2022;110:107560.

[96] Vaidya UK, Samalot F, Pillay S, Janowski GM, Husman G, Gleich K. Design and manufacture of woven reinforced glass/polypropylene composites for mass transit floor structure. J Compos Mater, vol. 38, 2004.

[97] Zhu G, Sun G, Li G, Cheng A, Li Q. Modeling for CFRP structures subjected to quasi-static crushing. Compos Struct 2018;184.

[98] Joosten MW, Dutton S, Kelly D, Thomson R. Experimental and numerical investigation of the crushing response of an open section composite energy absorbing element. Compos Struct 2011;93.

[99] Bidadi J, Hampaiyan Miandowab H, Saeidi Googarchin H, Akhavan-Safar A, da Silva LFM. Experimental and numerical investigation on the crashworthiness performance of double hat-section Al-CFRP beam subjected to quasi-static bending test. Polym Compos 2024;45.

[100] Xiao Z, Mo F, Zeng D, Yang C. Experimental and numerical study of hat shaped CFRP structures under quasi-static axial crushing. Compos Struct 2020;249.

[101] Albayrak M. Experimental and numerical investigation of patch effect on the bending behavior for hat-shaped carbon fiber composite beams. Mater Test 2024;66.

[102] Abdulqadir SF, Tarlochan F. An experimental validation of numerical model for top-hat tubular structure subjected to axial crush. Appl Sci 2021;11.

[103] Chen D, Sun X, Xiao S, Yang G, Yang B, Zhu T, et al. On axial crushing behavior of double hat-shaped CFRP and GFRP structures. Compos Struct 2023;319.

[104] Rozylo P, Debski H. Effect of eccentric loading on the stability and load-carrying capacity of thin-walled composite profiles with top-hat section. Compos Struct 2020;245.

[105] Koricho EG, Belingardi G. An experimental and finite element study of the transverse bending behaviour of CFRP composite T-joints in vehicle structures. Compos Part B Eng

2015;79.

[106] Lombarkia R, Gakwaya A, Nandlall D, Dano ML, Lévesque J, Vachon-Joannette P. Experimental investigation and finite-element modeling of the crushing response of hat shape open section composite. Int J Crashworthiness 2022;27.

[107] Ranz D, Cuartero J, Castejon L, Miralbes R, Malon H. A cohesive zone model approach to interlaminar behaviour of carbon/epoxy laminated curved beams. Compos Struct 2020;238.

[108] Saghafi H, Ghaffarian SR, Salimi-Majd D, Saghafi HA. Investigation of interleaf sequence effects on impact delamination of nano-modified woven composite laminates using cohesive zone model. Compos Struct 2017;166.

[109] Kumar M, Kumar P, Bhadauria SS. Numerical simulation of delamination growth in fiber reinforced polymer laminates using cohesive zone modeling. Mech Adv Mater Struct 2022;29.

[110] Lu X, Ridha M, Chen BY, Tan VBC, Tay TE. On cohesive element parameters and delamination modelling. Eng Fract Mech 2019;206.

[111] Sun XC, Hallett SR. Failure mechanisms and damage evolution of laminated composites under compression after impact (CAI): Experimental and numerical study. Compos Part A Appl Sci Manuf 2018;104.

[112] Iarve E V., Hoos KH, Nikishkov Y, Makeev A. Discrete damage modeling of static bearing failure in laminated composites. Compos Part A Appl Sci Manuf 2018;108.

[113] Turon A, Dávila CG, Camanho PP, Costa J. An engineering solution for mesh size effects in the simulation of delamination using cohesive zone models. Eng Fract Mech 2007;74.

[114] Ullah H, Harland AR, Lucas T, Price D, Silberschmidt V V. Finite-element modelling of bending of CFRP laminates: Multiple delaminations. Comput Mater Sci, vol. 52, 2012.

[115] Xiang D, Chen C, Xie G, Gong Y, Ma J, Harkin-Jones E, et al. Mechanical property enhancement of basalt fiber-reinforced epoxy composites via construction of an organic/inorganic hybrid interface. Prog Nat Sci Mater Int 2025;35:359–67.

[116] Derakhshani K, Alimohammadi M, Eslami-Farsani R. The mechanical behavior of silane-modified nano–Al2O3/ basalt fiber/ polymer composite materials. J Mater Sci 2024;59:15270–82.

[117] Zhang Z, Sun W, Huang W, Zhu Y, Li J, Liang C, et al. Interfacial and mechanical properties of silane coupling agent interface-modified basalt fiber reinforced thermoplastic polypropylene resin composites. Polym Compos 2025;46:6582–93.

[118] R K, K.R P, Bheemappa S. Experimental investigations on the mechanical behavior of basalt fabric reinforced epoxy composites. J Polym Res 2025;32:1–20.

[119] Chirayil CJ, Mathew L, Hassan PA, Mozetic M, Thomas S. Rheological behaviour of nanocellulose reinforced unsaturated polyester nanocomposites. Int J Biol Macromol 2014;69.

[120] Cheon J, Kim M. Impact resistance and interlaminar shear strength enhancement of carbon fiber reinforced thermoplastic composites by introducing MWCNT-anchored carbon fiber. Compos Part B Eng 2021;217:108872.

[121] Al-Bahrani M, Cree A. A simple criterion to evaluate the degree of damage in composite materials after sudden impact loads by exploiting the MWCNTs piezoresistive property. Carbon N Y 2019;150:505–17.

[122] Sarath Kumar P, Jayanarayanan K, Balachandran M. Thermal and Mechanical Behavior of Functionalized MWCNT Reinforced Epoxy Carbon Fabric Composites. Mater Today Proc, vol. 24, 2020, p. 1157–66.

[123] Xiong S, Zhao Y, Wang Y, Song J, Zhao X, Li S. Enhanced interfacial properties of carbon fiber/epoxy composites by coating carbon nanotubes onto carbon fiber surface by one-step dipping method. Appl Surf Sci 2021;546:149135.

[124] Liu L, Yan F, Li M, Zhang M, Xiao L, Shang L, et al. Improving interfacial properties of hierarchical reinforcement carbon fibers modified by graphene oxide with different bonding types. Compos Part A Appl Sci Manuf 2018;107:616–25.

[125] Khanjanzadeh H, Behrooz R, Bahramifar N, Gindl-Altmutter W, Bacher M, Edler M, et al. Surface chemical functionalization of cellulose nanocrystals by 3-aminopropyltriethoxysilane. Int J Biol Macromol 2018;106:1288–96.

[126] Ng HM, Sin LT, Bee ST, Tee TT, Rahmat AR. Review of Nanocellulose Polymer Composite Characteristics and Challenges. Polym - Plast Technol Eng 2017;56.

[127] Liang D, Liu W, Zhong T, Liu H, Dhandapani R, Li H, et al. Nanocellulose reinforced lightweight composites produced from cotton waste via integrated nanofibrillation and compounding. Sci Rep 2023;13.

[128] https://store.astm.org/d5528-01r07e01.html?utm_source= 2010.

[129] https://store.astm.org/d7905_d7905m-14.html?utm_source= 2019.

[130] Park SJ, Meng LY. Surface treatment and sizing of carbon fibers. Springer Ser Mater Sci 2015;210.

[131] Jia H, Qiao Y, Zhang Y, Liu C, Jian X. Excellent and effective interfacial transition layer with an organic/inorganic hybrid carbon nanotube network structure for basalt fiber reinforced high-performance thermoplastic composites. Chem Eng J 2023;465.

[132] Yu S, Oh KH, Hwang JY, Hong SH. The effect of amino-silane coupling agents having different molecular structures on the mechanical properties of basalt fiber-reinforced polyamide 6,6 composites. Compos Part B Eng 2019;163.

[133] Wu Q, Deng H, Bai H, Ye Z, Chen X, Zhu J. Facile and eco-friendly functionalization of basalt fiber with polyelectrolyte complex toward excellent interfacial adhesion of epoxy composites. Compos Part A Appl Sci Manuf 2022;156.

[134] Jia H, Liu C, Zhang Y, Qiao Y, Zhao W, Chen X, et al. Electrophoretic deposition for the interfacial enhancement of BF/PPENK composite: GO vs. Ti3C2Tx MXene. Compos Part

A Appl Sci Manuf 2024;181.

[135] Wu Q, Zhao R, Zhu J, Wang F. Interfacial improvement of carbon fiber reinforced epoxy composites by tuning the content of curing agent in sizing agent. Appl Surf Sci 2020;504.

[136] Liu X, Li M, Feng P, Fan X, Yan Z, Jia H, et al. An anchor-inspired interface for improving interfacial properties of carbon fiber-reinforced high-performance thermoplastic composites. Compos Part B Eng 2024;283:111654.

[137] Liu N, Wang J, Yang J, Han G, Yan F. Effects of nano-sized and micro-sized carbon fibers on the interlaminar shear strength and tribological properties of high strength glass fabric/phenolic laminate in water environment. Compos Part B Eng 2015;68:92–9.

[138] Xiao C, Tan Y, Wang X, Gao L, Wang L, Qi Z. Study on interfacial and mechanical improvement of carbon fiber/epoxy composites by depositing multi-walled carbon nanotubes on fibers. Chem Phys Lett 2018;703:8–16.

[139] Rathore DK, Prusty RK, Kumar DS, Ray BC. Mechanical performance of CNT-filled glass fiber/epoxy composite in in-situ elevated temperature environments emphasizing the role of CNT content. Compos Part A Appl Sci Manuf 2016;84:364–76.

[140] Tian Y, Zhang H, Zhang Z. Influence of nanoparticles on the interfacial properties of fiber-reinforced-epoxy composites. Compos Part A Appl Sci Manuf 2017;98:1–8.

[141] Uribe BEB, Chiromito EMS, Carvalho AJF, Arenal R, Tarpani JR. TEMPO-oxidized cellulose nanofibers as interfacial strengthener in continuous-fiber reinforced polymer composites. Mater Des 2017;133:340–8.

[142] Xu X, Liu F, Jiang L, Zhu JY, Haagenson D, Wiesenborn DP. Cellulose nanocrystals vs. Cellulose nanofibrils: A comparative study on their microstructures and effects as polymer reinforcing agents. ACS Appl Mater Interfaces 2013;5:2999–3009.

[143] Kumar S, Graninger G, Hawkins SC, Falzon BG. A nanostructured cellulose-based interphase layer to enhance the mechanical performance of glass fibre-reinforced polymer composites. Compos Part A Appl Sci Manuf 2021;148:106475.

[144] Liu H, Sun Y, Yu Y, Zhang M, Li L, Ma L. Effect of Nano-SiO2 Modification on Mechanical and Insulation Properties of Basalt Fiber Reinforced Composites. Polymers (Basel) 2022;14:3353.

[145] Samarasekara AMPB, Kahavita KDHN, Amarasinghe DAS, Karunanayake L. Fabrication and characterization of nanofibrillated cellulose (NFC) reinforced polymer composite. MERCon 2018 - 4th Int Multidiscip Moratuwa Eng Res Conf, 2018, p. 449–54.

[146] Lamm ME, Li K, Qian J, Wang L, Lavoine N, Newman R, et al. Recent Advances in Functional Materials through Cellulose Nanofiber Templating. Adv Mater 2021;33:2005538.

[147] Wang X, Zhao X, Wu Z, Zhu Z, Wang Z. Interlaminar shear behavior of basalt FRP and hybrid FRP laminates. J Compos Mater 2016;50:1073–84.

[148] Pathak AK, Garg H, Singh M, Yokozeki T, Dhakate SR. Enhanced interfacial properties

of graphene oxide incorporated carbon fiber reinforced epoxy nanocomposite: a systematic thermal properties investigation. J Polym Res 2019;26.

[149] Nechyporchuk O, Håkansson KMO, Gowda.V K, Lundell F, Hagström B, Köhnke T. Continuous Assembly of Cellulose Nanofibrils and Nanocrystals into Strong Macrofibers through Microfluidic Spinning. Adv Mater Technol 2019;4:1800557.

[150] Pandian A, Vairavan M, Jebbas Thangaiah WJ, Uthayakumar M. Effect of Moisture Absorption Behavior on Mechanical Properties of Basalt Fibre Reinforced Polymer Matrix Composites. J Compos 2014;2014:1–8.

[151] Nayak RK, Mahato KK, Ray BC. Water absorption behavior, mechanical and thermal properties of nano TiO2 enhanced glass fiber reinforced polymer composites. Compos Part A Appl Sci Manuf 2016;90:736–47.

[152] Demircan G. Structural integrity of glass fiber reinforced nanocomposites under hydrothermal aging for offshore structure applications. Appl Ocean Res 2024;146:103959.

[153] Don DK, Reiner J, Jennings M, Subhani M. Basalt Fibre-Reinforced Polymer Laminates with Eco-Friendly Bio Resin: A Comparative Study of Mechanical and Fracture Properties. Polymers (Basel) 2024;16.

[154] Bashar MT, Sundararaj U, Mertiny P. Mode-I interlaminar fracture behaviour of nanoparticle modified epoxy/basalt fibre-reinforced laminates. Polym Test 2013;32.

[155] Scalici T, Pitarresi G, Badagliacco D, Fiore V, Valenza A. Mechanical properties of basalt fiber reinforced composites manufactured with different vacuum assisted impregnation techniques. Compos Part B Eng 2016;104.

[156] Zhou J, Zou M, Ng BF, Ou M. Emerging Sinusoidal Structures for Energy Absorption: Mechanisms, Optimizations and Applications. Compos Part B Eng 2025;306:112759.

[157] Reuter C, Tröster T. Crashworthiness and numerical simulation of hybrid aluminium-CFRP tubes under axial impact. Thin-Walled Struct 2017;117.

[158] Duan S, Mo F, Yang X, Tao Y, Wu D, Peng Y. Experimental and numerical investigations of strain rate effects on mechanical properties of LGFRP composite. Compos Part B Eng 2016;88.

[159] Oyiborhoro G, Anegbe B, Odiachi IJ, Atoe B, Ifijen IH. Environmental Impact of Multi-component Fiber-Reinforced Composites: Challenges and Green Solutions. Miner Met Mater Ser, 2024.

[160] Mo F, Zhang H, Yang X, Duan S, Xiao Z. Coupling investigation on tensile and acoustic absorption properties of lightweight porous LGF/PP composite. Polym Compos 2019;40.

[161] Zhang B, Yang J, Li Y, Zhang J, Niu S, Han Z, et al. Bioinspired basalt fiber composites with higher impact resistance through coupling sinusoidal and helical structures inspired by mantis shrimp. Int J Mech Sci 2023;244.

[162] Zhao Y, Zhang S, Xu Q, Wang K, Xu Z, Long T, et al. Synergistic enhancement of mechanical and thermal properties in basalt fiber reinforced composites through nanotube

and graphene bridging structure: A multi-scale simulation. Compos Part B Eng 2025;297:112289.

[163] Xu P, Xing J, Yao S, Yang C, Chen K, Li B. Energy distribution analysis and multi-objective optimization of a gradual energy-absorbing structure for subway vehicles. Thin-Walled Struct 2017;115.

[164] dua S, Khatri H, Naveen J, Jawaid M, Jayakrishna K, Norrrahim MNF, et al. Potential of natural fiber based polymeric composites for cleaner automotive component production -a comprehensive review. J Mater Res Technol 2023;25.

[165] Khan F, Hossain N, Mim JJ, Rahman SM, Iqbal MJ, Billah M, et al. Advances of composite materials in automobile applications – A review. J Eng Res 2024.

[166] Manikandan V, Winowlin Jappes JT, Suresh Kumar SM, Amuthakkannan P. Investigation of the effect of surface modifications on the mechanical properties of basalt fibre reinforced polymer composites. Compos Part B Eng 2012;43:812–8.

[167] Yu S, Oh KH, Hong SH. Effects of silanization and modification treatments on the stiffness and toughness of BF/SEBS/PA6,6 hybrid composites. Compos Part B Eng 2019;173.

[168] Nebe M, Schmack T, Schaefer T, Walther F. Experimental and numerical investigation on the impact response of CFRP under 3-point-bending. Compos Part C Open Access 2021;4.

[169] Liu Q, Ou Z, Mo Z, Li Q, Qu D. Experimental investigation into dynamic axial impact responses of double hat shaped CFRP tubes. Compos Part B Eng 2015;79.

[170] Zhou G, Tang H, Sun Q, Li D, Peng Y, Zeng D, et al. Analysis of the crushing behaviors of woven carbon fiber reinforced plastic hat section component under dynamic bending and axial crushing loading. Thin-Walled Struct 2021;161.

[171] Zhou Z, Sun W, Zheng N, Tang LC. Experimental and numerical investigation of the energy absorption characteristics of carbon-basalt hybrid fiber reinforced polymer composites under ballistic impact. Compos Struct 2024;335.

[172] Liu Q, Ma J, He Z, Hu Z, Hui D. Energy absorption of bio-inspired multi-cell CFRP and aluminum square tubes. Compos Part B Eng 2017;121.

[173] Isaac CW, Ezekwem C. A review of the crashworthiness performance of energy absorbing composite structure within the context of materials, manufacturing and maintenance for sustainability. Compos Struct 2021;257.